Nanoscale Horizons

REVIEW

View Article Online
View Journal | View Issue

Check for updates

Cite this: *Nanoscale Horiz.*, 2024, **9**, 900

Atomic-level imaging of beam-sensitive COFs and MOFs by low-dose electron microscopy

Zhen Zhan,[a] Yuxin Liu,[a] Weizhen Wang,[a] Guangyu Du,[a] Songhua Cai *[a] and Peng Wang *[b]

Received 7th November 2023,
Accepted 1st March 2024

DOI: 10.1039/d3nh00494e

rsc.li/nanoscale-horizons

Electron microscopy, an important technique that allows for the precise determination of structural information with high spatiotemporal resolution, has become indispensable in unravelling the complex relationships between material structure and properties ranging from mesoscale morphology to atomic arrangement. However, beam-sensitive materials, particularly those comprising organic components such as metal–organic frameworks (MOFs) and covalent organic frameworks (COFs), would suffer catastrophic damage from the high energy electrons, hindering the determination of atomic structures. A low-dose approach has arisen as a possible solution to this problem based on the integration of advancements in several aspects: electron optical system, detector, image processing, and specimen preservation. This article summarizes the transmission electron microscopy characterization of MOFs and COFs, including local structures, host–guest interactions, and interfaces at the atomic level. Revolutions in advanced direct electron detectors, algorithms in image acquisition and processing, and emerging methodology for high quality low-dose imaging are also reviewed. Finally, perspectives on the future development of electron microscopy methodology with the support of computer science are presented.

Open Access Article. Published on 21 March 2024. Downloaded on 1/15/2026 6:48:41 PM.
This article is licensed under a Creative Commons Attribution-NonCommercial 3.0 Unported Licence.

1. Introduction

Chemistry and materials science have long been focused on understanding molecular and atomic structure/orientation to design novel materials with desired physicochemical properties. Crystalline molecules with a regular arrangement and long-range order serve as an ideal target for elucidating the relationships between inherent structures and properties, thus providing a controllable and quantifiable array. Inorganic crystals have been the primary focus of crystal research for several decades, owing to their exceptional physicochemical stability and processability.[1,2] However, this stability can limit structural design flexibility due to relatively fixed-mode binding. In contrast, organic building blocks exhibit greater designability and diversity, endowing organic-containing composites with exceptional structural flexibility.[3] However, similar to the conflicts between diversity and stability, the controllability of precise multilevel structure from the molecular junctions to the condensed-matter structure may be exponential-growth as the active site increases, leading to the sluggish development of crystalline organic materials (COMs). The construction of primary and high-order alignment through the retention of inorganic building elements (metal ions or clusters) and their connection with organic linkages has been proposed. Originally referred to as coordination polymers, these structures are now commonly known as metal–organic frameworks (MOFs).[4] The discovery of the crystallization of MOFs has prompted researchers to explore methods for synthesizing crystalline structures from solely organic building blocks through covalent bonds, instead of coordination interactions. Then, the pioneering covalent organic frameworks (COFs), which combine covalent and noncovalent interactions, were first reported by Yaghi and colleagues[5] in 2005, with their development occurring over the past decade. The extraordinary expansion of MOFs and COFs can be attributed to the versatile organic linkers. As shown in Fig. 1, over the past decade, more than 100 000 articles about MOFs have been reported, and COFs, despite their later inception, have also experienced exponential growth. In addition to their diverse construction units, MOFs and COFs exhibit several intriguing characteristics, such as exceptional chemical stability, intrinsic porosity, and the potential for post-modification or hybridization. These attractive features have numerous applications in fields such as gas adsorption and separation,[6,7] heterogeneous catalysis,[8,9] and energy storage and conversion.[10,11]

The topology diagram of MOFs and COFs is guided by the judicious selection of organic building blocks, resulting in a

[a] *Department of Applied Physics, The Hong Kong Polytechnic University, Kowloon 999077, Hong Kong SAR, China. E-mail: songhua.cai@polyu.edu.hk*
[b] *Department of Physics, University of Warwick, CV4 7AL, Coventry, UK. E-mail: peng.wang.3@warwick.ac.uk*

This journal is © The Royal Society of Chemistry 2024

Open Access Article. Published on 21 March 2024. Downloaded on 1/15/2026 6:48:41 PM.
This article is licensed under a Creative Commons Attribution-NonCommercial 3.0 Unported Licence.

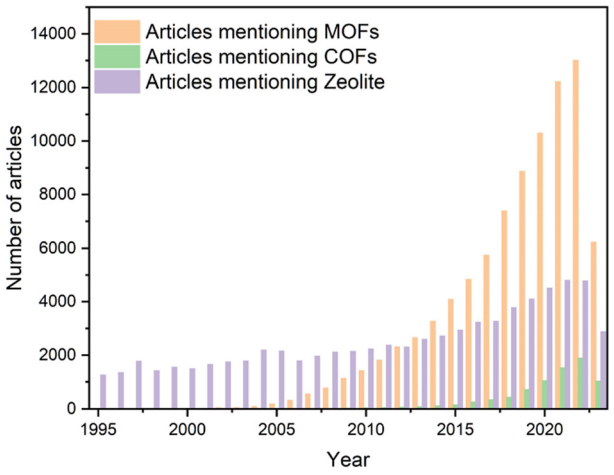

Fig. 1 Papers mentioning "metal organic framework", "covalent organic framework" and "zeolite" in the title, the abstract or the keyword, as searched in Web of Science in Aug 2023.

predesignable skeleton.[12,13] Such a well-defined alignment facilitates the determination of the structure–property relationship, thereby enabling the design of specific functionalized materials. To gain a comprehensive understanding of their structure, numerous state-of-the-art techniques have been applied, ranging from the holistic to the localized and atomic level. Single crystal X-ray diffraction (SXRD) is a potent technique for revealing the component, structure, and three-dimensional stereo-structural information. However, the production of large COM single crystals remains challenging.[14] Researchers commonly utilize powder X-ray diffraction (PXRD) to analyse the crystal structure; yet the local structure remains an enigma. Consequently, atomic-level characterization is indispensable for deciphering the structural details from a microscopic perspective, especially for the localized defects and interfaces.

Transmission electron microscopy (TEM)[15] and scanning transmission electron microscopy (STEM)[16] are among the most promising techniques for revealing long-range ordered alignment at the atomic level especially for intragrain structures, while scanning tunnelling microscopy (STM),[17] atomic force microscopy (AFM),[18] and scanning electron microscopy (SEM)[19] can only obtain the surface structure information. In the structural analysis of MOFs and COFs, TEM techniques such as electron diffraction and imaging are utilized. By capturing multiple diffraction patterns from a single crystal, electron diffraction, and more specifically the three-dimensional electron diffraction, is a highly effective method for depicting the structure with high precision.[20–23] However, it remains incapable of revealing local structural information, such as interfaces and defect distribution. Consequently, imaging with atomic-level spatial resolution is essential for investigating the tendency for variation between structure and performance.

Imaging MOFs and COFs with distinct atomic distribution is challenging due to the susceptibility of the light elements in the organic portion to high-energy electrons. Cryogenic electron microscopy (cryo-EM) can mitigate electron beam damage and enable the determination of the intrinsic structure of beam-sensitive materials including organic components.[24] However, despite some successful reports of cryo-EM in COFs, it is difficult to effectively protect the sample only by low temperature. This is due to the primary damage in COMs being radiolysis, which is dominated by the electron dose.[25,26] Therefore, a low electron-dose approach is considered as the fundamental solution for atomic-scale imaging of MOFs and COFs.[25,27]

The advancement of low-dose technology in TEM hinges on a series of technological innovations, including the electron optical system, detector, image processing, and specimen protection. A breakthrough in low-dose technology was achieved with the introduction of direct electron detectors (DEDs).[28] These DEDs exhibit an order-of-magnitude enhancement in detection quantum efficiency, leading to an unprecedented increase in the signal-to-noise ratio (SNR) with much higher acquisition speed compared to conventional charge-coupled device (CCD) cameras.[29] Additionally, the development of the integrated differential phase contrast (iDPC) approach based on the segmented STEM detectors represents a significant advancement in low-dose STEM imaging.[30] iDPC-STEM enables the acquisition of directly interpretable images from the averaged electronic potential in relation to atomic number Z, allowing elements with large Z differences to be imaged simultaneously. The recent progress of the four-dimensional STEM (4D-STEM) technique has opened an intriguing research methodology in the field of TEM.[31] This technique relies on the advanced high-speed pixel array detector to record a 4D dataset comprising 2D diffraction patterns at each scanning pixel. These datasets can be utilized to reconstruct the electrostatic potential of the specimen and extract the phase information. The development of low-dose technology in TEM was sparked by the invention of detectors, which were subsequently supported by advancements in computer technology. For example, the alignment of the crystal zone axis, a time-consuming procedure that accumulates electron dose and causes more damage to beam-sensitive materials, can now be automated to reduce the incident dosage. In data analysis, computer technology also plays a crucial role. Recent advances in electron ptychography have enabled the spatial resolution of TEM characterization to reach 23 picometers, allowing for precise measurements of structural details up to the sub-atomic level.[32]

Despite significant achievements in TEM data acquisition and post-processing, advancements in specimen protection techniques are essential for reducing beam damage and cannot be neglected. This article focuses on the electron beam damage mechanism in COFs and MOFs and explores technological innovations that can address this issue. We review both the most widely used techniques for TEM characterization of COFs and MOFs, and some more esoteric methods. The potential combination with other technologies, such as *in situ* TEM, is also discussed.

2. Electron beam damage in COMs

2.1 Electron beam damage mechanisms

The development of high-voltage field emission guns has significantly improved the resolution limits of electron

Open Access Article. Published on 21 March 2024. Downloaded on 1/15/2026 6:48:41 PM.
This article is licensed under a Creative Commons Attribution-NonCommercial 3.0 Unported Licence.

microscopes. However, the electron beam accelerated by such a high voltage can cause irreversible structural damage, particularly in beam-sensitive materials, impeding the determination of their pristine structure. Electron beam damage can manifest in various forms, including heating, knock-on damage or sputtering, and radiolysis.[15,33] Heating refers to the phonon vibration that can raise the temperature of the sample, particularly in materials with poor electrical or thermal conductivity. This can be alleviated by reducing the inelastic scattering cross-section through voltage increments. Knock-on damage or sputtering arises when the direct electron–nucleus contact results in atomic displacements or removal. This damage can be mitigated by employing incident electrons with energies less than the threshold for specific atomic displacement. Radiolysis, which entails the disintegration of chemical bonds due to electron–electron interaction, is accompanied by ionization and recombination of a different nature than that at the origin. Radiolysis can be mitigated by increasing the acceleration voltage. In organic specimens such as COMs, both knock-on damage and radiolysis contribute to the overall damage induced by electron beam irradiation. The selection of an appropriate operating voltage is crucial, considering the dominant damage mechanism. Operating at an accelerating voltage below a specific threshold value can potentially reduce knock-on damage and minimize the total damage to some extent. However, it should be noted that radiolysis is recognized as the primary damage mechanism in organic specimens and similar porous crystal zeolites due to their higher cross sections and relative damage susceptibility.[33] As a result, higher voltages are commonly employed, while low voltages are also applied in some cases.

2.2 The main damage mechanism in COMs

Maintaining a long-term ordered structure in COFs and MOFs poses a formidable challenge due to their unparalleled designability. Moreover, the inherent porosity of these materials exacerbates the issue by inducing substantial structural deformations arising from bond breakage and atomic displacement caused by beam damage.[26] Consequently, these factors contribute to an accelerated loss of crystallinity over time. Nevertheless, research is ongoing to identify the primary mechanism responsible for electron beam damage in these materials.

In 2012, Hmadeh and colleagues[34] observed a crystalline MOF material, Ni-CAT-1, for the first time using an aberration-corrected STEM at 60 kV. The images revealed the honeycomb structure of Ni-CAT-1, but the framework destructively collapsed after the entire scan process. As shown in Fig. 2a–c, similar strategies were employed to investigate the structure of MOF-5 under liquid nitrogen temperature and at a low acceleration voltage of 80 kV.[35] These conditions guaranteed the reduction of electron beam-induced damage in sensitive samples, thereby avoiding the collapse during the acquisition time. However, diffraction reflections dissipate after only a few seconds, particularly when dealing with information from individual particles.

Cryo-EM has recently emerged as a powerful technique for determining the nanostructure of proteins and energy materials, such as lithium batteries and perovskites.[36,37] These examples suggest that a cryogenic environment may prevent structural devastation from beam damage. Li *et al.*[38] developed a novel cryo-EM procedure for disclosing atomic host–guest structures within MOFs and demonstrated that these entities can be preserved at low temperatures for high-resolution imaging (Fig. 2e). The sample ZIF-8 underwent only partial amorphization when exposed to an accumulated electron dose of 90 e Å^{-2} at cryogenic temperature, whereas its crystallinity was completely destroyed when exposed to a dose of 50 e Å^{-2} at room temperature (Fig. 2f–h). Ogata *et al.*[39] analysed the nucleation and growth of protein-MOFs using cryo-EM and disclosed the crucial stage of amorphous particle aggregation in triggering the dissolution–recrystallization process. Tong *et al.*[40] attempted to ascertain the atomic-level structure of biomacromolecule-MOFs and the intrinsic relationship between their structure and activity. Notably, the cumulative dose of 30 e Å^{-2} for the optimal images is comparable to that used for MOFs and COFs at room temperature, indicating that although cryogenic temperatures can increase stability by several factors, it may not be a universal solution for extremely sensitive materials.

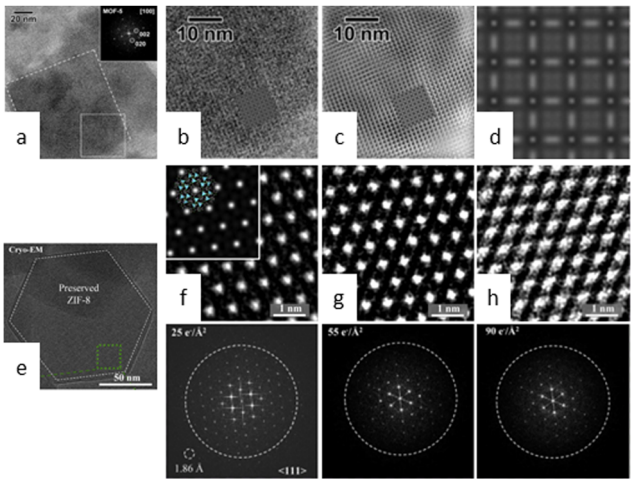

Fig. 2 Cryo-EM images of MOFs. (a) HRTEM images of MOF-5. (b) Experimental image along the [100] direction. (c) Filtered image. (d) Simulated image. Reproduced with permission.[35] Copyright 2012, Elsevier. (e) Cryo-EM image of ZIF-8 along the ⟨111⟩ direction. Electron doses of 25 e Å^{-2} (f), 50 e Å^{-2} (g), and 90 e Å^{-2} (h) with the corresponding FFT pattern. Reproduced with permission.[38] Copyright 2019, Elsevier.

In this context, radiolysis has been identified as the primary mechanism responsible for the damage. Ghosh *et al.*[26] used ZIF-8 to investigate the dominant damage mechanism by varying the incident electron dose rate from 2.91 to 0.34 e Å^{-2} s^{-1} (Fig. 3). Their findings indicated that, compared with inevitable knock-on damage, radiolysis is the leading cause of MOF destruction. Zhu *et al.*[25] revealed that ZIF-8 crystals were obliterated by a cumulative dose of 25 e Å^{-2} and exhibited rapid crystallinity loss even at 1 e Å^{-2} s^{-1}. They captured the motion-corrected images with a total dose of 4.1 e Å^{-2}. Based on the strategy of combining multiple short-exposed images into one, they achieved an effective acquisition at a total dose of 10 e Å^{-2}.[41] This approach can distinguish certain metal atomic columns, distinct surface terminations, and benzene rings in organic linkers. It can be applied to a variety of other electron

 This journal is © The Royal Society of Chemistry 2024

Open Access Article. Published on 21 March 2024. Downloaded on 1/15/2026 6:48:41 PM.
This article is licensed under a Creative Commons Attribution-NonCommercial 3.0 Unported Licence.

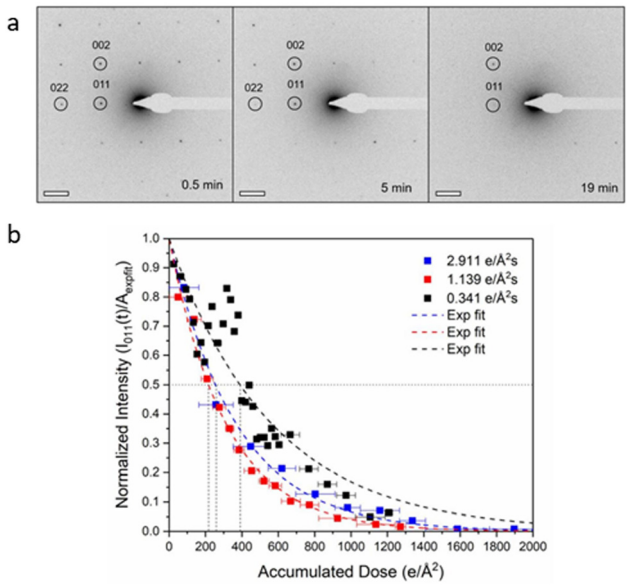

Fig. 3 The effect of total dose on the crystallinity of MOFs. (a) Electron diffraction pattern of ZIF-8 at a dose rate of 0.34 e Å^{-2} s^{-1}. (b) The intensities decrease at three different dose rates. Reproduced with permission.[26] Copyright 2019, Oxford University Press.

beam-sensitive materials, such as the organic–inorganic hybrid perovskite $CH_3NH_3PbBr_3$. The study of ZIF-L revealed that at a dose of 25 e Å^{-2}, the crystallinity suffered a noticeable loss, and completely collapsed at a dose of 100 e Å^{-2}.[42] At a cumulative dose of 50 e Å^{-2}, the visible bend contours in individual ZIF-L particles diminish and eventually disappear. Peng and colleagues[43] set the electron dose at 20 e Å^{-2}, at which the honeycomb-like structure with individual construction blocks in the as-prepared ultrathin COF nanosheets can be plainly visualized. This is the first report on the atomic structure of COFs by high-resolution TEM (HRTEM) imaging.

Besides the total dose, the dose rate also affects the damage and the corresponding deformation behavior. Zhou *et al.*[27] used iDPC-STEM with a progressively increased beam current from 2 to 8 pA to ascertain the evolution process of MIL-101 crystals. The crystals exhibited bend behavior related to the specific facet and position to form distinct domains, as opposed to overall structure change with broken crystals. The *d* spacing shrank in all directions at almost the same rate as the accumulated dose increased from 28 to 46 e Å^{-2}. When the beam current reached 8 pA, it was discovered that the (111) lattice plane contracted much more rapidly than the other directions. Similar electron irradiation was conducted on UiO-66 at a dose rate of 2.17 e Å^{-2} μs^{-1}, and the acquired images demonstrated an increase in the contrast between the metal node and organic linkers with the increase in the total dose, corresponding to the release of organic linkers from the skeleton.[44] In general, the rate of damage follows first-order decay kinetics stated as $I/I_0 = \hat{e}(-D/D_c)$, where D_c is the critical dose, which was determined as 256.41 e Å^{-2} in this case. Significantly, unlike uniform defects caused by ultra-low dose rate (4.38 e Å^{-2} μs^{-1}), larger area nonuniform defects formed with the same accumulated dose but a high rate of 7.84 e Å^{-2} μs^{-1}, indicating the influence of local charging and heating dominated by dose rate. Hence, minimizing the electron dose prior to their degradation is the most effective solution for precise atomic resolution images of beam-sensitive materials.

3. Technological innovations for low dose imaging

To prevent the collapse of multilevel ordered structures, low dose imaging has been identified as the primary solution. Nevertheless, ultralow doses can adversely affect image resolution, resulting in low SNR that can impede the atomic-level characterization. To achieve high-quality imaging under minimal doses, the first obstacle is the detector technology, which requires improving the detection efficiency of conventional CCD cameras. Innovative detectors, such as DEDs, have significantly increased detection efficiency, enabling the emergent application of low-dose imaging.[28] The second factor that makes low-dose imaging more practical is the computer-assisted acquisition and interpretation of images under limited doses. Although zone-axis alignment and information rescanning can be time-consuming, recent advancements in computer technologies have significantly accelerated these processes. These advancements enable the analysis of complex information contained in images, including those that may be concealed behind a deceptive representation. In addition to image acquisition and analysis under low-dose conditions, sample processing to mitigate radiolysis damage is also a crucial factor.

3.1 Innovations in detectors

CCD cameras have been a standard component in electron microscopes since the 1980s, providing real-time reading as an alternative to photographic films.[29,45] These cameras typically consist of a scintillator that converts electrons to photons, which are then conveyed *via* fiber optics or lens coupling to generate electrical signals for readout (Fig. 4a). However, the SNR of CCD images is insufficient for the point-spread function, limiting their practicality. Moreover, the charges in CCD cameras must be read out pixel by pixel, after being transmitted row by row into a serial register (Fig. 4c). This readout process significantly limits their read rates and precludes their use for accurate specimen motion correction.

The direct conversion of electrons into an electronic signal can significantly increase the SNR and acquisition speed. The development of DEDs, such as the monolithic active pixel sensors (MAPs), has made this vision a reality that marked a turning point in TEM technology.[28] By eliminating noise and signal distortions during electron–photon conversion and transfer (Fig. 4b), DEDs can provide a significantly higher quantum efficiency and SNR, resulting in the improvement of image qualities at a given dose. MAPs, with a narrow sensitive layer less than 30 μm, can receive a portion of the incident electron's energy and deposit it within a pixel, allowing for an enormous number of pixels more than 4000 × 4000 without

Open Access Article. Published on 21 March 2024. Downloaded on 1/15/2026 6:48:41 PM.
This article is licensed under a Creative Commons Attribution-NonCommercial 3.0 Unported Licence.

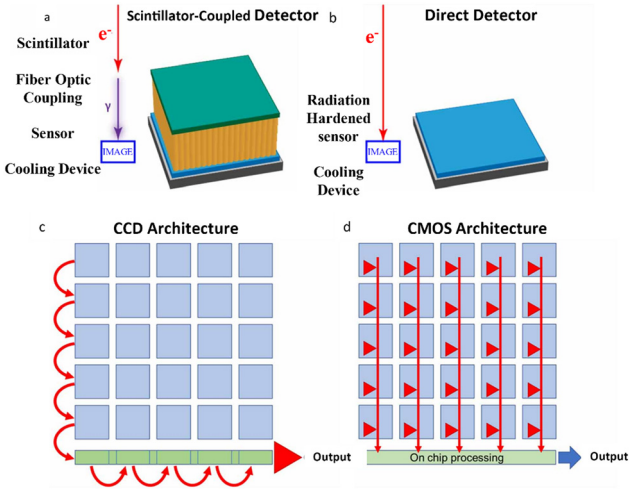

Fig. 4 The difference between conventional CCDs and DEDs. (a) The electron–photon-sensor process in CCDs. (b) The electron-sensor process in DDEC. (c) The row-by-row readout architecture in CCDs. (d) The simultaneous readout architecture in every pixel in DEDs. Reproduced with permission.[28] Copyright 2020, American Chemical Society.

back-scattering interference. Based on the high sensitivity of DEDs, which can convey signals even from a single electron, high spatial resolution imaging with rapid input and output speeds is achievable (Fig. 4d). Milazzo *et al.*[46] reported that the enhanced capability of DEDs could be utilized in high quality 3D structure maps of biological samples under low dose with image drift correction, demonstrating the great potential of DEDs. Specifically, DEDs can increase the visibility of holographic fringes and decrease the statistical inaccuracy of the phase of the reconstructed electron wave function. They can also withstand higher dose rates, allowing dose rate optimization to achieve the highest phase resolution under a variety of experimental conditions. Therefore, the counting mode may be able to use a significantly lower dose while still achieving a phase resolution comparable to that of the linear method. During the detection of the oxygen K edge signal in a biological protein, the SNR in electron energy loss spectroscopy (EELS) is reported to be 10 times higher than that of traditional CCDs.[47]

In contrast to the parallel beam used in TEM, STEM generates images by traversing a focused electron beam over the specimen, with signals including transmitted electrons and dispersed electrons detected by a bright field (BF) detector and annular detector, respectively. High angle annular dark field (HAADF) imaging is the most common modality for acquiring images with a high contrast proportional to $Z^{1.5-2.0}$. However, it remains challenging to image heavy and light atoms simultaneously in HAADF-STEM. Furthermore, the limited utilization of incident electrons due to sparse scattering necessitates higher electron doses for acquiring high SNR images. Shibata *et al.*[48] developed a new segment detector to thoroughly record the dispersed electrons and obtained 16 images simultaneously at the atomic level for post-processing. By calculating the difference between the signals taken by the opposing detector segments, the magnitude and direction of the electron beam's deflection can be measured quantitatively at each sample raster during beam scanning. The ability to record the localized and total electric and magnetic field of light and heavy element columns through the deflection is superior for constructing the exhaustive maps of the atoms' distribution, as opposed to the ambiguous "ghost" of the light atom in traditional methods.[49,50] Lazić *et al.*[30] proposed a continuously developed technology, iDPC-STEM, that demonstrates the approximately linear relationship between the diffraction disk's center of mass and its phase. iDPC-STEM can use almost all of the transmitted electrons to reduce the total electron dose for imaging (Fig. 5a and b).[51] Their work on $SrTiO_3$ demonstrated that even O atoms were clearly visible from iDPC-STEM images, while the corresponding information was absent in HADDF-STEM images (Fig. 5c).[52] The integration procedure automatically applies physical regularization, suppressing the non-conservative portions of the noise field. iDPC-STEM has rapidly become one of the most prevalent low-dose imaging methods. Recent studies demonstrate the direct observation of molecules adsorbed in delicate porous zeolites at the atomic level, revealing different orientations caused by host–guest interaction in individual channels, elucidating atomic-level adsorption-catalysis processes.[53,54]

Besides the segment detector, hybrid pixel array detectors (HPADs), a subtype of DEDs, were developed to determine the

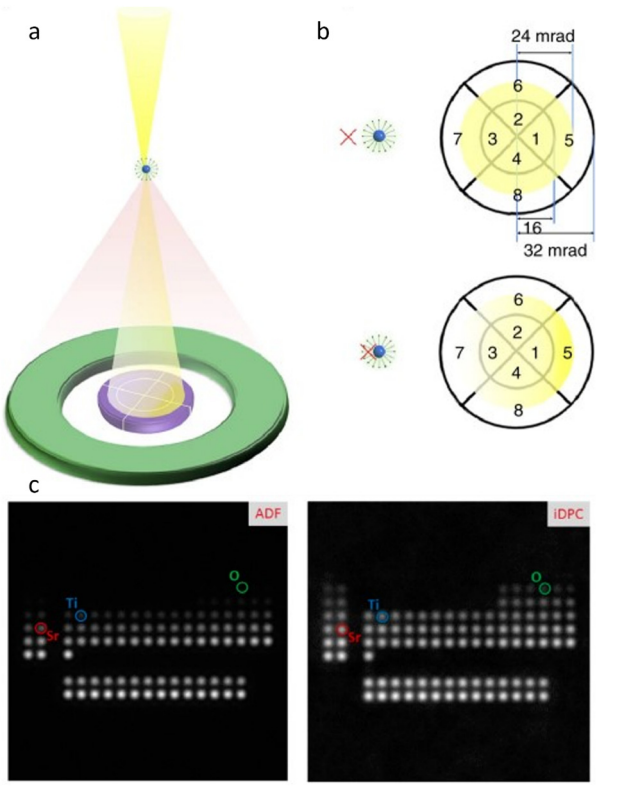

Fig. 5 The schematic illustration and imaging of the segment detector. (a) Segment detector inserted in the bright-field region and (b) intensity distribution for distinct probe position. Reproduced with permission.[51] Copyright 2017, Springer Nature. (c) Simulated ADF-STEM and iDPC-STEM images of the periodic table of elements. Reproduced with permission.[52] Copyright 2016, Oxford University Press.

 This journal is © The Royal Society of Chemistry 2024

Open Access Article. Published on 21 March 2024. Downloaded on 1/15/2026 6:48:41 PM.
This article is licensed under a Creative Commons Attribution-NonCommercial 3.0 Unported Licence.

phase of a specimen based on its atomic electrostatic potential.[55] The thick sensor chips in HPADs, such as the electron microscope pixel array detector (EMPAD)[56] in Fig. 6a and b, can capture all incident electrons to reconstruct the phase information, making them suitable for 4D-STEM acquisition. The detector records the 2D convergent beam electron diffraction (CBED) pattern for every dwell position in the 2D STEM raster over the specimen, enabling a 4D dataset to collect nearly all information about the specimen, including electric/magnetic field and strain. The synchronous readout of all pixels in HPADs can increase the recording speed with each pixel's real space and reciprocal space information to be read out.

Early 16 × 16 HPADs with a frame rate of 1.1 kHz had sufficient pixel density to distinguish distinct diffraction peaks, although slower than conventional STEM scan rates.[55] The EMPAD significantly improved the SNR to 140 with a readout time of 0.86 milliseconds per frame and a high dynamic range of 10^6 for incident electrons.[57,58] This remarkable dynamic range can help comprehensively map the specimen's physical information by describing features of interest with a wide variation in intensity. The second-generation EMPAD is capable of continuous imaging at a frame rate of 10 kHz, with a low-noise dynamic range extending from a single electron to 1.3×10^7 electrons.[59,60] The simultaneous high-precision measurements of all electrons suggest the possibility of extracting lattice information and strain maps from the complex datasets. Besides, a pixelated detector with 576 × 576 pixels was created with a frame rate up to 87 kHz, ensuring a data rate of 480 Gbit s^{-1} to record the data in minutes using fundamental edge computing algorithms.[61]

The information recorded in 4D-STEM can be used to construct virtual images like conventional STEM imaging such as HAADF and also can be applied to retrieve phase information by ptychography. Ptychography is based on the predictability of interference patterns during scanning and has been widely utilized in X-ray and optical microscopy. The technique is particularly attractive in electron microscopy due to the possibility of surpassing the information limit caused by the diffraction principle.

The challenges such as insufficient recording, inadequate dynamic range, and sluggish readout rates in ptychography can be resolved by utilizing HPADs, which offer a high dynamic range and synchronous readout of all pixels (Fig. 6d).[62–64] Jiang *et al.*[58] reported full-field ptychography using an EMPAD to decode phase information encoded in the diffraction pattern. The reconstructed image achieved a spatial diffraction-limited resolution of 0.39 Å, which is superior to the 0.98 Å resolution achieved by the conventional method under the same conditions. The atomic-resolution limits could be further improved to less than 20 pm by ptychography, corresponding to the thermal vibration of atoms (Fig. 6c and e).[32] The future introduction of rapid hollow detectors, designed to work seamlessly with EELS spectrometers, facilitates concurrent correlative analysis incorporating *Z*-contrast, phase imaging (ptychography and DPC), and chemical mapping (EELS, EDS and secondary electrons) (Fig. 6d).[62] Such multimodal STEM configuration offers multiple information channels about the specimen, ensuring efficient utilization of the electron dose.

3.2 Innovations in imaging procedures and acquisition

Modern detectors are indispensable for decoding the atomic structure of specimens. However, they alone are insufficient for implementing a practicable low dose strategy. The essential

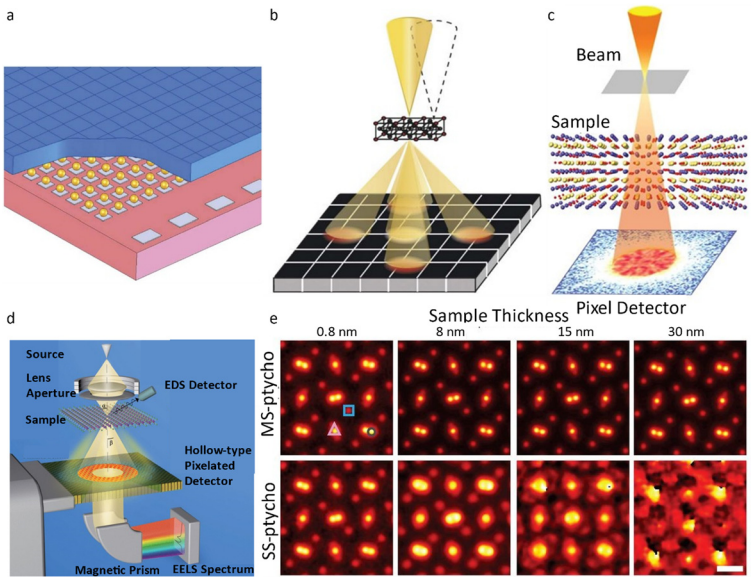

Fig. 6 The pixel detector and schematic illustration for ptychography. (a) The illustration of the structure of the EMPAD. (b) The schematic illustration of 4D-STEM imaging by the EMPAD. Reproduced with permission.[56] Copyright 2016, Oxford University Press. (c) Experimental setup for ptychography. Reproduced with permission.[32] Copyright 2021, The American Association for the Advancement of Science. (d) Configuration for ptychography dataset acquisition. Reproduced with permission.[62] Copyright 2018, American Physical Society. (e) The reconstructed images of $PrScO_3$ with distinct thickness by multislice and single-slice ptychography. Reproduced with permission.[32] Copyright 2021, The American Association for the Advancement of Science.

Open Access Article. Published on 21 March 2024. Downloaded on 1/15/2026 6:48:41 PM.
This article is licensed under a Creative Commons Attribution-NonCommercial 3.0 Unported Licence.

processes involve time-consuming image acquisition procedures, such as specimen searching, zone axis alignment, investigation of optimal imaging conditions, and image acquisition, resulting in excessive dosage waste.[41] Even for seasoned researchers, evaluating the images and adjusting the corresponding parameters is a laborious process. Consequently, automated image acquisition and correction by computer technology can effectively reduce unnecessary time and minimize the overall accumulated dose. Unlike subsequent steps that require precise regulation, specimen searching does not rely on automatic operation and can be performed at extremely low dose rates of 10^{-3} e Å^{-2} s^{-1}. While some automated systems have been developed to achieve effective detection without operator intervention, this is not a requirement for specimen searching.[65]

Accurately aligning the zone axis is a primary challenge in controlling cumulative dose in TEM. Traditionally, the zone axis is progressively aligned by repeatedly toggling between imaging and diffraction patterns. This crucial stage enables the final visualization of the atomic distribution in the structure but comes at the expense of high dose consumption. Jansen *et al.*[66] proposed an approach that combined the multislice method with a least-squares algorithm to rectify lattice misalignment with respect to the Laue circle, which performed well when the misorientation was small. Hayashida and collaborators[67] presented a coarse-alignment based on a cross-correlation technique that presumes the tilt angle could range from $\alpha = -90^\circ$ to 90°. This method worked well as an automatic pre-alignment prior to a precise zone axis alignment. Jansen *et al.*[68] further improved the alignment procedure to achieve a high degree of precision up to 0.05–0.02° by recording a series of diffraction patterns. The dedicated open-source software ALPHABETA offers a simple user interface that allows users to calibrate the orientation of the specimen and then compute the tilt angles.[69] This tool considerably reduces tilting work time by allowing for considerable tilts possible in image mode with approachable zones pre-indicated in the program. Zhang *et al.*[41] designed a program to automatically calculate the deviated angle between the incident beam and the zone axis and conduct alignment accordingly. As shown in Fig. 7a–f, similar to the traditional method, the electron diffraction pattern is acquired to identify the orientation of the sample. The computer initially calculates the Laue circle by fitting the reflection positions to confirm the variation angle. The angle is then disassembled into α and β directions according to the TEM double tilt stage, and the following alignment based on the decomposed angle is implemented automatically. After the alignment, another diffraction pattern is collected to confirm the final orientation of the specimen. The same process is repeated until the alignment is nearly perfect. The number of measurements could be as low as two (several for perfect alignment), and the dose rate for diffraction can be decreased to 0.03 e Å^{-2} s^{-1}. Then, the total dose for the whole zone axis alignment process can be far less than 1 e Å^{-2}, significantly reducing the dose consumption before the final imaging. To realize a universal reorientation under a wide range of the misalignment angle, a program was developed to automatically index the diffraction patterns and tilt from a specific position (Fig. 7g).[70] Under essentially the same procedure, an additional parameter about the crystal structure is necessary for a comprehensive evaluation about the orientation. As a result, the program can achieve a fast and precise alignment, and move the axis from one to another without manual operation under a deviation less than 0.6°.

However, the optimal imaging conditions in HRTEM are typically judged by researchers instead of being tuned by computer. This is because the image contrast is affected by the defocus value, with the lowest contrast being observed when the specimen is in focus. The optimal defocus value, Scherzer defocus, is dependent on the spherical variance coefficient and electron wavelength of the objective. The phase contrast transfer function (CTF) obtains the defocus of the widest spatial frequency passband, enabling researchers to determine the in-focus position and thoroughly consider imaging under different defocus values. Koster *et al.*[71] proposed an

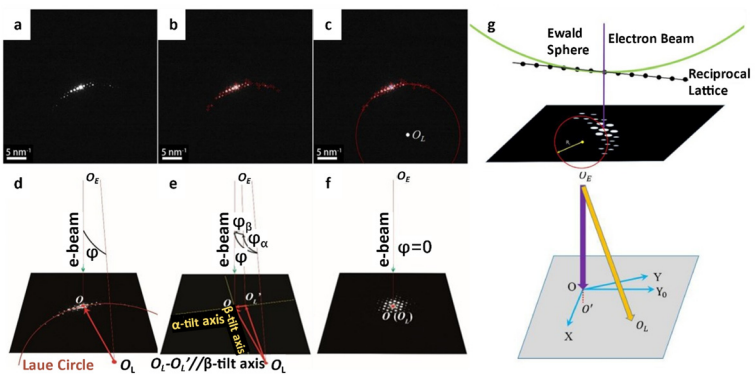

Fig. 7 The automatic alignment of the zone axis. (a) The initial diffraction pattern acquisition. (b) Identification of reflection peaks. (c) Automatic fitting of the Laue circle and determination of the center O_L. (d) Calculation of the angle between the zone axis and the incident direction. (e) The decomposition of the angle to α- and β-tilt axes. (f) The realization of the on-axis condition. Reproduced with permission.[41] Copyright 2018, The American Association for the Advancement of Science. (g) The condition for a Laue ring and corresponding tilting to the Laue circle. Reproduced with permission.[70] Copyright 2020, Elsevier.

 This journal is © The Royal Society of Chemistry 2024

Open Access Article. Published on 21 March 2024. Downloaded on 1/15/2026 6:48:41 PM.
This article is licensed under a Creative Commons Attribution-NonCommercial 3.0 Unported Licence.

autofocus method by adjusting the beam's tilt and measuring the image displacement, followed by correction of the defocus based on the well-established association between the defocus and the displacement. While this method achieved a precision of 5 nm, it is not satisfactory for modern TEM imaging. To improve the accuracy and reliability of autofocus, further advancements have been made by operating under low-dose conditions and stretching the image before cross-correlation.[72]

Image acquisition is a critical process in low dose technology, but it remains challenging to achieve significant progress using conventional methods. To minimize the accrued electron dose in STEM, two conventional methods have been employed: decreasing the scanning dwell time on each pixel and reducing the number of incident electrons.[73] However, these methods suffer from limitations such as the loss of stability of the scanning coil and potential misalignment due to the varied beam crossover. Recently, computer technology has provided an alternative method for low dose image acquisition using compressed sensing (CS).[74] In conventional sampling methods, the signal taken from the full sampling model can be used to reconstruct the image perfectly. However, under-sampled measurements, which compress the signal, can be reconstructed using a mathematical algorithm that considers *a priori* knowledge of the signals. Thus, perfect reconstruction from under-sampling can replace the fully sampled method, thus reducing the sampling rate and exposure time for low dose imaging. CS was first applied in electron tomography, a technology used to reconstruct the 3D morphology of specimens, to recover images from incomplete signals.[75] Saghi *et al.*[76] analysed the 3D structure of iron oxide nanoparticles with improved reconstruction quality including fewer missing wedges, providing reliable quantitative analysis without tedious projections. To achieve dynamic and real-time imaging, a dynamic CS framework was developed.[77] After the initial projection is acquired, the reconstruction process begins instantly and dynamically modifies the 3D structure as subsequent projections come. Dynamic CS is a continuous optimization that accommodates extra restrictions introduced by fresh projections.

CS has the potential to revolutionize low dose imaging, and its application in STEM has been explored using Bayesian dictionary algorithms. The algorithms were applied to a set of under-sampled images, where the number of pixels was reduced to 5% of the original. Despite this substantial reduction, the algorithms successfully reconstructed the original picture, showcasing their effectiveness in dealing with under-sampled pixel data. The post-acquisition image alterations could be immediately applied as a low-dose acquisition approach without changes to the electron optics or the microscope's alignment.[80] It is proposed that a coded aperture CS can integrate a series of images into a frame after decompression according to the extent of damage, rather than recording both damaged and undamaged part in the same image (Fig. 8a–c).[78] This method can help rebuild the precise commencement of radiolysis, and allow for a speedup of more than an order of magnitude.[81] The corresponding methodologies to realize the CS in this manner include blanking the incident electrons between two lighted pixels or guiding the scanning coils in a certain way to leap from one illuminated pixel to a nonadjacent subsequent pixel.[79] Efficient random sampling can reduce the dose for atomic-resolution images by at least 5 times (Fig. 8d–f). In addition to the slump in accumulated dose (even lower than 1 e $Å^{-2}$) for atomic resolution, the sub-sampling method exhibited a faster acquisition rate, exceeding 10 times, as well as enhanced resolution.[73] These advantages ensure a more realistic determination, especially for the *in situ* observation which can last quite a long time.[82] The subsampled method minimizes the interference of the external incident beam in *in situ* observation, and can illustrate the most actual reaction process at spatial/temporal resolution.

3.3 Innovations in computational processing and analysis

The low dose technique has flourished with the constant development of detectors and imaging technologies, enabling reliable acquisition of images at atomic resolution. However, partial images are still affected by a trade-off in decreased SNR. Therefore, post-processing techniques such as denoising have become crucial for rigorous and compressive measurements to extract the information from unimpressive and low contrast regions. In the conventional approach, adaptive nonlinear

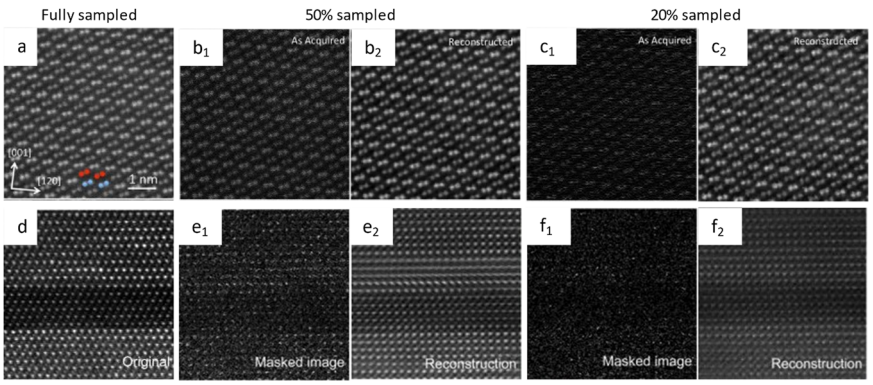

Fig. 8 The schematic illustration of CS and the reconstructed images. Images of $NiTiO_3$ acquired under (a) fully, (b) 50%, and (c) 20% sampled conditions. Reproduced with permission.[78] Copyright 2016, AIP Publishing. Images of the complex perovskite sample acquired under (d) fully, (e) 50%, and (f) 20% sampled conditions. Reproduced with permission.[79] Copyright 2016, AIP Publishing.

Open Access Article. Published on 21 March 2024. Downloaded on 1/15/2026 6:48:41 PM. This article is licensed under a Creative Commons Attribution-NonCommercial 3.0 Unported Licence.

filters utilize local SNR to calculate a suitable factor ratio for eliminating noise from an image contaminated by a mixture of indistinct additive random noise. This methodology guarantees the preservation of edge details while mitigating noise interference. Furthermore, the phase retrieval, which can reconstruct the fully structured images with phase information, has also seized the opportunity to apply the computer technique in the complicated mathematical reconstruction. The resulting images through post-processing techniques match well with the realistic structure at the atomic level.[32] Finally, to decipher these images, deliberate simulations taking into consideration the interaction between incident electrons and atoms are required to interpret the experimental measurements. The combination of low dose techniques, advanced post-processing, and sophisticated simulation has facilitated the acquisition of atomic-resolution images with exceptional detail and precision.

3.3.1 Denoising. The obtained image in imaging techniques frequently represents a degraded version of the latent observation owing to various factors including noise contamination and illumination. Additionally, the unidentified latent observation also introduces noise throughout the transmission and compression procedures. To eliminate the noise and retrieve the latent observation from the provided damaged image, various filters and algorithms have been developed and have shown effective denoising ability. In the 1990s, post-processing methods based on both real space and Fourier space were utilized to enhance the SNR of TEM images.[83] A signal adaptive mask was generated from the Fourier filtering procedure to accurately classify effective signal and noise. Another Wiener-filter method was proposed to reduce noise without bias from different places in Fourier space. The parametric Wiener filter produced robust and reliable results in qualitative and quantitative evaluation and enhanced SNR.[84] The *a priori* knowledge of continuous and circular atoms allowed for an improvement of 30% in SNR.[85] To simultaneously detect the periodic columns and non-periodic deviation from imperfect crystals, a nonlinear filtering algorithm was proposed as an iterate product of the Wiener filter.[86] It can provide significant suppression without obvious artifacts even with massive noise, making it suitable for quantitative analysis and imaging beam sensitive materials. Denoising in 4D STEM, which involves mass data and involute noise distribution, is more challenging. Zhang *et al.*[87] utilized the tensor singular value decomposition method, which can record all information for multi-spatial dimension exploration, to directly denoise atomic 4D STEM data. This method demonstrated comparable performance, while using less computation time and memory, making it even suitable for desktop usage.

3.3.2 Phase retrieval and ptychography. The conventional detectors record the intensity of signals as the square of the amplitude of the electron wave but lose the phase information. The reconstructed images are 2D projections instead of accurate representations of the realistic structure of the specimen. To address this limitation, a filtering process is performed in the reciprocal space, which enables the mathematical reconstruction of the image wave and the retrieval of phase information. In the 1990s, holographic methods were applied to phase retrieval using neural networks, which allowed for avoidance of the prerequisite of fine hologram fringes and artefacts in conventional methods. These neural network-based methods could reduce the error caused by noise corruption and improve the quality of acquired images.[88,89] This iterative phase retrieval employed *a priori* knowledge of several parameters: for instance, that the intensity of diffraction patterns is the square of the Fourier transform, and that there is a zero-value region out of the interested area, as well as the knowledge of atomicity, among others. Ptychography, which records the information of reciprocal space by utilizing an overlapped illumination probe to scan the specimen, also shows great potential. Combining with transverse translation diversity, the nonlinear optimized ptychographical iterative engine (PIE) algorithm has allowed the refinement of inaccurate parameters and yielded robust reconstruction.[90] Furthermore, the extended PIE algorithm updates the object and probe estimates as each diffraction pattern is taken into account, thereby exhibiting a quicker convergence rate and higher noise robustness.[91]

Additionally, this approach offers more flexibility in adjusting illumination according to practical conditions. Broek *et al.*[92,93] successfully retrieved the 3D potential of a specimen using a neural network based on the multislice strategy for a non-heuristic treatment of the modulation transfer function. In their further investigation, a similar treatment involving the combination of forward-simulation algorithms was conducted to recover the 3D structure from CBED patterns.[94] The versatile algorithm is theoretically suitable for other parameters associated with the interaction between the electron beam and the specimen, especially for limited measured disks with realistic noise even in the cases where there is a mismatched mean intensity.

3.3.3 Image simulation. Simulation is a powerful tool in (S)TEM for deciphering actual acquired images or generating forecast before testing, which is vital for the estimation of element species and related quantification. Several factors affect the image quality, including the specimen thickness and orientation, lens aberrations, and microscope stability. Simulation methods can comprehensively compute the exit-plane wave function from the incident electron and the projected potential of the sample. Two methods, Bloch wave and multislice approaches, are mainly used to simulate the scattering process. Based on solving the Schrodinger equation, the Bloch wave approach employs a matrix to represent the scattering ability of a sample and compute the exit wave. The method enables direct visualization of the atomic column positions or other repeated slab structures of a zone-axis-aligned specimen, exhibiting good agreement with experimental images.[95–97] In contrast, the multislice method simplifies the interaction between electrons and a thick specimen by dividing the specimen into a series of thin slices. In each slice, it assumes that the kinematical scattering holds. The exit wave generated from the interaction between the incident wave and the last slice can propagate to the subsequent slice, ultimately generating the final signal. In addition, the multislice method enables the introduction of a deviation in a specific slice without influences on other slices,

 This journal is © The Royal Society of Chemistry 2024

Open Access Article. Published on 21 March 2024. Downloaded on 1/15/2026 6:48:41 PM. This article is licensed under a Creative Commons Attribution-NonCommercial 3.0 Unported Licence.

which provides a flexible processing mode for inhomogeneous specimen. Meanwhile, the frozen phonon model can be incorporated into the multislice method by shifting the atoms about their equilibrium locations in accordance with the Debye–Waller factor. Similar to the splitting strategy in the multislice method, a layer-by-layer Bloch wave approach was applied to modify the provided submatrix to the relevant configuration for the calculation of thermal scattering, which is also propitious to nonperfect crystals with defects.[98–101] Furthermore, some efficient algorithms have been proposed by combining Bloch wave and multislice methods. In these algorithms, the multislice method worked for the calculation of a subset in a scattering matrix, and the Bloch wave method worked for the following calculation processing.[102] The plane wave reciprocal space interpolated scattering matrix algorithm exhibited negligible error in the short calculation time compared with the conventional multislice simulation. A probe partitioned method by interpolating original functions was further introduced, which decreased the usage of random access memory as well as maintained a balance between accuracy and simulation time.[103] An iterative neural-network-optimization-based algorithm integrated with the density functional theory (DFT), which can predict the information associated with the charge density around the atom, has been shown to provide a more accurate result with less calculation time.[104]

Simulation is a time-consuming process with multiple central processing unit cores, especially for models with thousands of atoms. The combination with intuitive GPU can significantly decrease the calculation time, even on a desktop computer.[105–108] Several open source codes or software, such as QSTEM,[109] STEM_CELL,[110] MULTEM,[106] FDES,[107] EMsoft,[111] Prismatic,[112] Dr. Probe,[113] and ToTEM,[114] have been developed for practical simulation.

Additionally, the introduction of CS technologies, which are successfully applied in TEM imaging, has also promoted the development of simulation. The sub-sampling method for signal acquisition and subsequent recovery of missing information using inpainting algorithms show great potential to combine with STEM simulation for an agreement with the simulated images from the fully sampled mode.[115,116] This advanced method can significantly reduce the simulation time, as well as the electron dose for sensitive materials. Further CS methods have been proposed to sample each layer in the frozen phonon model at a much lower ratio, which may allow for real-time STEM simulation.[117]

3.4 Innovations in specimen protection

Innovations in (S)TEM instrumentation and computational techniques have focused on image acquisition and processing to address fundamental factors. The successful application of these techniques has ensured comparable imaging quality at a lower dose of several orders of magnitude, ranging from 10^{10} to even below 10 e $Å^{-2}$. As a vital method for preparing specimens with suitable thickness, the focused ion beam (FIB) method may introduce ion beam damage into materials. Therefore, a cryogenic system has been introduced to the conventional FIB to minimize the damage. Additionally, at ultra-low electron dose, any measures to prolong the dwell time will enhance the imaging quality. Hence, coating of the specimen with a protective layer can remarkably reduce the amount of surface sputtering, and effectively delay the beam damage.

3.4.1 Electron transparent sample preparation developments. The thickness of the specimen for (S)TEM imaging is typically required to be under 100 nm to satisfy the weak phase object approximation and minimize dynamical scattering. However, the thickness of a sample can vary widely depending on its reaction conditions, ranging from several nanometers to millimeter-scale. The sample analysis often relies on complex deconvolution to investigate local interfaces from information perpendicular to the interface. This requires a method to process the sample parallel to the incident electron.[118] A conventional method for processing samples in TEM, known as ultramicrotomy, is commonly employed to mechanically section samples into thin pieces.[119] This technique involves embedding the sample in resin and subsequently sectioning using a diamond knife, which can achieve a thickness less than 15 nm. The ultramicrotomy technique offers a distinct advantage in terms of sample throughput, as it enables the expeditious preparation of multiple thin sections within a relatively brief timeframe. It has found widespread application in the preparation of biological specimens[120,121] organic solar cells,[122] battery cathodes[123] and polymers.[124] It is also reported in the fabrication of polymer mixed matrix membranes with MOFs.[125] However, the monitoring of sectioning and the site selectivity of ultramicrotomy can be challenging,[122] and more importantly, the mechanical sectioning steps may introduce residual stress, impacting the determination of high resolution information.[126] The FIB method has been explored for slicing off an electron-permeable membrane from a particular region of interest in bulk samples.[127,128] The FIB method performs well in slicing specimens with different morphologies and components, such as silicon and ZnSe optical ceramics.[129] It provides a versatile technology to determine interfaces and regions of interest in bulk samples. However, its application remains limited when it comes to beam-sensitive materials, as the ion beam, even at a limited voltage and current, may introduce damage and obscure images.

The cryogenic system, a routine method used in TEM for characterization of biological specimens, has been integrated into FIB to process the beam-sensitive samples.[130–132] It has been shown that the samples fabricated by cryo-focused ion beam (cryo-FIB) milling have negligible devitrification and artifacts compared to those obtained by conventional cryo-ultramicrotomy. Cryo-FIB milling is simpler and requires less specialized personnel than cryo-sectioning, making it widely applied in cryo-TEM.[133–135] Similar protection from ion beam damage has also been explored in polymer films that suffer from beam heating due to low conductivity. The results showed enhanced tolerance to beam current by nearly 10 times.[136]

The successful use of cryo-FIB in battery materials inspired the investigation of its applications in beam-sensitive materials.[137] Cryo-FIB minimizes surface damage and re-deposits of Li-metal materials by freezing samples at −170 °C throughout processing, which solves the sensitivity, artifact

Open Access Article. Published on 21 March 2024. Downloaded on 1/15/2026 6:48:41 PM.
This article is licensed under a Creative Commons Attribution-NonCommercial 3.0 Unported Licence.

difficulties, and mechanical deformation of conventional sample cross-sectioning, as well as allowing for a quantitative evaluation of deposited Li (Fig. 9c and d).[138,139] Cryo-FIB has also been applied to the processing of metals and their alloys,[140] solid–liquid interfaces and reactive materials,[141] solar cells,[142] and more.[143,144] Recently, pioneering work on the application of cryo-FIB in ultra-sensitive materials, MOFs and hybrid halide perovskites was reported (Fig. 9a and b).[145] It maintained perfect crystallinity at 16 kV compared to total crystallinity loss at room temperature (Fig. 9e and f). Furthermore, the universality of cryo-FIB was investigated in the determination of MOF–COF core–shell structures.[146] This approach effectively preserves the crystallinity of the materials throughout the process. Cryo-FIB also enabled orientation predetermination, which is particularly relevant for materials with various constituents or preferred orientations.

3.4.2 Specimen coating. Coating is a well-established method to combat radiation damage in insulating materials. It can act as an electron pathway that compensates for the charging effect, a thermal conductor, and a shield against sputtering. However, coating often has the unintended consequence of obscuring the specimen itself, lowering the SNR, and thus decreasing the achievable resolution. Hence, the ideal coating material should be crystalline, chemically inert, highly transparent to electrons at the employed energy, resistant to thermal expansion and contraction, and possess good electrical and thermal conductivity. In early investigations, C or Al films were used, and the fading rate of diffraction patterns exhibited an improvement of 3–5 times.[147] The poly(vinylpyrrolidone) polymer has been used to stabilize silver nanoparticles in TEM and functioned as a diffusion barrier to inhibit surface diffusion and filament production.

Graphene, which exhibits significant protective capability as a chamber for bacterial cell observation[148] and in ion irradiation,[149] may enhance the resistance of materials to electron damage. It has been reported that the radiation resistance of the initial single layer of MoS_2 was improved by three orders of magnitude through coating two graphene layers to form a sandwich layered structure, which allows for pristine atomic inspection of MoS_2.[150,151] The subsequent successful application of this strategy in the atomic characterization of $MoTe_2$,[152] phosphorene,[153] and perovskites[154] demonstrates that coating can remarkably enhance stability. It has been mentioned that the edge of the sandwich sample is less stable than the interior area, and may transform into an amorphous structure first.[152] Molecular dynamics simulations based on separation of the dimension and encapsulation have revealed substantial cooperation in toleration to radiolysis. The simulation results showed a hundred-fold increase in resistance from 3D to 1D.[155] Therefore, the combination of sample functionalization, encapsulation, and advanced low dose imaging technologies may provide a viable approach to investigate the structure and dynamic behavior of materials at atomic resolution over long time periods.

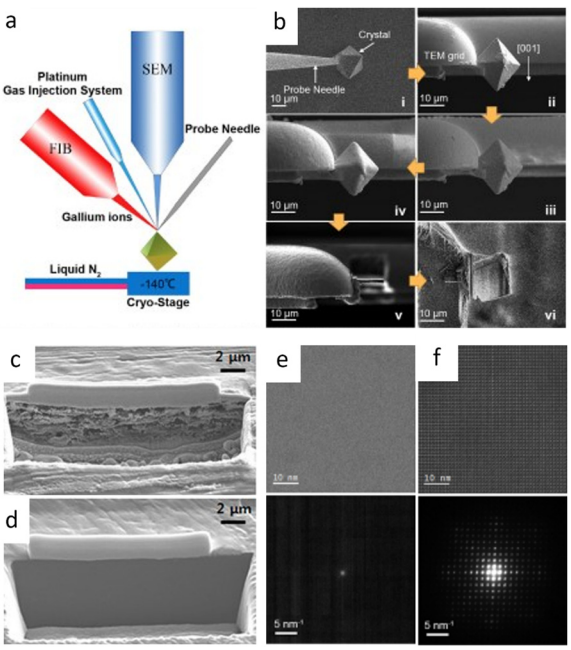

Fig. 9 Cryo-FIB for sample preparation. (a) Scheme of a cryo-FIB dual-beam system. (b) Workflow of cryo-FIB. Reproduced with permission.[145] Copyright 2013, AIP Publishing. (c, d) The SEM image of cross-sectioned Li foil at (c) room temperature and (d) cryogenic temperature. Reproduced with permission.[139] Copyright 2019, American Chemical Society. (e, f) HRTEM image and the corresponding electron diffraction pattern of HKUST-1 prepared at (e) room temperature and (f) cryogenic temperature with 16 kV ion beam for milling. Reproduced with permission.[145] Copyright 2013, AIP Publishing.

4. Current implementations in COMs

The utilization of a diverse range of organic groups has significantly broadened the spectrum of MOFs and COFs. Various chemical reactions are employed for linkage formation, leading to morphologies ranging from 0D to 3D. The frameworks demonstrate diverse applications, including gas capture and separation, photocatalysis, electrocatalysis, and device fabrication. Accurately determining the atomic-scale skeleton of these frameworks is crucial to establish the relationship between structure and performance, which can enhance understanding of the fundamental principles of physics and chemistry and facilitate the design of functionalized materials with specific properties. The recent rapid development of low dose (S)TEM imaging techniques has demonstrated an unprecedented opportunity for the determination of the atomic-scale structure of MOFs and COFs in multiscales and multidimensions. These techniques have enabled the observation of details such as atomic defects, host–guest interaction, and surface structures, with a resolution previously unattainable.

4.1 HRTEM

4.1.1 Bulk structure elucidation. In earlier research, HRTEM was the primary technique for determining the atomic structure of MOFs. Unlike STEM, which uses a converged electron beam, HRTEM employs a parallel electron beam in

 This journal is © The Royal Society of Chemistry 2024

Open Access Article. Published on 21 March 2024. Downloaded on 1/15/2026 6:48:41 PM.
This article is licensed under a Creative Commons Attribution-NonCommercial 3.0 Unported Licence.

TEM imaging and therefore causes less destructive damage prior to the development of low dose technology. It was not until 2015 that direct imaging of the giant pore of MOFs was achieved.[156] The cubic symmetry of MIL-101 was studied by keeping the electron dose and magnification as low as possible and two main zone axes [111] and [011] of the $Fd\bar{3}m$ space group were presented. Since then, HRTEM has gradually become a routine characteristic method to verify the crystal structure of MOFs and for further elucidating the local structure.[34,157,158] For example, a pyridine-stabilized MOF exhibited improved resistance to electron irradiation due to the introduced pyridine units.[157] In Fig. 11a, HRTEM images of 2D hexaaminobenzene-derived MOFs were taken with a low dose rate of 1 e $Å^{-2}$ s^{-1}.[159] The honeycomb array with holes smaller than 1 nm, as predicted by the 2D eclipsed packing model from PXRD, was validated by HRTEM images. Complementary strategies, including DEDs, automated zone axis search, image alignment, and calculation of the defocus value, were used to decrease the cumulative dosage for time-consuming modification required under ideal imaging conditions.[41] The use of an ultra-low dose of 0.033 e^{-1} per pixel in each frame ensured that the acquisition was completed before damage occurred. As shown in Fig. 10, HRTEM images with high SNR were in excellent agreement with the crystal structure of UiO-66, which consisted of triangular channels encircling metal clusters and 1,4-benzenedicarboxylic acid (BDC) linkers, as well as Zr atomic columns inside the Zr_6O_8 clusters.

Low-dose HRTEM enables the determination of the exact atomic structure of MOFs with discernible defects for specific functions related to defect engineering.[160] Low-dose HRTEM images in Fig. 11e–g revealed the coexistence of "missing linker" and "missing cluster" structural defects from distinct projections and electron crystallography. In the presence of the prevailing missing-linker defect, UiO-66 experienced a topological transformation from a face-centered cubic to a body-centered tetragonal structure. In contrast, missing cluster defects only manifest themselves in a constrained space and result in two different underlying topologies of **reo** and **scu** net. The defect tuning technique enables an intuitive investigation of the relationship between defects and catalytic performance. As an example, Chen *et al.*[161] doped Ni into Zn-MOFs based on the assumption that the square-planar coordinated Ni^{2+} could only replace the Zn on the crystal surface. A crisp image of (110) facets in rhombohedral dodecahedron crystals, together with energy-dispersive X-ray spectroscopy (EDS), was used to calculate the number density of metal atoms, indicating a density of 0.5Ni atoms per square nanometer.

Low dose HRTEM, in conjunction with advanced cryo-FIB techniques, provides more details about the intrinsic structure of MOFs, and allows for comprehensive reconstruction of their 3D structure.[145] In the determination of defects in MOF HKUST-1, ultralow-dose HRTEM images showed that an interpenetrating structure would form due to the overlap of two sets of lattices after the split and shift of a single crystal, resulting in a locked boundary with a distance of 3.2 Å. Robison *et al.*[162] designed a non-interpenetrated Zr cluster-based MOF, and determined the structure of original NU-1200 and its evolutive interpenetrated STA-26. They created a script to extract the

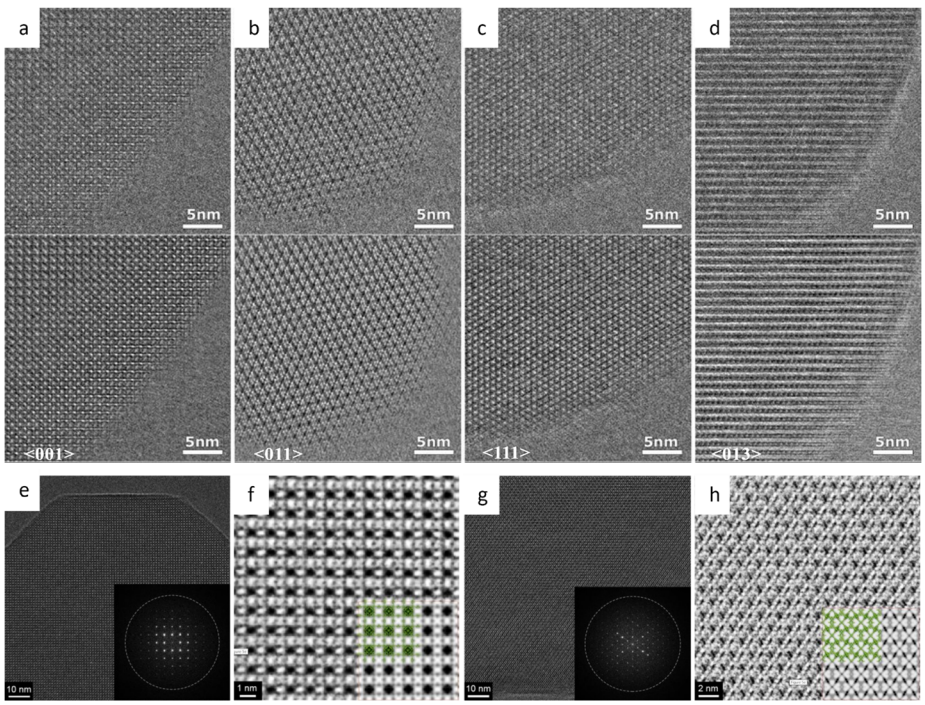

Fig. 10 The low-dose HRTEM images of MOFs. (a)–(d) The raw (top) and denoised (bottom) images of UiO-66 from different zone axes. (e) Drift-corrected, and (f) CTF-corrected and Wiener-filtered images of ZIF-8. (g) Drift-corrected, and (h) CTF-corrected and Wiener-filtered images of HKUST-1. Reproduced with permission.[41] Copyright 2018, The American Association for the Advancement of Science.

Open Access Article. Published on 21 March 2024. Downloaded on 1/15/2026 6:48:41 PM.
This article is licensed under a Creative Commons Attribution-NonCommercial 3.0 Unported Licence.

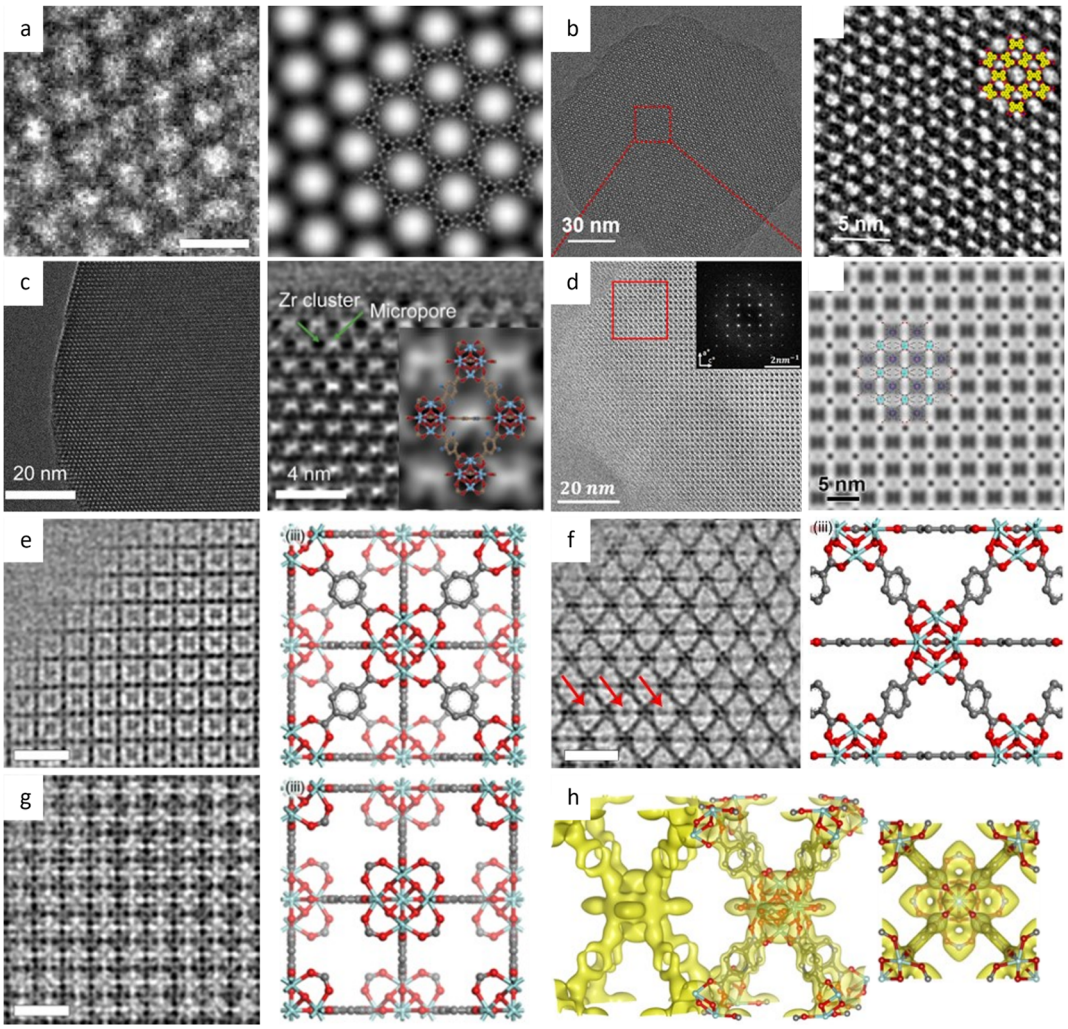

Fig. 11 The low-dose HRTEM images of MOFs. (a) The raw image, and symmetry-imposed and lattice-averaged image of Cu-/Ni-HAB MOFs. Reproduced with permission.[159] Copyright 2018, Springer Nature. (b) Images of ***kgm***-TBA-MOF. Reproduced with permission.[165] Copyright 2023, American Chemical Society. (c) The raw image and CTF-corrected image of UiO-66-NH_2, inset: model of UiO-66-NH_2. Reproduced with permission.[164] Copyright 2023, Elsevier Inc. (d) Image of PCN-226(Cu) along the [010] direction with the corresponding Fourier transform, and symmetry-imposed image. Inset: Model of PCN-226(Cu). Reproduced with permission.[170] Copyright 2020, American Chemical Society. CTF-corrected images of UiO-66 along the (e) [001], (f) [110], and (g) [001] zone axes. (h) Reconstructed 3D electrostatic potential map from different directions. Reproduced with permission.[160] Copyright 2019, Springer Nature.

Fourier transform of the area of interest and employed statistical methods to determine the predominant form based on the relative intensity ratios. The results indicated that once an interpenetration transition is initiated, it happens swiftly and thoroughly. A novel Fe-MOF, DNF-9, showed fluorinated metal nodes packed in an alternating helical pattern based on HRTEM images.[163] At an ultra-low dose rate of 0.03 e $Å^{-2}$ s^{-1}, the structure of the UiO-66-NH_2 derivative was determined.[164] The resulting highly crystalline structure with octahedral morphology clearly showed Zr_6O_8 clusters with abundant defects caused by missing linkers as shown in Fig. 11c.

To increase the interlayer π–π contacts, a flexible non-planar molecule with a large molecular size core was utilized to synthesize the 2D conductive MOFs.[165] For instance, the ***sql***-TBA-MOF with a single pore showed a nanorod morphology with a lattice fringe distance of 1.52 nm for the (110) plane, while the ***kgm***-TBA-MOF with a kagome topology with hexagonal and triangular dual pores featured a hexagonal nanoflake morphology with a lattice fringe distance of 2.6 nm for the (100) plane (Fig. 11b), demonstrating the viability of the topological control method. Sun *et al.*[166] reported a kind of nanowire-liked MOF with a pore size of 1.4 nm at a dose of 1.5–5.6 e $Å^2$. Another type of nanowire-like MOF, Zn-HHTP-H_2O, synthesized from octahedral Zn(II), exhibited an AB stacking model and a honeycomb structure with a width of 12 Å in the [001] direction.[167] Taking a novel approach to integrate Ni–S into the coordination links, a bamboo-leaf-like Ni(DMBD)-MOF was synthesized, and the lattice fringe distance of the contained crystal nanosheets could be recognized as 9.5 Å from a side view.[168] Furthermore, the HRTEM images displayed a distinct (010) twin border along the [101] and [101] zone axes. Gong *et al.*[169] combined TEM imaging (dose around 10 e $Å^{-2}$) with

 This journal is © The Royal Society of Chemistry 2024

Open Access Article. Published on 21 March 2024. Downloaded on 1/15/2026 6:48:41 PM.
This article is licensed under a Creative Commons Attribution-NonCommercial 3.0 Unported Licence.

metalation of linkers to differentiate between porphyrinic MOFs that would be indistinguishable by other methods.

A technique based on the use of Zr-chains was developed for high chemical and redox stability, and to tune the separation of redox active sites at an optimal density.[170] The HRTEM images in Fig. 11d revealed rectangular packing along [010] with an interplanar spacing d_{200} of 18.32 Å, which matched well with the simulation model. To solve the limited processability of MOF powders, a new approach was developed that involved the hybridization of block copolymers with active sites for metalation with MOFs through self-assembly.[171] The alternate layered structure corresponding to the Zr-rich or Zr-deficient regions could be identified, and the building unit results in a lamellar structure with a width of about 4.2 nm.

Identifying the structure of COFs encounters more challenges due to their poor crystallization and substantial overlap. A two-step seeded approach was proposed to fundamentally resolve the inadequate controllability of nucleation and growth processes.[172] This approach polymerizes monomers to create crystalline COF nanoparticles as seeds. The gradual addition of more monomers controls the second polymerization, resulting in single crystalline COFs with large domains. By separating the processes, growth occurs on the surface of existing nanocrystals instead of new particles. As a result, the targeted COFs presented single crystal domains with size up to 1.5 μm. At a total dose of 26.5 e $Å^{-2}$, COF-5 showed lattice fringes consistently and continuously extending from edge to edge. Intriguingly, despite possessing a comparable hexagonal structure and continuous crystalline domains, COF-10 exhibited a preference for orientation stacking perpendicular to the substrate. This method was subsequently extended to synthesize the single-crystalline boroxine-linked 2D and 3D COFs through the dehydrative trimerization of polyboronic acids.[173] The single-crystalline nature of the 2D and 3D samples was clearly identified while a variation existed in the interlayer distance for stacking offset in the 2D crystals.

Due to the poor conjugation of boroxine COFs, colloidal COF nanoparticles connected by imine were synthesized for photoelectronic applications.[174] HRTEM imaging revealed that TPB-MeOTP-NP and TPBMeOTP-NS had identical honeycomb networks but with a plate-like and spherical morphology, respectively. The centimeter-scale homogeneous films fabricated using the COF nanoparticles were incorporated in photoelectrodes for photoelectrochemical solar-to-hydrogen conversion, and their performance was comparable to the best performance of conventional semiconductor-based photocathodes.

Imines are the most prevalent and adaptable class of COFs, and they are intensively researched to determine an effective strategy to produce high-quality COF single crystals under moderate conditions. Single crystals of 2D COFs with a size range of 4–20 μm were produced by the solvothermal method in only 5 minutes.[175] Constant lattice fringes extending from edge to edge of the platelets indicate the integrity of the single crystal. The inter-lattice fringe distances were measured to be 24.0 Å and 31.5 Å for TAPPy-PDA and TAPB-DMPDA, respectively. After inserted into gas chromatography separation columns, single-crystalline COFs showed a considerable increase in efficiency and selectivity compared to polycrystalline COFs, indicating the importance of the highly ordered structure. In a recent study, inverse pulse gas chromatography was used to quantitatively characterize the physiochemical adsorption properties of these 2D COFs.[176] The results demonstrated that the single-crystalline TAPPy-PDA COF exhibited a nonpolar and electron donor character, whereas the reference polycrystalline sample exhibited a mild polar and electron acceptor character.

The facile synthesis of imine-based COFs permits a direct comparison of the alterations in properties resulting from structural isomers, such as the orientation of the C=N bonds.[177] In contrast to its isomer, the TAPAPDA COF exhibited perfect reversibility in phase transition involving the slip-stacking model of the β phase, coupled with a high solvatochromic feature. The imine linkages also permit the introduction of antiaromatic compounds for intriguing attributes, such as a low HOMO–LUMO energy gap.[178] Dibenzopentalene-based building blocks with an antiaromatic 4n π-conjugated structure are stable in both oxidized and reduced states, making them suitable as electrode materials. The crystalline nature of the COFs is demonstrated by rod-shaped crystals with constant (200) lattice fringes of 1.24 nm, enabling a higher capacity as a positive electrode material in Li-organic batteries (26 mA h g^{-1}) compared to amorphous DBP-Ph-TFP POP (14 mA h g^{-1}). The imine linkages could also be transformed to more resistant quinoline linkages while preserving the original topology and porosity.[179] HRTEM images (Fig. 12a–d) at a cumulative dose of 2.1 e $Å^{-2}$ revealed an ordered hexagonal projected symmetry with a pore size of approximately 3.0 nm. After the transformation through cycloaddition, the pore size suffered a modest drop to around 2.3 nm while maintaining its original structure. The quinoline aromatic ring-linked COFs displayed significantly increased stability against strong acids and bases. The intramolecular Povarov reaction that can transform imine linkages to more stable chromenoquinoline moieties was also applied in the formation of crystalline COFs with ladder-type linkages from single-strand-type linkages (Fig. 12e–h).[180] In addition, transformation *via* the three-component Doebner reaction has been applied to synthesize stable crystalline COFs.[181] The resulting COFs with an interplanar *d*-spacing of 0.34 nm in HRTEM images exhibited superior crystallinity and stability compared to imine COFs. To construct COFs with pre-designed topology, introducing molecular linkers with variable conformation has been developed to provide an extra degree of freedom for the topologies.[182] As shown in Fig. 13a–i, two distinct COFs were synthesized using TPE links: one with a dual-pore kagome topology (TPE-COF-OH) and the other with a single-pore rhombic topology (TPE-COF-OMe). HRTEM images revealed a star-shaped hexagonal project structure in TPE-COF-OH, featuring a triangular channel with a pore size of 7 Å and a hexagonal channel with a pore size of 27 Å. In comparison, a rhombic-shaped projected structure was observed in TPE-COF-OMe, with a pore size of 12 Å.

By selecting monomers with the highest C_6-symmetry, researchers designed COFs with ***kgd*** topology that could lead to the smallest pore size.[183] HRTEM images in Fig. 12i–k revealed a honeycomb pattern with a decreased *p*3 symmetry

Open Access Article. Published on 21 March 2024. Downloaded on 1/15/2026 6:48:41 PM.
This article is licensed under a Creative Commons Attribution-NonCommercial 3.0 Unported Licence.

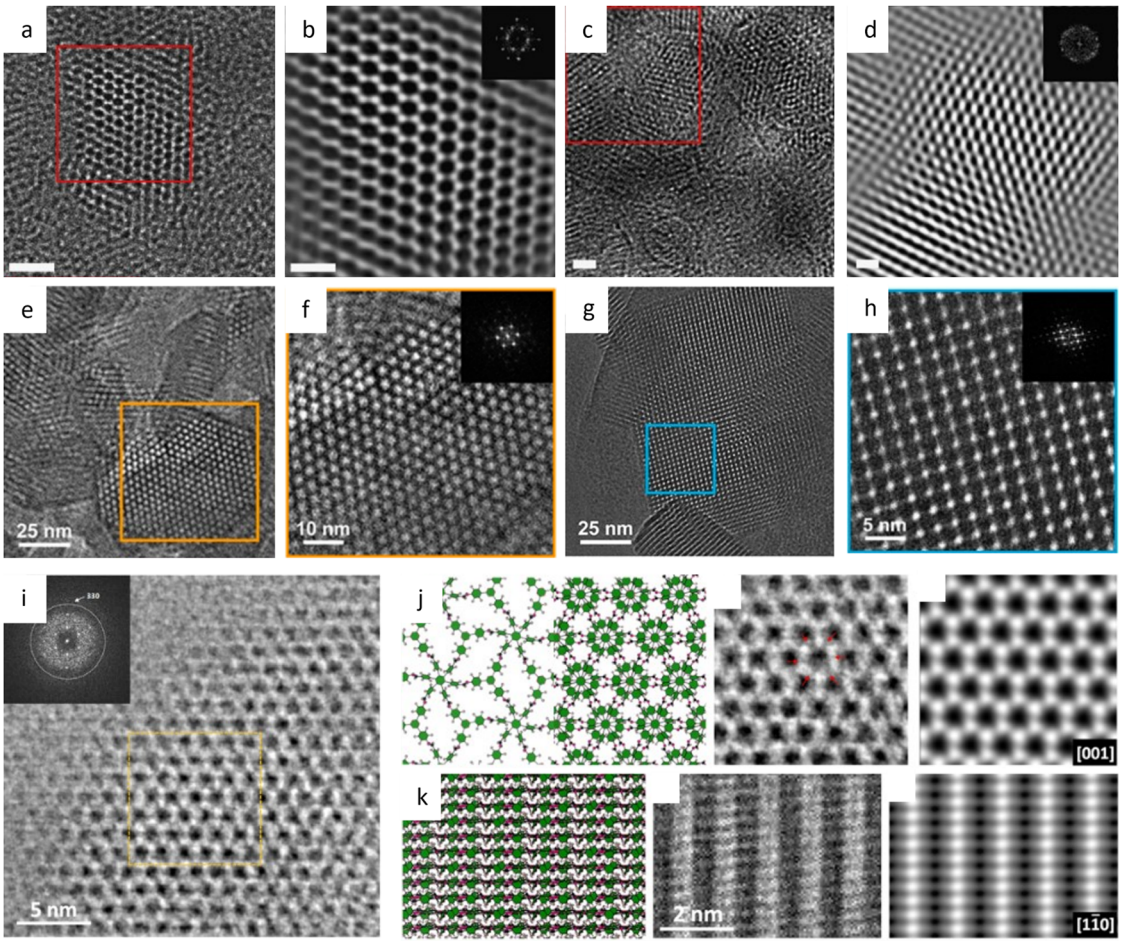

Fig. 12 Low-dose HRTEM images of COFs. (a) High-resolution image and (b) Fourier-filtered image of COF-1. (c) High-resolution image and (d) Fourier-filtered image of MF-1a. Reproduced with permission.[179] Copyright 2018, Springer Nature. (e) and (f) Images of CQ-$COF_{TAPB-BPTA}$. (g) and (h) Images of CQ-$COF_{Py-BPTA}$. Reproduced with permission.[180] Copyright 2022, American Chemical Society. (i) CTF-corrected image of HFPB-TAPT. (j) Single-layer and ABC stacked model along the [100] direction, enlarged image from (i), and simulated image (from left to right). (k) Structural projection along the [1$\bar{1}$0] direction, raw image, and simulated image (from left to right). Reproduced with permission.[183] Copyright 2022, American Chemical Society.

in the [001] direction, indicating a more stable configuration, as well as a distinguishable ABC stacked structural projection in the [110] direction. HFPB-TAPT, with the smallest pore size of 6.5 Å, exhibited the maximum loading quantity and excellent release characteristics in drug delivery. Recently, a set of distinctive COFs comprised of mechanically interlocked catenanes have been constructed to investigate the facilitating dynamics of such an interlocked structure (Fig. 13k–n).[184] An unprecedented [∞] mechanically linked framework in COFs is realized by an infinite 3D arrangement of the alternately linked tritopic linker and tetrahedral $Cu(PDB)_2BF_4$. The spots in catena-COF-805 are aligned in a zigzag pattern along the $\langle 1\bar{1}0 \rangle$ direction, but they are aligned in a straight line in the other two samples, which may be due to the unit-cell doubling in catena-COF-805. All three COFs display a doubly interpenetrated ***bor***-y topology, while the space group of catena-COF-805 is identified as $F4_132$, whereas catena-COF-806 and 807 are $P4_232$. To prevent the reduction of surface area due to interpenetration in topologies like ***pts***, innovative 3D COFs based on the ***stp*** topology with non-interpenetration have been developed.[185] These COFs exhibited both high surface area and exceptionally low crystal density. The HRTEM images clearly showed channels with a hexagonal structure, and the (100) and (010) reflections had a *d*-spacing of 4.65 nm, which is in good agreement with the proposed structural model.

4.1.2 Nanosheet structure elucidation. The ultra-thin 2D nanosheets, which can be exfoliated from parent 3D MOFs, have many novel properties. However, atomic-resolution imaging of such materials remains challenging due to their fragile structure and limited reflection intensity at such thin thickness. To achieve a more stable structure, layered Ln-MOFs with high-valent Ln(III) have been exfoliated into 2D nanosheets with a thickness of around 6 nm.[186] With a modest dose of 20 e $Å^{-2}$, the clusters and ligands can be easily discerned from the HRTEM images in Fig. 14a–c. Interestingly, when interlayer binding is weak enough, the layers can slide relative to each other, leading to disordered stacking and the loss of periodicity in one dimension. A novel layered MOF (IPM-1) connected by cage-like linkers is not robust enough to withstand external stimulus. As a result, the material maintains an in-plane 2D ordered structure without

 This journal is © The Royal Society of Chemistry 2024

Open Access Article. Published on 21 March 2024. Downloaded on 1/15/2026 6:48:41 PM.
This article is licensed under a Creative Commons Attribution-NonCommercial 3.0 Unported Licence.

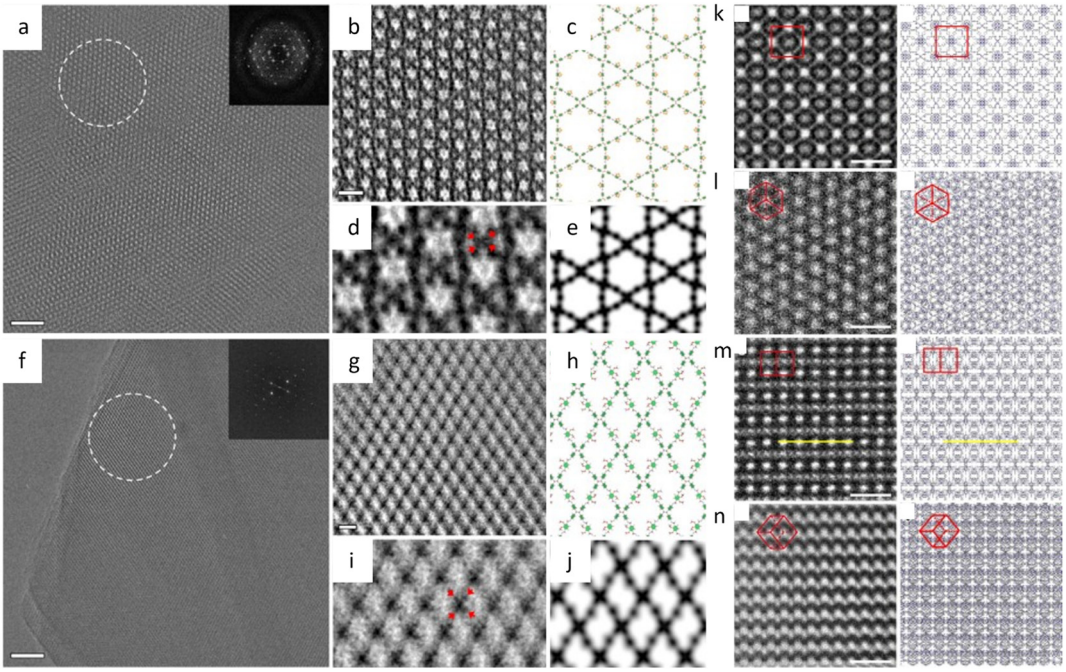

Fig. 13 Low-dose HRTEM images of COFs. (a) Raw image, (b) CTF-corrected image, (c) structural model, (d) motif-averaged image and (e) simulated image of TPE-COF-OH. (f) Raw image, (g) CTF-corrected image, (h) structural model, (i) motif-averaged image and (j) simulated image of TPE-COF-OMe. Reproduced with permission.[182] Copyright 2020, American Chemical Society. Images and projections of catena-COF-806 along the (k) [001], (l) [111], (m) [1$\bar{1}$0], and (n) [$\bar{1}$12] direction. Reproduced with permission.[184] Copyright 2023, Springer Nature.

alignment in the stacking direction.[187] This seemingly contradictory structure is supported by the amorphous-like pattern from PXRD of the bulk sample, and the clear lattice fringes and electron diffraction pattern in HRTEM images. In addition to exfoliated 2D nanosheets from a parent bulk sample, another strategy to derive 2D MOFs from delaminated 2D precursors has been developed. The 2D MXene was initially prepared by etching the Al layer in the layered MXene, providing active sites for chemical transformation into MOFs.[188] The resulting V_2CT_x-PMOF exhibited decent stability inherited from the original crystal structure, and the HRTEM images showed a well-ordered cubic structure along the ⟨100⟩ zone axis, which corresponded well with the simulated results.

Additionally, a bottom-up strategy based on building block design has been proposed to synthesize 2D MOFs, taking cues from the finding that incorporating a larger proportion of the π-conjugated structure into the skeleton will enhance non-covalent interactions.[189] By choosing a large, electron-deficient ligand core with lower electron density, direct synthesis of 2D MOFs with improved in-plane crystallinity has been achieved. The HRTEM images in Fig. 14e–g exhibited a long-range ordered array with a pore size of 2.1 nm, which agrees with the result of N_2 adsorption isotherm and simulations. As anticipated, the 2D MOFs exhibited anisotropic electrical transport capability, with the in-plane conductivity of the whole crystallite significantly greater than that of the out-of-plane conductivity. An alternative bottom-up technique, based on anisotropic nature of horizontal and vertical directions, has been developed to promote a preorientation of the ligand on the surface.[190] HRTEM observations clearly demonstrated a large crystalline domain of 600 nm with a distinct lattice distance of 1.75 nm and a π–π stacking distance of 0.33 nm. The 2D film exhibited three orders of magnitude greater conductivity horizontally than vertically. More recently, unit-cell-thick MOF films, ranging from sub-monolayers of 2 nm to several layers, were synthesized on substrates by controlling growth time and precursor concentration.[191] HRTEM images revealed alternating chains of 4-membered and 6-membered rings along the [001] direction, which features the films with an outstanding gas sieve performance, with a separation factor of 115 in H_2/N_2 separation. The same approach can also be applied to fabricate 2D COF nanosheets. Peng *et al.*[43] devised a sheet-shaped COF composed of a flexible building block to decrease the strong π–π interaction. At a total dose of 20 e $Å^{-2}$, the hexagonal structure of the TPA-COF nanosheets can be explored along the [001] direction at a resolution of 4 Å. For the first time, the individual building blocks were detected through HRTEM images. To prevent pore blockage caused by traditional functionalization of the center or side chain, it was proposed to incorporate a functional group into the linkage to provide COFs with more reactivity without sacrificing crystallinity. Li *et al.*[192] introduced high activity imidazopyridinium analogues as the linker, which permits simple exfoliation along (110) to generate 2D IP-COF nanosheets for the ionicity. A slight deviation from the stacking direction and a fringe distance of 2.5 nm corresponding to (110) facets were clearly revealed, which agreed well with simulation results set with similar deviation. A unique strategy to incorporate mechanically interlocked molecular architectures into monomers allows the molecules to

Open Access Article. Published on 21 March 2024. Downloaded on 1/15/2026 6:48:41 PM.
This article is licensed under a Creative Commons Attribution-NonCommercial 3.0 Unported Licence.

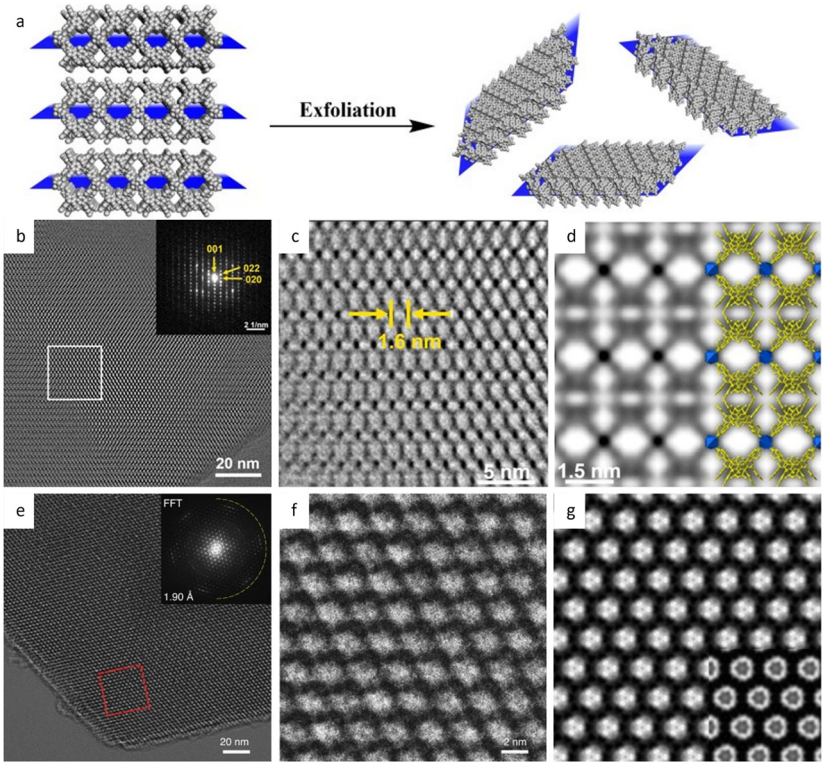

Fig. 14 Synthesis and low-dose HRTEM characterization of 2D nanosheets. (a) Schematic illustration of the 2D nanosheet synthesis by the exfoliation method. (b) Motion-corrected image, (c) CTF-corrected and denoised image, and (d) simulated potential map of 1-MONs. Reproduced with permission.[186] Copyright 2021, American Chemical Society. (e) Cryo-EM image, (f) enlarged image, and (g) averaged image of the Cu_3HHTT_2 MOF. Reproduced with permission.[189] Copyright 2020, Springer Nature.

mechanically link with a certain number of COF layers, thus providing pseudo-periodicity along the stacking direction.[193] A sandwich structure with macrocycles between COF layers reduces interlayer contact and enables self-exfoliation through electrostatic force, even with minor mechanical agitation that could potentially cause charge imbalance. HRTEM images showed a clear lattice fringe distance of 5.9 Å, corresponding to the (410) lattice plane.

Liu *et al.*[194] reported a surfactant-assisted interfacial strategy to synthesize layered 2D polymers with tunable crystal domains by using surfactants (Fig. 15a). It resulted in a significant enhancement in crystallinity domains from 0.3 μm^2 to 121 μm^2. HRTEM images in Fig. 15c and d revealed distinct domain boundaries along the (100) and (010) crystallographic planes, as well as tilt and overlapping boundaries. Furthermore, they expanded the on-water surface synthesis approach to construct 2D COFs by the irreversible Katritzky reaction to enhance diversity and stability.[195] With a controllable thickness of 2–30 nm, the size of crystalline domains could be enlarged from tens of nanometers to 120 μm^2. HRTEM images in Fig. 15b at a dose of 70 e $Å^{-2}$ revealed a square unit cell with AA stacking, consistent with the predications of modeling simulations. The layered 2D COFs synthesized *via* the surfactant-assisted interfacial strategy provided an ideal platform for analyzing defects in the pristine framework. The HRTEM Images at a dose of 100 e $Å^{-2}$ revealed a "micro-flowers" structure composed of grains with distinguishable sizes and orientations.[196] A thorough examination of the defects in Fig. 15e–g revealed that antiphase boundaries arise from the oriented attachment of crystalline particles, and can be eliminated through a self-correcting process. Grain boundaries with a tilt angle $<10^\circ$ produce a dislocation array, while maintaining the covalent connection between adjacent grains. Grain boundaries with high tilt angles, on the other hand, result in the termination of building blocks due to geometric prohibition of the covalent bond. Furthermore, rupture occurs along the boundaries under a micromanipulator force, indicating that these defects dominate the mechanical strength of 2D COFs. Recently, these 2D COFs were employed to optimize acceleration voltage.[197] Increasing the acceleration voltage, according to classical theory, can reduce radiolysis by decreasing the inelastic scattering cross section. However, this may result in a lower ratio between elastic and inelastic scattering cross sections, indicating a reduction in the elastic scattering cross section, particularly for thin nanosheets exposed to an excess dose. To evaluate the influence of critical fluence and efficiency of electron consumption on resolution, researchers defined an 'information coefficient'. Simulation results demonstrated a substantial improvement in image contrast, ranging from 41% to 113%, when employing an accelerated voltage of 120 kV. Experimental findings in Fig. 15h–m at 120 kV validated the simulations, showing reduced contrast delocalization and a maximum resolution of 1.9 Å. Interestingly, these results

 This journal is © The Royal Society of Chemistry 2024

Open Access Article. Published on 21 March 2024. Downloaded on 1/15/2026 6:48:41 PM.
This article is licensed under a Creative Commons Attribution-NonCommercial 3.0 Unported Licence.

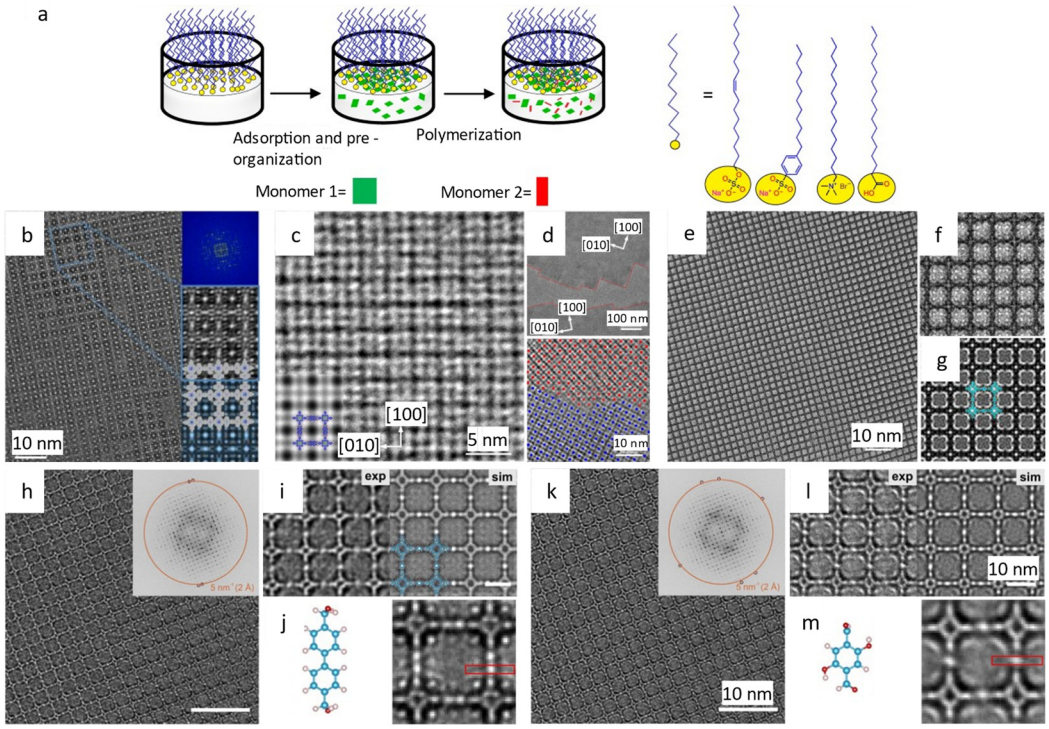

Fig. 15 Synthesis and low-dose HRTEM characterization of 2D COFs. (a) Schematic illustration of the synthesis of 2D COFs by interfacial reaction. Reproduced with permission.[194] Copyright 2019, Springer Nature. (b) Wiener-denoised image of C2DP-Por. Inset: Fourier transform, magnified image, and simulated image (from top to bottom). Reproduced with permission.[195] Copyright 2021, Springer Nature. (c) Image of 2DPI. Inset: Simulated image and structural model. (d) Image of two crystalline domains with marked edges (top), and image of a tilt grain boundary with marked core position. Reproduced with permission.[194] Copyright 2019, Springer Nature. (e) Raw image, (f) magnified image, and (g) simulated image of L-2D-PI. Reproduced with permission.[196] Copyright 2020, American Association for the Advancement of Science. (h) Raw image, (i) magnified image, simulated image, and (j) structural model of linkers and real-space averaged image of 2D-PI-BPDA. (k) Raw image, (l) magnified image, simulated image, and (m) structural model of linkers and real-space averaged image of 2D-PI-BPDA. Reproduced with permission.[197] Copyright 2022, Springer Nature.

surpassed those obtained at 300 kV, despite occasional aberrant contrast caused by elusive sample structural characteristics.

Like the extensively studied liquid–gas interface, the solid–liquid interface also exhibits great potential as a suitable platform. Cao *et al.*[200] synthesized a crystalline 2D COF membrane through condensing monomers at the interface of a SiO_2/Si substrate and precursor solutions. HRTEM images acquired perpendicular to the membrane exhibit highly ordered hexagonal channels with a size of 3.2 nm, indicating the preferred stacking direction of the COF layers. Nanofluidic devices fabricated using these 2D COF membranes exhibited 2–3 orders of magnitude larger ion currents compared to traditional single-channel devices, owing to the massive and ordered channels with charge and electrolyte concentrations of 0.01 M.

Feriante *et al.*[201] employed HRTEM to examine COFs after a reaction time of one minute. The results revealed that COFs were highly crystalline sheets with a thickness ranging from 3 to 30 nm, consistent with the XRD findings. These results indicated that the self-correction of amorphous polymers into an ordered framework may not be a universal way of synthesizing COFs. Instead, it is possible that imine-linked COFs may initially generate ordered sheets with limited registry, which then structurally reorient and stack to construct a COF with three-dimensional order.

4.1.3 Host–guest structure elucidation. MOFs and COFs have also attracted significant attention as host materials to incorporate small molecules or nanoparticles owing to their porous nature. To achieve a controllable synthesis of composites with specific functions, it is crucial to investigate the interaction between the host framework and the guest molecule. Aulakh *et al.*[202] employed a simple solvent-mediated approach to insert single-molecule magnets $Mn_{12}Ac$ into the pore of NU-1000 with retained magnetic bistability. HRTEM images along the [001] direction revealed that the distinct nanoparticles precisely lodged in the primary ordered hexagonal channels of NU-1000, providing the first real-space depiction of guest molecules in MOF pores. The as-designed composite demonstrated record molar single-molecule magnet loading capabilities with increased thermal stability, while preserving the magnetic bistability in entirety. Dou *et al.*[189] demonstrated that the presence of guest molecules with $[CoO_6]$ secondary building units (SBUs) in the channels of 2D M_3HHTT_2 nanosheets might disrupt the original π-stacking and lead to sliding of the nanosheets into a staggered ABC packing pattern. The $Co_3(HHTT)(H_2O)_{12}$ clusters that resided in the hexagonal channels interacted with adjacent MOF layers, resulting in discernible contrast with the lattices.

The host–guest interaction may also lead to an intriguing degree of polymorphism in switchable DUT-8 (Ni), which can

Open Access Article. Published on 21 March 2024. Downloaded on 1/15/2026 6:48:41 PM.
This article is licensed under a Creative Commons Attribution-NonCommercial 3.0 Unported Licence.

adopt a degenerate family of disorganized configurations.[203] The complicated disordered structure arises from six potential up/down interactions between the step-like linker and paddle wheel clusters, which are necessary to meet the boundary requirement. The diffraction patterns suggest the widespread occurrence of stacking faults in the framework and the coexistence of numerous domains inside an individual nanocrystal. It is feasible to switch between well-defined disordered configurations by regularly switching guests to promote the reorientation of the framework, suggesting that it is conceivable to record complicated information pertaining to their physical characteristics by manipulating disordered configurations.

4.1.4 Interfacial structure elucidation. Besides the intrinsic structure and resident guest molecules, the surface structure of MOFs and COFs plays a significant role in determining a variety of physicochemical characteristics. However, this was a challenging task before the development of low dose TEM techniques. Zhu and colleagues[25] carried out a pioneering investigation to identify the terminal group on the surface of ZIF-8 at an extraordinarily low accumulative dose of 4.1 e $Å^{-2}$. HRTEM images from the ⟨111⟩ direction revealed that the (110) surface terminated without reconstruction or macro-defects. This indicated that the termination was in the armchair model with a lower surface energy. The terminated mode was further validated to be armchair-type termination on interconnecting (110) surfaces between two ZIF-8 crystals, which revealed a flawless transitional interface with precisely aligned (112) lattice fringes (Fig. 16d–f). Further verification was carried out to identify the discrepancy along three mean directions.[204] A zigzag surface structure with tetrahedrally coordinated Zn sites was revealed, which was also confirmed by experimental and simulated results from the other two directions. In this structure, there are two Zn^{2+} with 3/4 linkers on the zigzag surface, whereas there are two Zn^{2+} with 1/2 linkers on the armchair and armchair-flat surfaces. Meanwhile, the surface structure can be modified by adjusting the solvent and metal/ligand ratio. Similar analysis on the surface of UiO-66 revealed that the truncation surface corresponded to (100) and (111) facets.[41] Two termination modes with the (111)

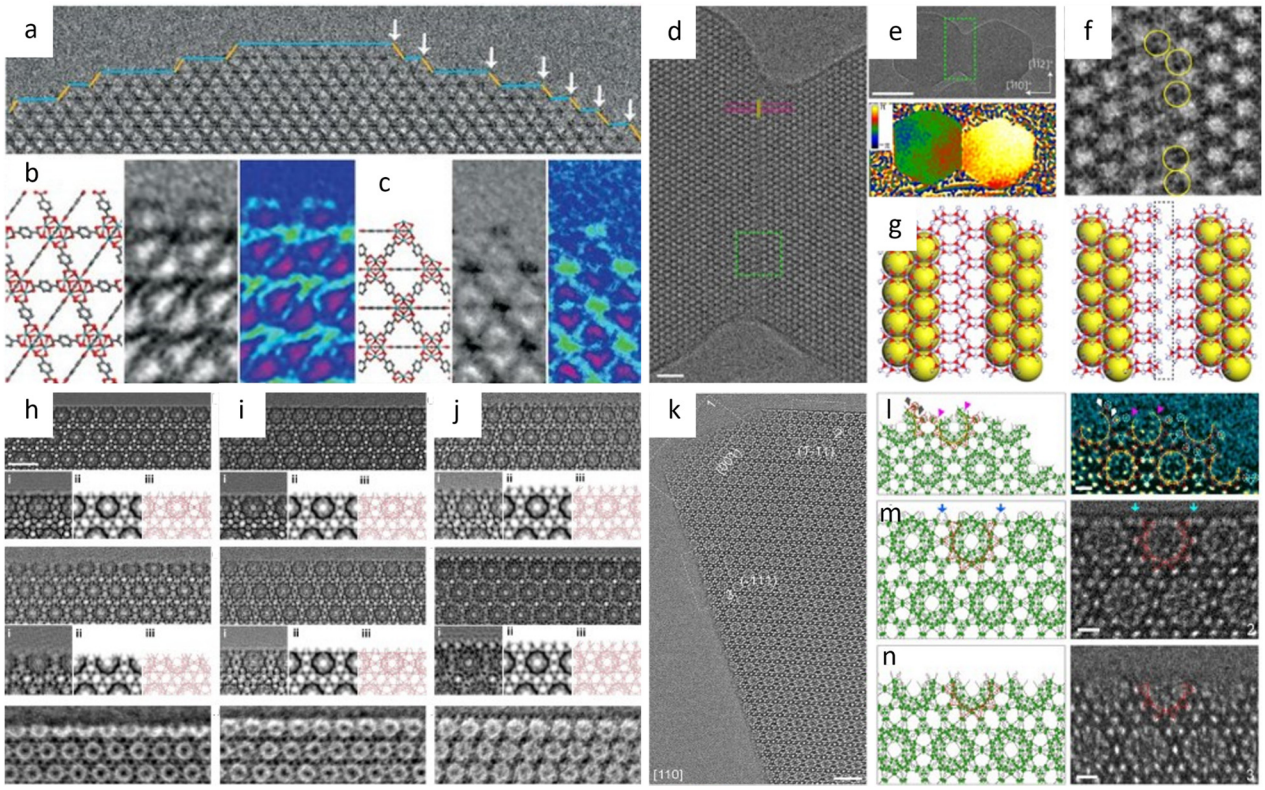

Fig. 16 Low-dose image of the surface and interface of MOFs. (a) The terminal steps of UiO-66 including the {100} (blue) and {111} facet (yellow). (b) Structural model, real-space averaged image, and colored image (from left to right) of the ligand-terminated {111} surface. (c) Structural model, real-space averaged image, and colored image (from left to right) of the ligand-free {100}/{111} surface. Reproduced with permission.[41] Copyright 2018, The American Association for the Advancement of Science. (d) Enlarged image of the green region in (e). (e) Low-magnification image of the interface (top) and the corresponding geometric phase map in temperature colour codes (bottom) of two ZIF-8 crystals. (f) CTF-corrected image of the green area in (d). (g) Bulk (left) and optimized interfacial structures (right) projected along the [111] direction. Reproduced with permission.[25] Copyright 2017, Springer Nature. (h)–(j) CTF-corrected image of fresh MIL-101-HF, MIL-101-NA, and MIL-101-Ac (TOP). CTF-corrected image of vacuum-heated MIL-101-HF, MIL-101-NA, and MIL-101-Ac (middle), and iDPC-STEM image of vacuum-heated MIL-101-HF, MIL-101-NA, and MIL-101-Ac (bottom). (i) Real-space averaged image, (ii) simulated projected potential map, and (iii) structural model. Reproduced with permission.[198] Copyright 2019, American Chemical Society. (k) Drift-corrected image of MIL-101 along the [110] direction. (l) Structural model (left) and colored Gaussian-filtered image (right). (m) and (n) Structural model (left) and unfiltered image (right) of the terminal surface structure of MIL-101 with different completeness. Reproduced with permission.[199] Copyright 2020, Wiley-VCH GmbH.

 This journal is © The Royal Society of Chemistry 2024

Open Access Article. Published on 21 March 2024. Downloaded on 1/15/2026 6:48:41 PM.
This article is licensed under a Creative Commons Attribution-NonCommercial 3.0 Unported Licence.

facets terminating with an organic linker and exposing Zr clusters at the connected sites between (100) and (111) facets coexisted (Fig. 16a–c).

The analysis is expanded to another well-studied MOF, MIL-101 (Cr), to determine the effect of additives on the crystallization process, which can improve the crystal size management and/or increase product output.[198] Completeness, defined as the proportion of residual hybrid super-tetrahedra in the incomplete medium cage, was used to evaluate the impact of different additives. HRTEM images in Fig. 16h–j obtained at 8 e $Å^{-2}$ revealed uniform {111} surfaces terminated by almost medium cages with varying degrees of completeness. MIL-101 synthesized with no additives or with HF exhibited the same open surface completeness of 80%, while the samples from acetic acid showed 100% completeness. This is the first time that the impact of additives on the surface structure has been measured. Han *et al.*[199] also observed a similar phenomenon involving incomplete cages at the surface, specifically the loss of one or two $Cr_3(\mu_3\text{-O})$ at the smooth terminal $(1\bar{1}1)$ surface (Fig. 16k–n). The $(\bar{1}11)$ facets exhibited an unusually uneven surface, which may be the consequence of a distinct loss model for the three trimers at the sublayer surface. The transition from a sublayer surface to a stable top surface suggested a possible crystal growth mechanism, which involved the progressive formation of full super-tetrahedra through the attachment of $Cr_3(\mu_3\text{-O})$ trimers.

Low-dose TEM has emerged as the predominant method for atomic imaging of COMs. Nonetheless, the application of TEM encounters certain limitations. For example, the CTF in TEM images varies dramatically with defocus, necessitating precise defocus measurement for reliable image interpretation. Second, the implementation of spectroscopic techniques such as EELS and EDS to obtain atom-specific information, including species identification and valence states, is more intricate in the TEM model. Consequently, there is a growing exploration of STEM as an alternative approach to achieve interpretable images with higher resolution, as well as for spectroscopic analyses.

4.2 STEM

4.2.1 Bulk structure elucidation. STEM has been widely used to reveal atomic structures due to its nearly directly interpretable images without the anomalies induced by non-optimal defocus in HRTEM. However, difficulties arise when it is applied to beam-sensitive materials, as the converged beam typically introduces a greater electron dose and destructive damage.[205] The utilization of low-dose STEM for atomic-level imaging has been pursued by researchers; however, the achievement of satisfactory results was limited before the advent of the iDPC-STEM method. For example, Mayoral *et al.*[206] conducted the analysis of zeolite TAPO-5 by HAADF-STEM at an electron dose rate of 0.038 e $Å^{-2}$ s^{-1} with an exposure time of 10 μs per pixel, and Zn-MOF-74 at a dose rate of 0.20 e $Å^{-2}$ s^{-1}. Hexagonal channels with distinguishable Zn clusters can be revealed from these images. However, even with the highest resolution available at the time, it was insufficient to identify each column due to the low SNR. Thiam *et al.*[207] functionalized the MOF Zr-NU-1000 with a surface organometallic fragment for the predictive heterogeneous catalysis. HAADF-STEM investigations revealed the original structure with hexagonal and trigonal channels, and the specifically anchored W species in Zr_6 sites. However, it is impossible to distinguish W from Zr_6 clusters or even image individual Zr atom at 0.32 nm with a resolution of 0.7 nm. For thin 2D MOF nanosheets, HAADF-STEM images also can reveal the local structure of the interface with distinct missing cluster defects and disordered regions.[208] Research on MIL-101 by ADF-STEM imaging under a low-dose condition revealed a super-tetrahedral structure that corresponded well with the simulated results.[209] However, it still suffers degradation after image acquisition. In addition, the atomic structure of the mixed-matrix MOF membrane by low dose ABF-STEM imaging revealed the preferential orientation of (001) with a distinguishable distance of adjacent inorganic chains and confirmed the highly desirable morphology for attaining in-plane alignment.[210]

The iDPC-STEM method (Fig. 17a) has become a prevalent strategy for characterizing beam-sensitive materials, such as perovskites,[211] zeolites,[54] and MOFs/COFs, owing to its high electron utilization efficiency and high SNR. Shen *et al.*[212] applied the iDPC-STEM imaging technique to reveal the atomic structure of MIL-101 and applied it to beam-sensitive materials including MOF UiO-66 and zeolites ZSM-5 and SAPO-34. The traditional ADF-STEM imaging method can only demonstrate the ordered spheres and lattices of MIL-101, but it is unable to differentiate between node–linker coordination. Intriguingly, the averaged iDPC-STEM images in Fig. 17b–d at a beam current of less than 0.1 pA can reveal the node–linker coordination, which consists of three 1,4-benzene dicarboxylate linkers in each coordination with high contrast. Additionally, the spatial resolution of 4.7 Å provided sufficient details, although the determination of individual atoms remains challenging.[27] The iDPC-STEM method was also used to investigate the microstructure of BZIF-8 composites, which exhibit unexpected activity when the pore size of BZIF-8 is smaller than the enzymatic substrate.[40] The iDPC-STEM images in Fig. 18i and j of BZIF-8-S revealed that the 12 Å periodic cavity with pore sizes of 3.4 and 2.8 Å is formed by Zn clusters and 2-methylimidazole, respectively. In contrast, BZIF-8-B exhibited co-existence of crystalline and amorphous phases with feeble diffraction intensity. Furthermore, the disordered structure exhibited numerous coordination defects, which accounted for the high enzyme activity. Additionally, an intriguing phase transformation from an initial SOD-type to a ***dia***-type nanosheet was discovered in BZIF-8-B, whereas this transformation was absent in BZIF-8-S.

STEM images for UiO-66 indicated that the structure of the two sides of the interface exhibited significant difference.[145] The core area showed three Zr clusters, while the shell region showed six. Additionally, huge clusters were hexagonally organized with a *P6mm* projection. The data could then be used to reconstruct a 3D potential map, which revealed the connection of the Zr_{12} cluster with 12 other clusters. As a comparison,

Open Access Article. Published on 21 March 2024. Downloaded on 1/15/2026 6:48:41 PM.
This article is licensed under a Creative Commons Attribution-NonCommercial 3.0 Unported Licence.

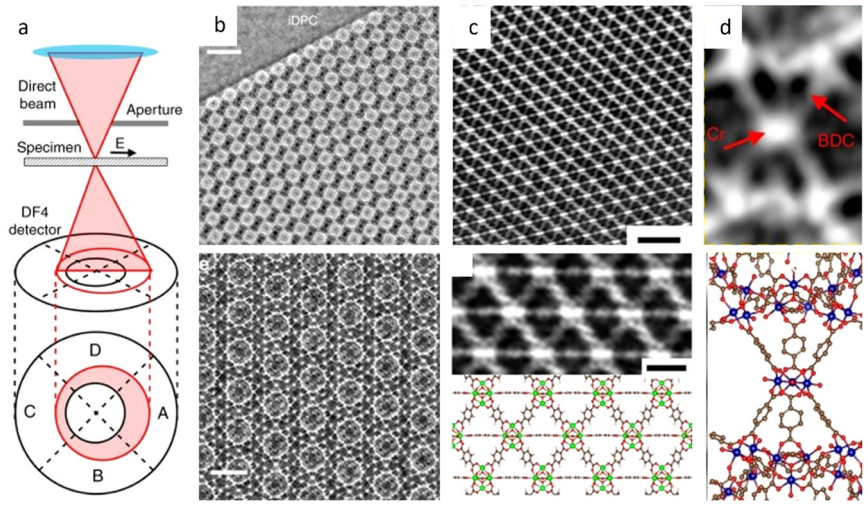

Fig. 17 The schematic illustration and imaging of iDPC-STEM. (a) The workflow of iDPC-STEM: four images detected by the segments of the DPC detector can be calculated to DPC*x* and DPC*y*, which can be further integrated into the iDPC-STEM image. (b) iDPC-STEM image integrated from the DPC image (top, scale bar: 10 nm), and magnified image (bottom, scale bar: 5 nm). (c) Image of UiO-66 along the [100] direction (top), and magnified image with the structural model (bottom). Scale bar: 3 nm. (d) Imaging of super tetrahedra in MIL-101 constructed by Cr and the organic linker (top) and the structural model (bottom). Reproduced with permission.[212] Copyright 2020, Springer Nature.

HAADF-STEM images showed an arrangement of indistinct ZrO nodes without linkers, DPC-STEM images showed linkers vaguely present with obvious noise, and iDPC-STEM images showed clear Zr–O nodes and linkers (Fig. 18a–d).[44]

Feng *et al.*[213] synthesized bimetallic (Zn,Zr)-UiO-66 with easily removable Zn nodes to construct a crystal with cluster defects. The iDPC-STEM images along the (100) direction revealed an obvious absence of clusters, resulting in a topology

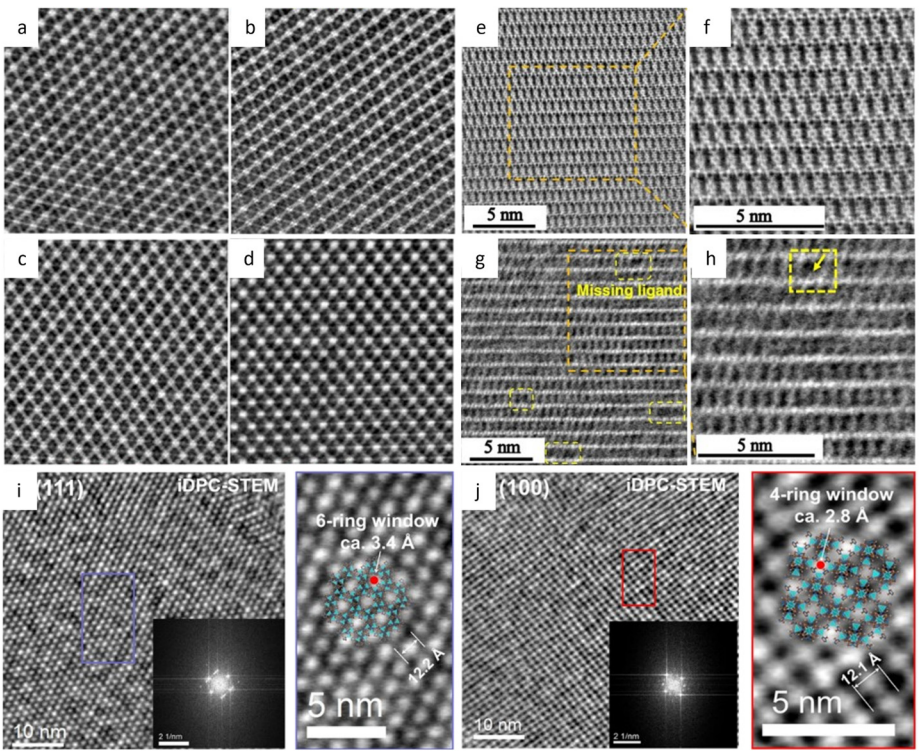

Fig. 18 The iDPC-STEM characterization of MOFs. (a)–(d) Image of UiO-66 (Zr) along the [110] direction with different dwell time: 8, 16, 32, and 64 μs, respectively. Reproduced with permission.[44] Copyright 2023, American Chemical Society. (e) High-magnification image and (f) magnified image of Ni-BDC-T. (g) High-magnification image and (h) magnified image of FeNi-BA-T with missing ligand defect. Reproduced with permission.[214] Copyright 2022, Wiley-VCH GmbH. (i, j) Image of BZIF-8-S along (i) the [111] direction and (j) the [100] direction. Reproduced with permission.[40] Copyright 2022, Springer Nature.

 This journal is © The Royal Society of Chemistry 2024

Open Access Article. Published on 21 March 2024. Downloaded on 1/15/2026 6:48:41 PM.
This article is licensed under a Creative Commons Attribution-NonCommercial 3.0 Unported Licence.

switch from ***fcu*** to ***reo*** net. UiO-66 with four defects/clusters demonstrated a considerable increase in styrene oxide conversion from 17% to 90%, and a twofold improvement in CO_2/N_2 selectivity. Sun and colleagues[214] incorporated Fe^{3+} into the skeleton of Ni-MOF to create multivariate MOFs with varying lattice strain for enhancing the electrocatalytic ability. STEM images in Fig. 18e–h showed numerous missing ligand defects in the thermally treated sample FeNi-BA-T, whereas the original Ni-MOFs exhibited no evident defects. FeNi-BA-T exhibited superior oxygen evolution reaction activity compared to that of commercial RuO_2, due to the unsaturated metal atoms at the defects and the reduced lattice strain variation. To investigate the effects of functionalization on the dynamic properties, Liu *et al.*[215] analysed the rotation properties of BDC linkers to establish a correlation between linker structure and local rigidity. Notably, the intensity profile along the long axis revealed an intriguing trend in the width of the projection of BDC-X linkers, wherein the signal of BDC-NH_2 transformed from a narrow line with a full width at half maximum of 2.01 Å to a broader spot measured as 4.02 Å in BDC-Br. This broadening phenomenon indicated the π-flipping of benzene rings induced by different functional groups, supporting the trend of –OH > $–NH_2$ > –H > $–CH_3$ ∼ –F > –Cl > –Br. Subsequently, the most rigid UiO-66-OH exhibited the highest CO_2 adsorption capacity, confirming the advantageous effect of rigidity on the adsorption of guest molecules.

Zhang *et al.*[216] incorporated tetra-topic chromophores into the skeleton of COFs to enhance two-photon absorption performance. The iDPC-STEM images revealed an offset distance between layers of 0.4 nm, consistent with the value of 1/8 *a* offset along the *a* axis. The micrometer-sized COF-606 single crystals with serrated interlayer stacking exhibited the highest two-photon action cross-section value. Liu *et al.*[217] synthesized topological isomers JUC-620 with a ***dia*** net and JUC-621 with a ***qtz*** net by calculating the potential energy. The iDPC-STEM images along the [100] direction of JUC-621 revealed the symmetry type of *p*2*mm* that matched well with the simulated projective potential. The space group symmetry was further determined as $P6_422$. Combined with cryo-FIB, iDPC-STEM images facilitated the observation of core–shell structures in MOF-COF with a sharp boundary.[146] The application of this combined approach allowed for the precise characterization of the interpenetrated structure of MOF-5 and the half hexagonal-shaped channel at the interface.

4.2.2 Host–guest structure elucidation. Jiang *et al.*[218] presented front-page research on host–guest interaction by growing TiO_2 within the mesopores of MIL-101 and its derivatives to create molecular compartments. The STEM images in Fig. 19 revealed nearly complete occupation of TiO_2 in the mesopores of 29 Å and 34 Å in 42%-TiO_2-in-MIL-101-Cr. These TiO_2 exhibited an exact arrangement in the same type of pore, concentrating in the center of the small pore and covering the walls of the large pore. In contrast to the situation in 23%-TiO_2-in-MIL-101-Cr, nearly all occupation occurs in the mesopore of 29 Å only, suggesting the preferred occupation mode of the guest molecule. The turnover frequency (parameter to evaluate the catalytic capacity) of the TiO_2 units in the 34 Å pore is 44 times higher than that in the 29 Å pore, indicating the importance of the location of the guest. As a result, the overall performance of 42%-TiO_2-in-MIL-101-Cr-NO_2 is 1.4×10^4 higher than that of pure TiO_2. Liu and colleagues[219] were the first to report simultaneously imaging MOFs and single metal atoms to gain a comprehensive understanding for the design of single atom catalysts. Encapsulated single Pt atoms adsorbed by benzene *via* Pt–π interactions in UiO-66 led to an increase in intensity in the center of adjacent Zr clusters and a reduction in organic linkers. However, Pt only exists as clusters rather than single atoms in UiO-66-NH_2. The adsorbed position was determined by depositing single Pd atoms, which exhibited a tendency to be close to the amino group, highlighting the requirement for a thorough evaluation of functional group species and binding strength.

4.2.3 Interfacial structure elucidation. Similar to the elucidation provided by HRTEM images,[198] investigation on the surface of MIL-101 by iDPC-STEM has revealed two terminations, including complete and near half cages, with complete cages being more prevalent for the energetic stability.[212] The corner structure terminated with exposed 34 Å cages, whereas the adjacent margins terminated with 29 Å cages, and the growth and propagation of surface steps were easily identifiable in Fig. 19h-i. The interface analysis revealed no lattice incompatibility at the affixed (111) face, which is connected by super-tetrahedra while one lattice undergoes horizontal rotation and movement. Interestingly, the surface structure experienced different movements under the electron stimulation (Fig. 20a and b).[27]

The interface analysis of two identically oriented UiO-66 crystals revealed a continuous lattice at the transition region with an irregular terminal mode (Fig. 20c–g). In contrast, the interface analysis of two crystals with different orientations revealed chemical bonding between metal nodes and organic linkers with a distortion of the node.[220] The coordination formed through periodically arranged organic linkers suspended outside of the metal was confirmed by the intensity profile analysis.

The iDPC-STEM method has achieved notable success in the high SNR visualization of heavy and light atoms within the COM structure. However, this method necessitates precise zone axis alignment and specific defocus settings to obtain clear and interpretable images, resulting in a relatively low success rate. Consequently, in addition to the combination with auto-alignment techniques, emerging technologies such as ptychography by 4D-STEM have been employed to address the challenges associated with imaging beam-sensitive materials.

5. Upcoming approaches and techniques

Over the past few decades, low-dose TEM/STEM have progressively become routine imaging techniques for elucidating the local structure, host–guest interaction, and surface of extremely sensitive COMs. These techniques advance the comprehension

Open Access Article. Published on 21 March 2024. Downloaded on 1/15/2026 6:48:41 PM.
This article is licensed under a Creative Commons Attribution-NonCommercial 3.0 Unported Licence.

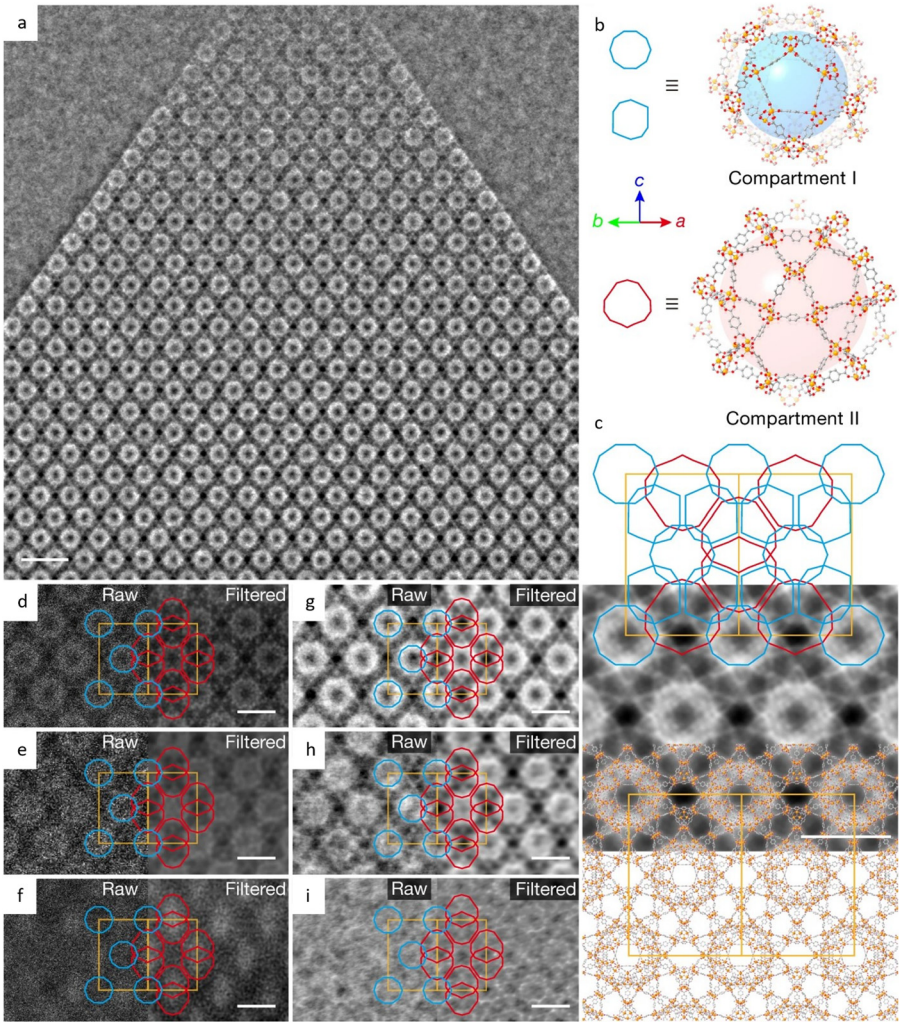

Fig. 19 The observation of the guest molecule in MOFs by the iDPC-STEM image. (a) Image of MIL-101-Cr along the [110] direction. Scale bar: 10 nm. (b) Two structural models (compartments I and II) with specific position of guest TiO_2. (c) Symmetry-imposed image overlaid with the pore distribution map (top) and the structural model (bottom). (d)–(f) Raw and filtered HAADF image, and (g)–(i) raw and filtered iDPC-STEM image overlaid with the pore distribution map. Scale bar: 5 nm. Reproduced with permission.[218] Copyright 2020, Springer Nature.

of the structure–property relationship to guide the design of specific materials with prospective functions. However, HRTEM imaging is constrained by CTF and requires a precisely determined defocus value, HAADF-STEM imaging is insensitive to light atoms in organic linkages, and iDPC-STEM imaging requires precise focusing. Further development is required for optimisation of image acquisition conditions to minimize excess dose consumption, and post-processing to eradicate noise or extract structural information for an ideal SNR. The novel imaging mode, known as 4D-STEM, holds great promise as a highly effective technique for low-dose imaging. By capturing massive information from both real and reciprocal space and leveraging redundancy in the data, 4D-STEM enables the recovery of high-quality images. Pioneering work conducted by Peng *et al.*[208] utilizing the ptychography algorithm demonstrated the successful recovery of the MOF structure using 4D-STEM. However, additional tuning and careful selection of the ptychography algorithm are necessary to achieve an ideal reconstruction at minimal dose. These developments may also shed light on the incorporation of *in situ* technology, a potent method for performing real-time intuitive imaging under different stimuli, which enables direct imaging of the dynamic process of catalysis and reveals the dynamic interactions of reactant molecules with the active site, even for the beam-sensitive materials. 4D-STEM and *in situ* techniques have revolutionized the acquisition of extensive spatiotemporal data, offering unprecedented insights into material behavior. The advancements in these techniques owe much to the progress in computer science, which has facilitated the processing and analysis of the vast amount of data generated. In recent years, machine learning (ML), an advanced and innovative technology, has witnessed remarkable progress in its application to electron microscopy, specifically in the domains of imaging and spectroscopy.[221] Despite the significant advancements achieved thus far, the full potential of ML in TEM and STEM is yet to be fully realized. This can be attributed to the rapid

 This journal is © The Royal Society of Chemistry 2024

Open Access Article. Published on 21 March 2024. Downloaded on 1/15/2026 6:48:41 PM.
This article is licensed under a Creative Commons Attribution-NonCommercial 3.0 Unported Licence.

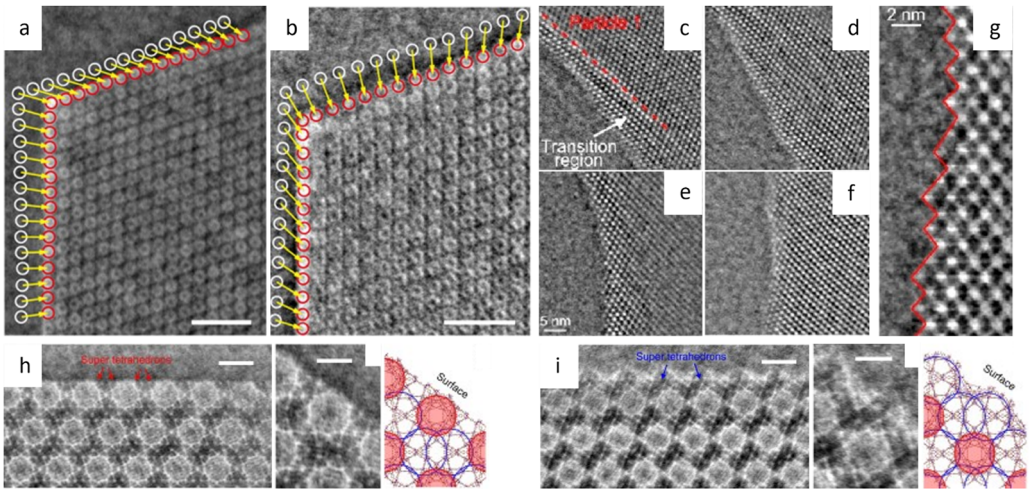

Fig. 20 The terminal surface structure observation by iDPC-STEM. (a, b) Image of the MIL-101 surface (a) before and (b) after electron irradiation. Reproduced with permission.[27] Copyright 2020, American Chemical Society. (c)–(f) Images with continuous transition area and (g) magnified image of the jagged surface of UiO-66 (Zr). Reproduced with permission.[220] Copyright 2020, American Chemical Society. (h) and (i) Two types of terminal surface image (left, scale bar: 5 nm), magnified image (middle, scale bar: 3 nm), and structural model (right) of MIL-101. Reproduced with permission.[212] Copyright 2020, Springer Nature.

evolution of ML algorithms, the wealth of data generated by direct electron detectors, and the inherent complexity of specimen structures.

5.1 Ptychography by 4D-STEM

The 4D-STEM dataset consists of a series of CBED patterns generated at each scan position. These patterns contain voluminous structure information that can be used for reconstruction by various algorithms, such as ADF and BF images using virtual detectors, center of mass images analogous to DPC and iDPC images, and ptychographic phase images. Among these algorithms, ptychography can generate interpretable phase images, allowing for simultaneous imaging of heavy and light atoms. Additionally, it permits scanning by defocused beams, which improves dose efficiency and data acquisition rate. Furthermore, it has a higher thickness tolerance due to the flexibility in adjusting the scanning region and sampling method. Therefore, ptychography has been applied to various materials, including 2D materials and biological samples.

Ptychographic phase images of mono-layered MoS_2 revealed much more distinguishable atoms than those in HAADF images acquired at a similar dose.[222] Atomic-resolution images with a resolution of 1.58 Å were also reconstructed at a dose of 403 e $Å^{-2}$. Jiang *et al.*[58] reconstructed a series of images of mono-layer MoS_2 at a range of doses from 250 to 2000 e $Å^{-2}$ using a distinct algorithm. The image quality clearly improved as the dose increased. The information limit of full-field ptychography images was 5α, corresponding to an Abbe diffraction-limited resolution of 0.39 Å, which is substantially lower than that of conventional ADF (0.98 Å). Using a mixed quantum state to describe the partial coherence, mixed-state ptychography[223] was proposed to reconstruct the images of bilayer $MoSe_2/WS_2$.[224] The lattice can be discerned even at a dose of 375 e $Å^{-2}$ in Fig. 21e–j. Zhou *et al.*[225] combined cryo-TEM with ptychography to analyse the biological rotavirus and non-symmetric immature particles at a low dose of 5.7 e $Å^{-2}$. The combination of these two techniques demonstrated high-quantity reconstruction with substantially enhanced contrast transfer and phase sensitivity, yielding high-quality data with wider and continuous CTF. The superiority of ptychography reconstruction was further demonstrated by the 3D phase reconstruction of organic DNA with inorganic Au particles,[226] and single particle analysis with a wide bandwidth for small molecules such as rotavirus double-layered viral particles.[227]

The high-quality reconstruction of biological specimens by ptychography offers the potential for elucidating beam-sensitive materials such as zeolites, despite the challenges posed by the need for atomic imaging and zone axis alignment. O'Leary *et al.*[228] proposed a strategy for reducing the exposure duration of the specimen by altering the bit depth of the detector. Using this method, the atomic structure of ZSM-5 can be revealed at a dose of 200 e $Å^{-2}$, despite the ambiguity of the thinner region due to insufficient scattering. Dong *et al.*[229] disclosed the local structure of Na^+ ion occupied zeolite LTA and guest-containing ZSM-5 using ptychography with the iterative ePIE at a dose of less than 3000 e $Å^{-2}$ (Fig. 21a–d). They also demonstrated that the iterative technique can achieve a higher resolution reconstruction than the non-iterative technique.

To overcome the time-consuming zone axis alignment process, Sha *et al.*[232] developed a method that makes the Fresnel propagator adaptive to eliminate the misalignment. They applied the proposed method to imaging ZSM-5 with a thickness of 60 nm at a dose of 1100 e $Å^{-2}$, which revealed deformation along the lateral and depth directions due to the structure's flexibility, as well as dose-dependent visibility of individual metal atoms in the pores (Fig. 21k).[230] In a recent study by Zhang *et al.*,[231] the potential of ptychography in reconstructing the projection direction was realized, enabling

Open Access Article. Published on 21 March 2024. Downloaded on 1/15/2026 6:48:41 PM.
This article is licensed under a Creative Commons Attribution-NonCommercial 3.0 Unported Licence.

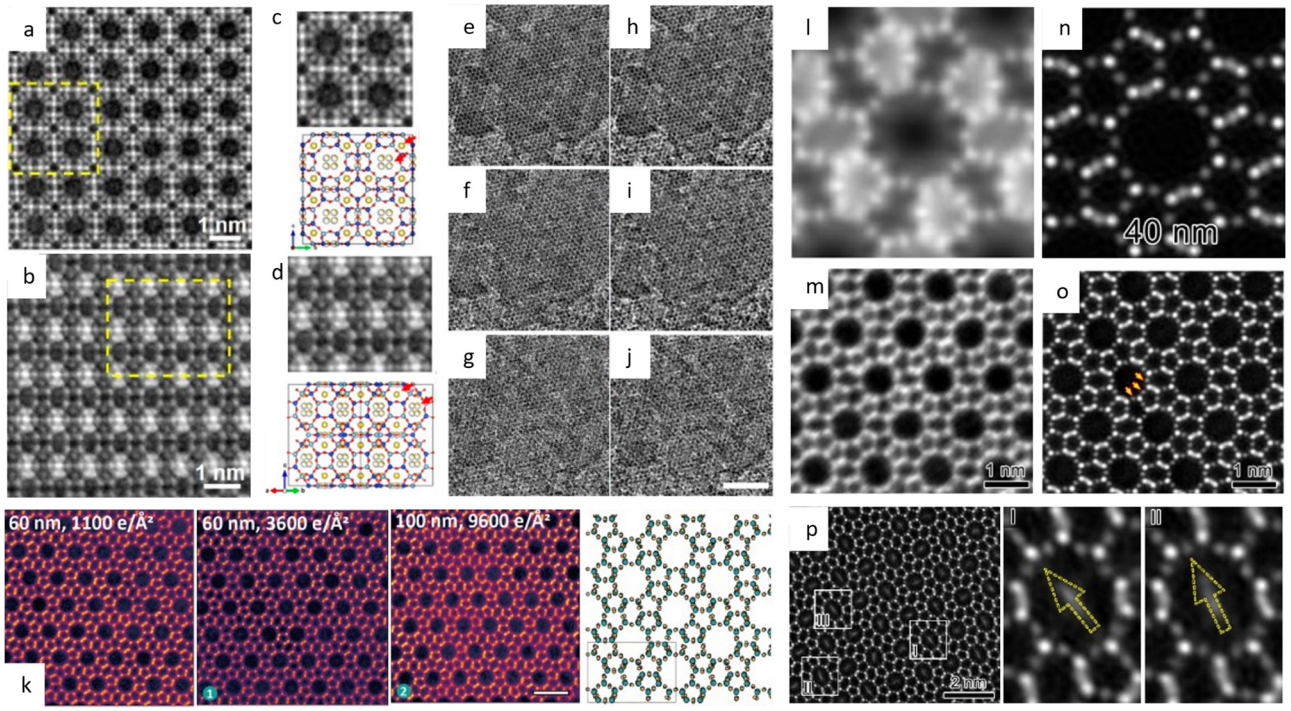

Fig. 21 Ptychograpghy reconstruction of zeolite and 2D materials based on the 4D-STEM dataset. (a) Reconstructed image, and (c) magnified image and structural model of the Na-LTA zeolite along the [100] direction. (b) Reconstructed image, and (d) magnified image and structural model of the Na-LTA zeolite along the [110] direction. Reproduced with permission.[229] Copyright 2023, American Chemical Society. (e)–(j) Mixed-state ptychography reconstruction of WS_2 at a total dose of 1500, 790, and 375 e $Å^{-2}$. (h)–(j) Single-state ptychography reconstruction of WS_2 at a total dose of 1500, 790, and 375 e $Å^{-2}$. Scale bar: 3 nm. Reproduced with permission.[224] Copyright 2020, Springer Nature. (k) Low-magnification image (scale bar: 100 nm) and (m) ptychography reconstructed images and structural model of ZSM-5. Scale bars: 5 nm. Reproduced with permission.[230] Copyright 2023, American Association for the Advancement of Science. (l) and (m) Simulated and experimental iDPC-STEM images, and (n) and (o) ptychography images of ZSM-5 of 40 nm. (p) Ptychograpghy images of ZSM-5 with adsorbed *p*-xylene molecules. Reproduced with permission.[231] Copyright 2023, The American Association for the Advancement of Science.

the identification of 3D inhomogeneities within the zeolite structure (Fig. 21l–p). Through the reconstruction of a ~40 nm-thick specimen, the presence of oxygen was unambiguously identified, which was previously achievable only in the case of iDPC-STEM when the sample thickness was below 12 nm. The reconstructed ptychographic image exhibited excellent contrast, facilitating the identification of adsorbed *p*-xylene molecules, and enabling direct observation of oxygen vacancies within the zeolite framework. Moreover, the depth-resolution was determined to be approximately 6.6 nm by analyzing the intensity profile using derivative curves along two atomic columns in seven slices. This approach demonstrated 3D imaging with a high dose-efficiency compared to other methods such as electron tomography and optical sectioning.

However, exceedingly sensitive MOF/COF materials are rarely explored. Simulation results of UiO-66 demonstrated that the reconstructed images matched the crystal structure nearly identically even though data were acquired with a large defocus value of 100 nm.[233] However, implementing it in practice remains difficult. Recently, Peng *et al.*[208] used ptychographic reconstruction to analyse the structure of an ultra-thin metal–organic layer in which individual Hf clusters were discernible at a transfer of information of 1/2.36 $Å^{-1}$. The images simultaneously displayed metal clusters with six organic linkers, corresponding well with the simulated images of four-layer metal–organic layers. Notably, the total dose for the acquisition of the dataset is 864 e $Å^{-1}$, significantly higher than most doses used in low-dose HRTEM/STEM. This indicates that additional investigation is required to determine the universality of 4D-STEM characterization in ultra-sensitive materials.

Ptychography has demonstrated the ability to image beam-sensitive biological specimens and zeolites at a comparatively low dose. However, the realistic dose for atomic-resolution reconstruction typically ranges from several hundreds to thousands, which is higher than that used for imaging exceedingly beam-sensitive materials such as MOFs and COFs. Therefore, the application of ptychography to these exceedingly delicate substances requires further investigation.

5.2 *In situ* techniques at atomic resolution

In situ TEM/STEM techniques, conducted under a single or multiple stimuli introduced into the specimen chamber, allow for the mimic of realistic scenarios. These techniques enable observation of the structural evolutions of materials in real time, facilitating a comprehensive understanding of the dynamic structure–property relationship. The development of *in situ* techniques has enabled the introduction of stimuli that encompass most application sectors for materials, including

 This journal is © The Royal Society of Chemistry 2024

Open Access Article. Published on 21 March 2024. Downloaded on 1/15/2026 6:48:41 PM. This article is licensed under a Creative Commons Attribution-NonCommercial 3.0 Unported Licence.

crystal growth, structure evolution, chemical catalysis, and electrocatalysis, among others. For example, the growth of Pt nanocrystals at the atomic level was monitored in liquid cells by TEM.[234] It revealed that the growth rate of all facets at small size suffers a block in (100) facets as the crystals grow up, leading to an understanding of the mechanisms of crystal growth and shape formation. Yuan *et al.*[235] visualized the dissociation and reaction of adsorbed water molecules through a twin-protrusion structure on the (001) surface of TiO_2 at 700 °C. Sun and co-workers[236] observed the formation and behaviour of mismatch dislocations during the transformation of Cu_2O/Cu at the interface when H_2 flow was introduced at 873 K. However, due to the complexity of the system and chamber design, *in situ* research at the atomic level on photo/electro-catalysis is typically not achieved.

In situ characterization requires a long-term observation and is conducted at the lowest possible dose rate (on the order of 100 e $Å^{-2}$ s^{-1}) to avoid beam-introduced error. However, this dose is still significantly higher than the critical threshold for beam-sensitive materials. Fortunately, the low-dose technique has been developed and applied to monitor crystal growth, structural transformation and catalysis of MOFs and COFs. Patterson *et al.*[237] reported a real-time observation of the growth of a ZIF-8 crystal at a dose rate of 15 e $Å^{-2}$ s^{-1} within 11 min. This observation revealed that the nucleation can be constrained by the local depletion of monomers, providing insights into the mechanisms underlying crystal growth. Additionally, this study represents the first observation of the growth of beam-sensitive materials, demonstrating the potential for *in situ* techniques. *In situ* techniques have been employed to visualize the growth of 1D MOF nanotubes[238] and colloidal COFs[239] at modest fluxes of 0.05 e $Å^{-2}$ s^{-1} and 0.66 e $Å^{-2}$ s^{-1} respectively. At an ultra-dose rate of 0.04 e $Å^{-2}$ s^{-1}, Parent and co-workers[240] observed pore breathing behavior in MIL-53(Cr) in response to water adsorption and temperature variations. *In situ* observation of a phase transition from NU-906 to NU-1008 at an accumulated dose of 6 e $Å^{-2}$ s^{-1} was also achieved by acquiring images every few minutes.[241] However, all of these *in situ* observations were conducted on a microscale rather than an atomic scale, highlighting the need for further advancements to extend low-dose atomic imaging from *ex situ* to *in situ*.

5.3 Machine learning

In recent years, machine learning has emerged as a powerful tool with applications spanning various scientific disciplines. Notably, in the context of electron microscopy, ML has demonstrated considerable potential in image denoising and phase retrieval discussed in Section 3. The utilization of supervised and unsupervised ML techniques has enabled efficient processing of data, leading to improved results in a time-effective manner. Furthermore, the advent of emerging techniques such as 4D-STEM and *in situ* technologies has resulted in the generation of massive datasets, necessitating advanced computer science methodologies for the extraction and analysis of relevant information. In this regard, ML offers new opportunities for achieving rapid and accurate results in the analysis of these complex datasets.

ML has been utilized in denoising using diverse strategies since the first application of neural networks in image denoising in 1989. Auto-encoding neural networks have shown the ability to reconstruct images with over 90% accuracy of column position after training with thousands of random sample images, along with improved contrast variation.[242] To realize a time-effective and fully informative recovery, convolutional neural networks (CNNs) advanced by graphical progressing unit (GPU) acceleration are being employed for assembling high-quality images without the blurring effect within an appropriate timescale.[243] Unlike the conventional convolution process, the divided pointwise and depthwise convolutions work more effectively, ensuring outstanding performance in suppressing noise. Practice using the sample datasets generated from multislice image simulation exhibited outstanding performance in presenting nonperiodic defects at ultra-low SNR. This demonstrated that the network can take advantage of both overall and localized information during the noise determination, and allows one to flexibly adjust the filtering strategy in the presence of atomic defects.[244] Additionally, a method to determine the consistency between the denoised images and original information was also proposed.[245] Another unsupervised method, *K*-means clustering, was applied to binarize the atom column and background for specifying the center of mass fitting zone.[246] The dominant Poisson noise can be eliminated through integration of Anscombe transform, block matching and 3D filtering, histogram stretching, and morphology filtering. The average error in the images is less than 0.7 pixel with an increased SNR to 7 to 11 dB, as well as an enhancement in the signals of light atoms.

The revolution in ptychography is accompanied with the development of pixel array detectors in 4D-STEM.[247] 4D-STEM generates multidimensional datasets including full information of the specimen, which is theoretically perfect for reconstruction. However, a comprehensive and efficient analysis remains challenging for the massive amount of data. It is difficult to explicate the nonlinear relationship between acquired signals and inherent properties in a linear way. Based on linear decomposition, the artifacts in raw diffraction patterns can be eliminated.[248] Furthermore, by evaluating the metaparameters, the amount of data can be reduced by up to 68-fold compared to the original data with a suitable cut-off. By combining variational autoencoders with rotational symmetry, a succinct presentation of 4D-STEM data with an atomic visualization of the symmetry-breaking map was achieved.[249] Even a single atom or vacancy in monolayer graphene can be identified, which might help to determine the abnormality even with a small atomic difference. Manifold learning, another nonlinear method in ML used to identify the underlying relation, has been utilized to approximate the nearest adjacent image in order to solve low-dimensional signals and iteratively reconstruct them.[250] This technique can extract multidimensional underlying information even from the weak diffraction pattern obtained from monolayer graphene, demonstrating the

Open Access Article. Published on 21 March 2024. Downloaded on 1/15/2026 6:48:41 PM. This article is licensed under a Creative Commons Attribution-NonCommercial 3.0 Unported Licence.

potential for low dose imaging and holonomic signal analysis. One such development is the work of Friedrich and colleagues,[251] who developed a network to retrieve a complex wave and recover images using CNNs based on the phase objective approximation and neighbouring diffraction patterns. This approach allows for rapid predictions in almost real-time, while the resulting images exhibit high SNR, high spatial resolution, and simultaneous imaging of both light and heavy atoms at comparable low electron dose.

In situ technology holds the potential to provide real-time observations of inner reaction mechanisms. However, the vast amount of data generated, ranging from tens to hundreds of images per minute, poses significant challenges for traditional processing methods. In this context, machine learning techniques based on mathematical models demonstrate great promise for the automatic processing of data with high efficiency and accuracy. Fully connected neural networks (FCN) based on an encoder–decoder architecture have proven effective in extracting features from *in situ* STEM datasets.[252] Through training, these networks can automatically capture high-resolution atomic relationships and structural information related to chemical bonding, such as the dynamic switching between different coordination states of silicon dopants in graphene over time. The weakly supervised FCN model trained on simulated STEM images enables quantitative analysis of each frame of high-dimensional *in situ* STEM data with minimal manual intervention, facilitating the self-adjustment of the microscope settings. Lee *et al.*[253] provide a practical guide for training deep learning models for the determination of vacancies and polymorph types, showcasing the accuracy of FCN models on a substantial number of experimental STEM images, which is comparable to meticulous manual analysis. On the other hand, the U-Net neural network, unlike FCN, incorporates skip connections to preserve context and details more effectively. Its smaller parameter count makes it particularly suitable for challenging datasets such as STEM images, where obtaining data annotations can be difficult. Yao *et al.*[254] pioneered the application of U-Net in the analysis of liquid-phase TEM images, revealing valuable information about reaction kinetics and assembly dynamics. The U-Net model showcased its capability in predicting the position and shape boundaries of nanoparticles amidst highly noisy and fluctuating backgrounds, thereby uncovering properties such as the anisotropic interaction landscape of nanoprisms. Lu *et al.*[255] successfully employed the U-Net architecture to identify all Pt–Ni nanoparticles in a case study involving bimetallic Pt–Ni catalyst nanoparticles, effectively segmenting them by well-defined outlines with much higher accuracy of edge detection. U-Net has demonstrated remarkable capabilities even in identifying seemingly unremarkable features, such as nanopores, in nanopore-healing images during investigating the healing behavior of magnetic 1T-$CrTe_2$.[256] Through the application of U-Net, the automatic identification of nanopores was achieved, showcasing the network's ability to accurately discern and analyze subtle details in the healing process.

The rapid development of ML has provided unprecedented capacity for electron microscopy, enabling the complex and time-consuming analysis process. This has vastly enhanced the analysis efficiency and accuracy. However, the success rate of ML under low-dose conditions endures an untenable decrease during the analysis due to the low SNR. This indicates that a further modification in ML is required for an accurate determination of beam-sensitive materials.

6. Summary and outlook

In recent decades, the development of MOFs and COFs, two crystalline porous frameworks, has led to widespread applications in various fields due to their high surface area, facilely tailored functionality, and designable pore structure. The MOFs/COFs' flexible organic linkages bestow them with diverse synthesis strategies, chemical structures, and topologies, making them ideal platforms for studying the structure–property relationship. However, the organic components of MOFs/COFs are sensitive to irradiation, making it difficult to determine the atomic structure using conventional TEM/STEM techniques. Recently, the low-dose technique has been swiftly developed for beam-sensitive materials, becoming a promising technique for imaging MOFs/COFs. These advancements rely on the integration of multiple technologies:

i. The development of DEDs enabled high-quality imaging with improved spatial resolution under low-dose conditions. Segmented detectors enabled integration of the fully recorded scattered electron with spatial distribution, which is the foundation for the newly developed iDPC-STEM to reconstruct phase images. The pixelated detector enables the recording of the entire spectrum of reciprocal space information, accelerating the acquisition of 4D-STEM datasets by recording CBED at each position for post-processing techniques such as ptychography. When specialized 'hollow' DEDs become available, the multimodal STEM mode, incorporating simultaneous imaging techniques (ptychography, HAADF-STEM, and DPC) along with spectroscopy (EDS and EELS), will facilitate comprehensive and reliable investigations into the structure and chemistry at ultrahigh spatial resolution.

ii. Low-dose zone-axis alignment enables automated tilting by a program that can calculate the deviation from the initial electron diffraction pattern, thereby minimizing dose consumption. The combination of sparse sampling and CS can recover all information with a significantly reduced dose consumption.

iii. The denoising of images by advanced algorithms can improve the SNR of acquired images, revealing more embedded information. Phase retrieval can aid in the reconstruction of phase images for interpretable images, in which ptychography can achieve the highest resolution at the same dose as other modes. In addition, simulation software has been developed to predict the image and determine the degree of similarity between experiment and simulation.

iv. The introduction of a cryogenic system to FIB for sample processing can effectively reduce the damage caused by the focused ion beam, and the sample protection by coating can reduce surface sputtering caused by the incident beam.

 This journal is © The Royal Society of Chemistry 2024

Open Access Article. Published on 21 March 2024. Downloaded on 1/15/2026 6:48:41 PM.
This article is licensed under a Creative Commons Attribution-NonCommercial 3.0 Unported Licence.

These developments facilitate the practical application of low-dose techniques, which helps disclose the exact structure of MOFs/COFs from metal clusters to organic linkage at the atomic level, elucidating the local structure, host–guest interaction, and surface and interface structure. These images provide solid evidence to explain the improvement in property from the perspective of microstructure difference, steering the modification and functionalization of materials based on the design of building blocks.

Despite the gratifying advances in low-dose technology, issues remain. A precisely determined defocus value is required for the analysis of HRTEM images, and a precisely focused beam results in a low success rate in iDPC-STEM. Machine learning may provide a solution for the analysis of collected images by identifying features automatically, even if they are indistinguishable to the naked eyes or conventional computer analysis; however, algorithm optimization is still required. In addition, ptychography in 4D-STEM, which can reconstruct the clearest images with the highest resolution near lattice vibrations, has tremendous potential for imaging beam-sensitive materials. While ptychography has been successfully applied to MOFs at a dose of 800 e $Å^{-2}$, the possibility of imaging at ultra-low dose (<100 e $Å^{-2}$) requires further investigation, despite the significant improvement in relevant computing capacity. Extremely beam-sensitive materials may necessitate the use of potent algorithms in conjunction with machine learning to accomplish imaging. If achieved, the monitoring of beam-sensitive materials at the atomic level in real time will no longer be an unattainable future objective.

Conflicts of interest

There are no conflicts to declare.

Acknowledgements

The authors acknowledge support from startup grant from the Department of Applied Physics, the Hong Kong Polytechnic University (1-BDCM), the General Research Fund (No. 15306021, 15306122), and the Early Career Scheme (No. 25305023) from the Hong Kong Research Grants Council (RGC), and the Warwick Startup Funding.

References

1 M. Varela, A. R. Lupini, K. V. Benthem, A. Y. Borisevich, M. F. Chisholm, N. Shibata, E. Abe and S. J. Pennycook, *Annu. Rev. Mater. Res.*, 2005, **35**, 539–569.
2 M. R. Lee, *Mineral. Mag.*, 2018, **74**, 1–27.
3 S. Abednatanzi, P. G. Derakhshandeh, H. Depauw, F. X. Coudert, H. Vrielinck, P. Van Der Voort and K. Leus, *Chem. Soc. Rev.*, 2019, **48**, 2535–2565.
4 O. M. Yaghi, G. Li and H. Li, *Nature*, 1995, **378**, 703–706.
5 A. P. Cote, A. I. Benin, N. W. Ockwig, M. O'Keeffe, A. J. Matzger and O. M. Yaghi, *Science*, 2005, **310**, 1166–1170.
6 Y. Cheng, S. J. Datta, S. Zhou, J. Jia, O. Shekhah and M. Eddaoudi, *Chem. Soc. Rev.*, 2022, **51**, 8300–8350.
7 S. Yuan, X. Li, J. Zhu, G. Zhang, P. Van Puyvelde and B. Van der Bruggen, *Chem. Soc. Rev.*, 2019, **48**, 2665–2681.
8 R. Liu, K. T. Tan, Y. Gong, Y. Chen, Z. Li, S. Xie, T. He, Z. Lu, H. Yang and D. Jiang, *Chem. Soc. Rev.*, 2021, **50**, 120–242.
9 G. Chakraborty, I. H. Park, R. Medishetty and J. J. Vittal, *Chem. Rev.*, 2021, **121**, 3751–3891.
10 X. Zhao, P. Pachfule and A. Thomas, *Chem. Soc. Rev.*, 2021, **50**, 6871–6913.
11 K. Winkler, *Chem. Rev.*, 2022, **122**, 10573–10574.
12 P. M. Bhatt, V. Guillerm, S. J. Datta, A. Shkurenko and M. Eddaoudi, *Chem*, 2020, **6**, 1613–1633.
13 K. Geng, T. He, R. Liu, S. Dalapati, K. T. Tan, Z. Li, S. Tao, Y. Gong, Q. Jiang and D. Jiang, *Chem. Rev.*, 2020, **120**, 8814–8933.
14 F. Haase and B. V. Lotsch, *Chem. Soc. Rev.*, 2020, **49**, 8469–8500.
15 D. B. Williams and C. B. Carter, *The transmission electron microscope*, Springer, 1996.
16 M. J. Cabral, Z. Chen and X. Liao, *Microstructures*, 2023, **3**, 2023040.
17 X. Wang, Y. Q. Wang, Y. C. Feng, D. Wang and L. J. Wan, *Chem. Soc. Rev.*, 2021, **50**, 5832–5849.
18 A. Sweetman, N. R. Champness and A. Saywell, *Chem. Soc. Rev.*, 2020, **49**, 4189–4202.
19 A. Bogner, P. H. Jouneau, G. Thollet, D. Basset and C. Gauthier, *Micron*, 2007, **38**, 390–401.
20 T. Sun, L. Wei, Y. Chen, Y. Ma and Y. B. Zhang, *J. Am. Chem. Soc.*, 2019, **141**, 10962–10966.
21 M. Ge, Y. Wang, F. Carraro, W. Liang, M. Roostaeinia, S. Siahrostami, D. M. Proserpio, C. Doonan, P. Falcaro, H. Zheng, X. Zou and Z. Huang, *Angew. Chem., Int. Ed.*, 2021, **60**, 11391–11397.
22 Z. H. Huang, E. S. Grape, J. Li, A. K. Inge and X. D. Zou, *Coord. Chem. Rev.*, 2021, **427**, 213583.
23 T. Yang, T. Willhammar, H. Xu, X. Zou and Z. Huang, *Nat. Protoc.*, 2022, **17**, 2389–2413.
24 X. C. Ren, X. Q. Zhang, R. Xu, J. Q. Huang and Q. Zhang, *Adv. Mater.*, 2020, **32**, e1908293.
25 Y. Zhu, J. Ciston, B. Zheng, X. Miao, C. Czarnik, Y. Pan, R. Sougrat, Z. Lai, C. E. Hsiung, K. Yao, I. Pinnau, M. Pan and Y. Han, *Nat. Mater.*, 2017, **16**, 532–536.
26 S. Ghosh, P. Kumar, S. Conrad, M. Tsapatsis and K. A. Mkhoyan, *Microsc. Microanal.*, 2019, **25**, 1704–1705.
27 Y. Zhou, X. H. Xu, A. Carlsson, S. Lazar, Z. C. Pan, Y. H. Ma, O. Terasaki and H. X. Deng, *Chem. Mater.*, 2020, **32**, 4966–4972.
28 B. D. A. Levin, *J. Phys.: Mater.*, 2021, **4**, 042005.
29 P. T. E. Roberts, J. N. Chapman and A. M. MacLeod, *Ultramicroscopy*, 1982, **8**, 385–396.
30 I. Lazic, E. G. T. Bosch and S. Lazar, *Ultramicroscopy*, 2016, **160**, 265–280.
31 C. Ophus, *Microsc. Microanal.*, 2019, **25**, 563–582.
32 Z. Chen, Y. Jiang, Y. T. Shao, M. E. Holtz, M. Odstrcil, M. Guizar-Sicairos, I. Hanke, S. Ganschow, D. G. Schlom and D. A. Muller, *Science*, 2021, **372**, 826–831.

Open Access Article. Published on 21 March 2024. Downloaded on 1/15/2026 6:48:41 PM. This article is licensed under a Creative Commons Attribution-NonCommercial 3.0 Unported Licence.

33 R. F. Egerton, *Microsc. Res. Technol.*, 2012, **75**, 1550–1556.
34 M. Hmadeh, Z. Lu, Z. Liu, F. Gándara, H. Furukawa, S. Wan, V. Augustyn, R. Chang, L. Liao, F. Zhou, E. Perre, V. Ozolins, K. Suenaga, X. Duan, B. Dunn, Y. Yamamto, O. Terasaki and O. M. Yaghi, *Chem. Mater.*, 2012, **24**, 3511–3513.
35 C. Wiktor, S. Turner, D. Zacher, R. A. Fischer and G. V. Tendeloo, *Microporous Mesoporous Mater.*, 2012, **162**, 131–135.
36 J. Zhang, J. Wen, W.-D. Liu, X. Cui and Y. Chen, *Sci. China: Mater.*, 2022, **65**, 2613–2626.
37 M. J. Zachman, Z. Tu, S. Choudhury, L. A. Archer and L. F. Kourkoutis, *Nature*, 2018, **560**, 345–349.
38 Y. Li, K. Wang, W. Zhou, Y. Li, R. Vila, W. Huang, H. Wang, G. Chen, G. H. Wu, Y. Tsao, H. Wang, R. Sinclair, W. Chiu and Y. Cui, *Matter*, 2019, **1**, 428–438.
39 A. F. Ogata, A. M. Rakowski, B. P. Carpenter, D. A. Fishman, J. G. Merham, P. J. Hurst and J. P. Patterson, *J. Am. Chem. Soc.*, 2020, **142**, 1433–1442.
40 L. Tong, S. Huang, Y. Shen, S. Liu, X. Ma, F. Zhu, G. Chen and G. Ouyang, *Nat. Commun.*, 2022, **13**, 951.
41 D. Zhang, Y. Zhu, L. Liu, X. Ying, C. E. Hsiung, R. Sougrat, K. Li and Y. Han, *Science*, 2018, **359**, 675–679.
42 S. Ghosh, H. Yun, P. Kumar, S. Conrad, M. Tsapatsis and K. A. Mkhoyan, *Chem. Mater.*, 2021, **33**, 5681–5689.
43 Y. Peng, Y. Huang, Y. Zhu, B. Chen, L. Wang, Z. Lai, Z. Zhang, M. Zhao, C. Tan, N. Yang, F. Shao, Y. Han and H. Zhang, *J. Am. Chem. Soc.*, 2017, **139**, 8698–8704.
44 L. Wang, M. Ma, H. Wang, H. Xiong, X. Chen, F. Wei and B. Shen, *ACS Nano*, 2023, **17**, 4740–4747.
45 J. C. H. Spence and J. M. Zuo, *Rev. Sci. Instrum.*, 1988, **59**, 2102–2105.
46 A. C. Milazzo, P. Leblanc, F. Duttweiler, L. Jin, J. C. Bouwer, S. Peltier, M. Ellisman, F. Bieser, H. S. Matis, H. Wieman, P. Denes, S. Kleinfelder and N. H. Xuong, *Ultramicroscopy*, 2005, **104**, 152–159.
47 A. Maigne and M. Wolf, *Microscopy*, 2018, **67**, i86–i97.
48 N. Shibata, Y. Kohno, S. D. Findlay, H. Sawada, Y. Kondo and Y. Ikuhara, *J. Electron Microsc.*, 2010, **59**, 473–479.
49 N. Shibata, S. D. Findlay, Y. Kohno, H. Sawada, Y. Kondo and Y. Ikuhara, *Nat. Phys.*, 2012, **8**, 611–615.
50 N. Shibata, *J. Ceram. Soc. Jpn.*, 2019, **127**, 708–714.
51 N. Shibata, T. Seki, G. Sanchez-Santolino, S. D. Findlay, Y. Kohno, T. Matsumoto, R. Ishikawa and Y. Ikuhara, *Nat. Commun.*, 2017, **8**, 15631.
52 E. G. T. Bosch, I. Lazic and S. Lazar, *Microsc. Microanal.*, 2016, **22**, 306–307.
53 B. Shen, H. Wang, H. Xiong, X. Chen, E. G. T. Bosch, I. Lazic, W. Qian and F. Wei, *Nature*, 2022, **607**, 703–707.
54 H. Xiong, Z. Liu, X. Chen, H. Wang, W. Qian, C. Zhang, A. Zheng and F. Wei, *Science*, 2022, **376**, 491–496.
55 T. A. Caswell, P. Ercius, M. W. Tate, A. Ercan, S. M. Gruner and D. A. Muller, *Ultramicroscopy*, 2009, **109**, 304–311.
56 M. W. Tate, P. Purohit, D. Chamberlain, K. X. Nguyen, R. Hovden, C. S. Chang, P. Deb, E. Turgut, J. T. Heron, D. G. Schlom, D. C. Ralph, G. D. Fuchs, K. S. Shanks, H. T. Philipp, D. A. Muller and S. M. Gruner, *Microsc. Microanal.*, 2016, **22**, 237–249.
57 Y. Han, S. Xie, K. Nguyen, M. Cao, M. W. Tate, P. Purohit, S. M. Gruner, J. Park and D. A. Muller, *Microsc. Microanal.*, 2017, **23**, 1712–1713.
58 Y. Jiang, Z. Chen, Y. Han, P. Deb, H. Gao, S. Xie, P. Purohit, M. W. Tate, J. Park, S. M. Gruner, V. Elser and D. A. Muller, *Nature*, 2018, **559**, 343–349.
59 H. Philipp, M. Tate, K. Shanks, L. Mele, M. Peemen, P. Dona, R. Hartong, G. van Veen, Y. T. Shao, S. Gruner, J. Thom-Levy and D. Muller, *Microsc. Microanal.*, 2021, **27**, 992–993.
60 H. T. Philipp, M. W. Tate, K. S. Shanks, L. Mele, M. Peemen, P. Dona, R. Hartong, G. van Veen, Y. T. Shao, Z. Chen, J. Thom-Levy, D. A. Muller and S. M. Gruner, *Microsc. Microanal.*, 2022, **28**, 425–440.
61 P. Ercius, I. Johnson, H. Brown, P. Pelz, S.-L. Hsu, B. Draney, E. Fong, A. Goldschmidt, J. Joseph, J. Lee, J. Ciston, C. Ophus, M. Scott, A. Selvarajan, D. Paul, D. Skinner, M. Hanwell, C. Harris, P. Avery, T. Stezelberger, C. Tindall, R. Ramesh, A. Minor and P. Denes, *Microsc. Microanal.*, 2020, **26**, 1896–1897.
62 B. Song, Z. Ding, C. S. Allen, H. Sawada, F. Zhang, X. Pan, J. Warner, A. I. Kirkland and P. Wang, *Phys. Rev. Lett.*, 2018, **121**, 146101.
63 C. S. Allen, J. Song, M. Danaie, P. Wang and A. I. Kirkland, *Microsc. Microanal.*, 2018, **24**, 186–187.
64 R. Sagawa, H. Hashiguchi, T. Isabell, R. Ritz, M. Simson, M. Huth, H. Soltau, G. T. Martinez, P. D. Nellist and Y. Kondo, *Microsc. Microanal.*, 2018, **24**, 198–199.
65 E. T. Utagawa, E. Nakazawa, K. Matsuo, I. Oishi, N. Takeda and T. Miyamura, *J. Virol. Methods*, 2002, **100**, 49–56.
66 J. Jansen, D. Tang, H. W. Zandbergen and H. Schenk, *Acta Crystallogr. A*, 1998, **54**, 91–101.
67 M. Hayashida, S. Terauchi and T. Fujimoto, *Micron*, 2010, **41**, 540–545.
68 J. Jansen, M. T. Otten and H. W. Zandbergen, *Ultramicroscopy*, 2013, **125**, 59–65.
69 N. Cautaerts, R. Delville and D. Schryvers, *J. Microsc.*, 2019, **273**, 189–198.
70 Y. Zhang, R. Yan, T. Sun and Y. Ma, *Ultramicroscopy*, 2020, **211**, 112941.
71 A. J. Koster, A. Van den Bos and K. D. van der Mast, *Ultramicroscopy*, 1987, **21**, 209–222.
72 K. Dierksen, D. Typke, R. Hegerl, A. J. Koster and W. Baumeister, *Ultramicroscopy*, 1992, **40**, 71–87.
73 A. Stevens, L. Luzi, H. Yang, L. Kovarik, B. L. Mehdi, A. Liyu, M. E. Gehm and N. D. Browning, *Appl. Phys. Lett.*, 2018, **112**, 043104.
74 S. Ganguli and H. Sompolinsky, *Annu. Rev. Neurosci.*, 2012, **35**, 485–508.
75 R. Leary, Z. Saghi, P. A. Midgley and D. J. Holland, *Ultramicroscopy*, 2013, **131**, 70–91.
76 Z. Saghi, D. J. Holland, R. Leary, A. Falqui, G. Bertoni, A. J. Sederman, L. F. Gladden and P. A. Midgley, *Nano Lett.*, 2011, **11**, 4666–4673.

 This journal is © The Royal Society of Chemistry 2024

Open Access Article. Published on 21 March 2024. Downloaded on 1/15/2026 6:48:41 PM. This article is licensed under a Creative Commons Attribution-NonCommercial 3.0 Unported Licence.

77 J. Schwartz, H. Zheng, M. Hanwell, Y. Jiang and R. Hovden, *Microsc. Microanal.*, 2020, **26**, 2462–2465.
78 L. Kovarik, A. Stevens, A. Liyu and N. D. Browning, *Appl. Phys. Lett.*, 2016, **109**, 164102.
79 A. Béché, B. Goris, B. Freitag and J. Verbeeck, *Appl. Phys. Lett.*, 2016, **108**, 093103.
80 A. Stevens, H. Yang, L. Carin, I. Arslan and N. D. Browning, *Microscopy*, 2014, **63**, 41–51.
81 A. Stevens, L. Kovarik, P. Abellan, X. Yuan, L. Carin and N. D. Browning, *Adv. Struct. Chem. Imaging*, 2015, **1**, 10.
82 B. L. Mehdi, A. Stevens, L. Kovarik, N. Jiang, H. Mehta, A. Liyu, S. Reehl, B. Stanfill, L. Luzi, W. Hao, L. Bramer and N. D. Browning, *Appl. Phys. Lett.*, 2019, **115**, 063102.
83 G. Möbus, G. Necker and M. Rühle, *Ultramicroscopy*, 1993, **49**, 46–65.
84 L. D. Marks, *Ultramicroscopy*, 1996, **62**, 43–52.
85 L. Jones and P. D. Nellist, *Microsc. Microanal.*, 2013, **19**, 1050–1060.
86 H. Du, *Ultramicroscopy*, 2015, **151**, 62–67.
87 C. Zhang, R. Han, A. R. Zhang and P. M. Voyles, *Ultramicroscopy*, 2020, **219**, 113123.
88 E. Heindl, W. D. Rau and H. Lichte, *Ultramicroscopy*, 1996, **64**, 87–97.
89 R. R. Meyer and E. Heindl, *J. Microsc.*, 1998, **191**, 52–59.
90 M. Guizar-Sicairos and J. R. Fienup, *Opt. Express*, 2008, **16**, 7264–7278.
91 A. M. Maiden and J. M. Rodenburg, *Ultramicroscopy*, 2009, **109**, 1256–1262.
92 W. Van den Broek and C. T. Koch, *Phys. Rev. Lett.*, 2012, **109**, 245502.
93 W. Van den Broek and C. T. Koch, *Phys. Rev. B: Condens. Matter Mater. Phys.*, 2013, **87**, 184108.
94 R. S. Pennington, W. Van den Broek and C. T. Koch, *Phys. Rev. B: Condens. Matter Mater. Phys.*, 2014, **89**, 205409.
95 P. D. Nellist and S. J. Pennycook, *Ultramicroscopy*, 1999, **78**, 111–124.
96 K. Mitsuishi, M. Takeguchi, Y. Toda and K. Furuya, *Ultramicroscopy*, 2003, **96**, 323–333.
97 L. J. Allen, A. J. D'Alfonso, M. Bosman, S. D. Findlay, M. P. Oxley, V. J. Keast, J. M. LeBeau and S. Stemmer, *Microsc. Microanal.*, 2008, **14**, 922–923.
98 T. Yamazaki, K. Watanabe, K. Kuramochi and I. Hashimoto, *Acta Crystallogr. A*, 2006, **62**, 233–236.
99 T. Morimura and M. Hasaka, *Ultramicroscopy*, 2009, **109**, 1203–1209.
100 T. Yamazaki, M. Ohtsuka, Y. Kotaka and K. Watanabe, *Ultramicroscopy*, 2013, **135**, 16–23.
101 R. S. Pennington, F. Wang and C. T. Koch, *Ultramicroscopy*, 2014, **141**, 32–37.
102 C. Ophus, *Adv. Struct. Chem. Imaging*, 2017, **3**, 13.
103 P. M. Pelz, A. Rakowski, L. Rangel DaCosta, B. H. Savitzky, M. C. Scott and C. Ophus, *Microsc. Microanal.*, 2021, **27**, 835–848.
104 R. S. Pennington, C. Coll, S. Estradé, F. Peiró and C. T. Koch, *Phys. Rev. B*, 2018, **97**, 024112.
105 C. Dwyer, *Ultramicroscopy*, 2010, **110**, 195–198.
106 I. Lobato and D. Van Dyck, *Ultramicroscopy*, 2015, **156**, 9–17.
107 W. Van den Broek, X. Jiang and C. T. Koch, *Ultramicroscopy*, 2015, **158**, 89–97.
108 Y. Yao, B. H. Ge, X. Shen, Y. G. Wang and R. C. Yu, *Ultramicroscopy*, 2016, **166**, 1–8.
109 C. T. Koch, *Determination of core structure periodicity and point defect density along dislocations*, PhD thesis, Arizona State University, 2002.
110 V. Grillo and E. Rotunno, *Ultramicroscopy*, 2013, **125**, 97–111.
111 S. Singh, F. Ram and M. De Graef, *Microsc. Microanal.*, 2017, **23**, 212–213.
112 L. Rangel DaCosta, H. G. Brown, P. M. Pelz, A. Rakowski, N. Barber, P. O'Donovan, P. McBean, L. Jones, J. Ciston, M. C. Scott and C. Ophus, *Micron*, 2021, **151**, 103141.
113 J. Barthel, *Ultramicroscopy*, 2018, **193**, 1–11.
114 P. J. Yuan, K. P. Wu, S. W. Chen, D. L. Zhang, C. H. Jin, Y. Yao and F. Lin, *J. Microsc.*, 2022, **287**, 93–104.
115 A. W. Robinson, D. Nicholls, J. Wells, A. Moshtaghpour, A. Kirkland and N. D. Browning, *Ultramicroscopy*, 2022, **242**, 113625.
116 A. W. Robinson, D. Nicholls, J. Wells, A. Moshtaghpour, A. I. Kirkland and N. D. Browning, *Microsc. Microanal.*, 2022, **28**, 3116–3117.
117 A. W. Robinson, J. Wells, D. Nicholls, A. Moshtaghpour, M. Chi, A. I. Kirkland and N. D. Browning, *J. Microsc.*, 2023, **290**, 53–66.
118 J. C. Bravman and R. Sinclair, *J. Electron Microsc. Technol.*, 1984, **1**, 53–61.
119 C. Quintana, *Micron*, 1997, **28**, 217–219.
120 H. Gnaegi, *Microsc. Microanal.*, 2020, **6**, 314–315.
121 Ł. Mielańczyk, N. Matysiak, O. Klymenko and R. Wojnicz, *Transmission electron microscopy of biological samples*, BoD–Books on Demand, 2015.
122 M. Corazza, S. B. Simonsen, H. Gnaegi, K. T. S. Thydén, F. C. Krebs and S. A. Gevorgyan, *Appl. Surf. Sci.*, 2016, **389**, 462–468.
123 H. Zhang, C. Wang and G. Zhou, *Microsc. Microanal.*, 2020, **26**, 867–877.
124 J. A. Kammerer, F. Feist, D. Ryklin, A. Sarkar, C. Barner-Kowollik and R. R. Schroder, *Adv. Mater.*, 2023, **35**, e2211074.
125 A. Kertik, L. H. Wee, M. Pfannmöller, S. Bals, J. A. Martens and I. F. J. Vankelecom, *Energy Environ. Sci.*, 2017, **10**, 2342–2351.
126 L. Swistak, A. Sartori-Rupp, M. Vos and J. Enninga, *Methods in Microbiology*, Elsevier, 2021.
127 M. H. F. Overwijk, F. C. Vandenheuvel and C. W. T. Bullelieuwma, *J. Vac. Sci. Technol. B*, 1993, **11**, 2021–2024.
128 F. A. Stevie, T. C. Shane, P. M. Kahora, R. Hull, D. Bahnck, V. C. Kannan and E. David, *Surf. Interface Anal.*, 1995, **23**, 61–68.
129 L. A. Giannuzzi, J. L. Drown, S. R. Brown, R. B. Irwin and F. A. Stevie, *Microsc. Res. Technol.*, 1998, **41**, 285–290.

Open Access Article. Published on 21 March 2024. Downloaded on 1/15/2026 6:48:41 PM. This article is licensed under a Creative Commons Attribution-NonCommercial 3.0 Unported Licence.

130 M. Marko, C. Hsieh, R. Schalek, J. Frank and C. Mannella, *Nat. Methods*, 2007, **4**, 215–217.
131 M. Marko, C. Hsieh, D. Vetter, N. J. Salmon and C. Mannella, *Microsc. Microanal.*, 2010, **16**, 178–179.
132 K. Narayan and S. Subramaniam, *Nat. Methods*, 2015, **12**, 1021–1031.
133 K. M. Strunk, K. Wang, D. Ke, J. L. Gray and P. Zhang, *J. Microsc.*, 2012, **247**, 220–227.
134 J. He, C. Hsieh, Y. Wu, T. Schmelzer, P. Wang, Y. Lin, M. Marko and H. Sui, *J. Struct. Biol.*, 2017, **199**, 114–119.
135 M. J. Zachman, J. M. Noble and L. F. Kourkoutis, *Microsc. Microanal.*, 2017, **23**, 2312–2313.
136 S. Kim, M. Jeong Park, N. P. Balsara, G. Liu and A. M. Minor, *Ultramicroscopy*, 2011, **111**, 191–199.
137 Y. Li, Y. Li, A. Pei, K. Yan, Y. Sun, C. L. Wu, L. M. Joubert, R. Chin, A. L. Koh, Y. Yu, J. Perrino, B. Butz, S. Chu and Y. Cui, *Science*, 2017, **358**, 506–510.
138 J. Alvarado, M. A. Schroeder, T. P. Pollard, X. F. Wang, J. Z. Lee, M. H. Zhang, T. Wynn, M. Ding, O. Borodin, Y. S. Meng and K. Xu, *Energy Environ. Sci.*, 2019, **12**, 780–794.
139 J. Z. Lee, T. A. Wynn, M. A. Schroeder, J. Alvarado, X. F. Wang, K. Xu and Y. S. Meng, *ACS Energy Lett.*, 2019, **4**, 489–493.
140 Y. H. Chang, W. J. Lu, J. Guenole, L. T. Stephenson, A. Szczpaniak, P. Kontis, A. K. Ackerman, F. F. Dear, I. Mouton, X. K. Zhong, S. Y. Zhang, D. Dye, C. H. Liebscher, D. Ponge, S. Korte-Kerzel, D. Raabe and B. Gault, *Nat. Commun.*, 2019, **10**, 942.
141 M. J. Zachman, Z. Tu, L. A. Archer and L. F. Kourkoutis, *ACS Energy Lett.*, 2020, **5**, 1224–1232.
142 K. Sardashti, R. Haight, R. Anderson, M. Contreras, B. Fruhberger and A. C. Kummel, *ACS Appl. Mater. Interfaces*, 2016, **8**, 14994–14999.
143 D. M. Long, M. K. Singh, K. A. Small and J. Watt, *Nanotechnology*, 2022, **33**, 503001.
144 C. D. Parmenter and Z. A. Nizamudeen, *J. Microsc.*, 2021, **281**, 157–174.
145 J. Zhou, N. Wei, D. Zhang, Y. Wang, J. Li, X. Zheng, J. Wang, A. Y. Alsalloum, L. Liu, O. M. Bakr and Y. Han, *J. Am. Chem. Soc.*, 2022, **144**, 3182–3191.
146 J. Li, P. Liu, Y. Chen, J. Zhou, J. Li, J. Yang, D. Zhang, J. Li and L. Li, *J. Am. Chem. Soc.*, 2023, **145**, 19707–19714.
147 S. M. Salih and V. E. Cosslett, *Philos. Mag.*, 1974, **30**, 225–228.
148 N. Mohanty, M. Fahrenholtz, A. Nagaraja, D. Boyle and V. Berry, *Nano Lett.*, 2011, **11**, 1270–1275.
149 M. Kalbac, O. Lehtinen, A. V. Krasheninnikov and J. Keinonen, *Adv. Mater.*, 2013, **25**, 1004–1009.
150 G. Algara-Siller, S. Kurasch, M. Sedighi, O. Lehtinen and U. Kaiser, *Appl. Phys. Lett.*, 2013, **103**, 203107.
151 R. Zan, Q. M. Ramasse, R. Jalil, T. Georgiou, U. Bangert and K. S. Novoselov, *ACS Nano*, 2013, **7**, 10167–10174.
152 K. Elibol, T. Susi, G. Argentero, M. Reza Ahmadpour Monazam, T. J. Pennycook, J. C. Meyer and J. Kotakoski, *Chem. Mater.*, 2018, **30**, 1230–1238.
153 Y. Lee, J. Y. Yoon, H. Y. Jeong and K. Kim, *Microsc. Microanal.*, 2019, **25**, 1696–1697.
154 B. Yuan, Z. Hua, S. Jia, Y. Lu, E. Shi and Y. Yu, *Microsc. Res. Technol.*, 2022, **85**, 3582–3588.
155 S. T. Skowron, S. L. Roberts, A. N. Khlobystov and E. Besley, *Micron*, 2019, **120**, 96–103.
156 O. I. Lebedev, F. Millange, C. Serre, G. Van Tendeloo and G. Férey, *Chem. Mater.*, 2005, **17**, 6525–6527.
157 B. Xiao, P. J. Byrne, P. S. Wheatley, D. S. Wragg, X. Zhao, A. J. Fletcher, K. M. Thomas, L. Peters, J. S. Evans, J. E. Warren, W. Zhou and R. E. Morris, *Nat. Chem.*, 2009, **1**, 289–294.
158 H. Deng, S. Grunder, K. E. Cordova, C. Valente, H. Furukawa, M. Hmadeh, F. Gandara, A. C. Whalley, Z. Liu, S. Asahina, H. Kazumori, M. O'Keeffe, O. Terasaki, J. F. Stoddart and O. M. Yaghi, *Science*, 2012, **336**, 1018–1023.
159 D. Feng, T. Lei, M. R. Lukatskaya, J. Park, Z. Huang, M. Lee, L. Shaw, S. Chen, A. A. Yakovenko, A. Kulkarni, J. Xiao, K. Fredrickson, J. B. Tok, X. Zou, Y. Cui and Z. Bao, *Nat. Energy*, 2018, **3**, 30–36.
160 L. Liu, Z. Chen, J. Wang, D. Zhang, Y. Zhu, S. Ling, K. W. Huang, Y. Belmabkhout, K. Adil, Y. Zhang, B. Slater, M. Eddaoudi and Y. Han, *Nat. Chem.*, 2019, **11**, 622–628.
161 C. Chen, M. R. Alalouni, X. Dong, Z. Cao, Q. Cheng, L. Zheng, L. Meng, C. Guan, L. Liu, E. Abou-Hamad, J. Wang, Z. Shi, K. W. Huang, L. Cavallo and Y. Han, *J. Am. Chem. Soc.*, 2021, **143**, 7144–7153.
162 L. Robison, X. Gong, A. M. Evans, F. A. Son, X. Wang, L. R. Redfern, M. C. Wasson, Z. H. Syed, Z. Chen, K. B. Idrees, T. Islamoglu, M. Delferro, W. R. Dichtel, F. X. Coudert, N. C. Gianneschi and O. K. Farha, *J. Am. Chem. Soc.*, 2021, **143**, 1503–1512.
163 Y. M. Gu, Y. Y. Yuan, C. L. Chen, S. S. Zhao, T. J. Sun, Y. Han, X. W. Liu, Z. Lai and S. D. Wang, *Chem. Sci.*, 2023, **14**, 1472–1478.
164 Y. Xu, L. Jiao, J. Ma, P. Zhang, Y. Tang, L. Liu, Y. Liu, H. Ding, J. Sun, M. Wang, Z. Li, H.-L. Jiang and W. Chen, *Joule*, 2023, **7**, 515–528.
165 M. Qi, Y. Zhou, Y. Lv, W. Chen, X. Su, T. Zhang, G. Xing, G. Xu, O. Terasaki and L. Chen, *J. Am. Chem. Soc.*, 2023, **145**, 2739–2744.
166 L. Sun, L. Yang, J. H. Dou, J. Li, G. Skorupskii, M. Mardini, K. O. Tan, T. Chen, C. Sun, J. J. Oppenheim, R. G. Griffin, M. Dinca and T. Rajh, *J. Am. Chem. Soc.*, 2022, **144**, 19008–19016.
167 J. Y. Choi, M. Stodolka, N. Kim, H. T. B. Pham, B. Check and J. Park, *Chem*, 2023, **9**, 143–153.
168 Y. Liu, X. Li, S. Zhang, Z. Wang, Q. Wang, Y. He, W. H. Huang, Q. Sun, X. Zhong, J. Hu, X. Guo, Q. Lin, Z. Li, Y. Zhu, C. C. Chueh, C. L. Chen, Z. Xu and Z. Zhu, *Adv. Mater.*, 2023, 2300945.
169 X. Gong, H. Noh, N. C. Gianneschi and O. K. Farha, *J. Am. Chem. Soc.*, 2019, **141**, 6146–6151.
170 M. O. Cichocka, Z. Liang, D. Feng, S. Back, S. Siahrostami, X. Wang, L. Samperisi, Y. Sun, H. Xu, N. Hedin, H. Zheng,

 This journal is © The Royal Society of Chemistry 2024

Open Access Article. Published on 21 March 2024. Downloaded on 1/15/2026 6:48:41 PM. This article is licensed under a Creative Commons Attribution-NonCommercial 3.0 Unported Licence.

X. Zou, H. C. Zhou and Z. Huang, *J. Am. Chem. Soc.*, 2020, **142**, 15386–15395.

171 K. C. Bentz, K. Gnanasekaran, J. B. Bailey, S. Ayala, Jr., F. A. Tezcan, N. C. Gianneschi and S. M. Cohen, *Chem. Sci.*, 2020, **11**, 10523–10528.

172 A. M. Evans, L. R. Parent, N. C. Flanders, R. P. Bisbey, E. Vitaku, M. S. Kirschner, R. D. Schaller, L. X. Chen, N. C. Gianneschi and W. R. Dichtel, *Science*, 2018, **361**, 52–57.

173 A. M. Evans, I. Castano, A. Brumberg, L. R. Parent, A. R. Corcos, R. L. Li, N. C. Flanders, D. J. Gosztola, N. C. Gianneschi, R. D. Schaller and W. R. Dichtel, *J. Am. Chem. Soc.*, 2019, **141**, 19728–19735.

174 L. Yao, A. Rodriguez-Camargo, M. Xia, D. Mucke, R. Guntermann, Y. Liu, L. Grunenberg, A. Jimenez-Solano, S. T. Emmerling, V. Duppel, K. Sivula, T. Bein, H. Qi, U. Kaiser, M. Gratzel and B. V. Lotsch, *J. Am. Chem. Soc.*, 2022, **144**, 10291–10300.

175 A. Natraj, W. Ji, J. Xin, I. Castano, D. W. Burke, A. M. Evans, M. J. Strauss, M. Ateia, L. S. Hamachi, N. C. Gianneschi, A. L. Za, J. Sun, K. Yusuf and W. R. Dichtel, *J. Am. Chem. Soc.*, 2022, **144**, 19813–19824.

176 K. Yusuf, A. Natraj, K. Li, M. Ateia, Z. A. Alothman and W. R. Dichtel, *Chem. Mater.*, 2023, **35**, 1691–1701.

177 L. D. Tran, K. F. Presley, J. K. Streit, J. Carpena-Núñez, L. K. Beagle, T. A. Grusenmeyer, M. J. Dalton, R. A. Vaia, L. F. Drummy, N. R. Glavin and L. A. Baldwin, *Chem. Mater.*, 2022, **34**, 529–536.

178 J. Sprachmann, T. Wachsmuth, M. Bhosale, D. Burmeister, G. J. Smales, M. Schmidt, Z. Kochovski, N. Grabicki, R. Wessling, E. J. W. List-Kratochvil, B. Esser and O. Dumele, *J. Am. Chem. Soc.*, 2023, **145**, 2840–2851.

179 X. Li, C. Zhang, S. Cai, X. Lei, V. Altoe, F. Hong, J. J. Urban, J. Ciston, E. M. Chan and Y. Liu, *Nat. Commun.*, 2018, **9**, 2998.

180 X. R. Ren, B. Bai, Q. Zhang, Q. Hao, Y. Guo, L. J. Wan and D. Wang, *J. Am. Chem. Soc.*, 2022, **144**, 2488–2494.

181 P. Das, G. Chakraborty, J. Roeser, S. Vogl, J. Rabeah and A. Thomas, *J. Am. Chem. Soc.*, 2023, **145**, 2975–2984.

182 Y. Peng, L. Li, C. Zhu, B. Chen, M. Zhao, Z. Zhang, Z. Lai, X. Zhang, C. Tan, Y. Han, Y. Zhu and H. Zhang, *J. Am. Chem. Soc.*, 2020, **142**, 13162–13169.

183 L. Li, Q. Yun, C. Zhu, G. Sheng, J. Guo, B. Chen, M. Zhao, Z. Zhang, Z. Lai, X. Zhang, Y. Peng, Y. Zhu and H. Zhang, *J. Am. Chem. Soc.*, 2022, **144**, 6475–6482.

184 T. Ma, Y. Zhou, C. S. Diercks, J. Kwon, F. Gándara, H. Lyu, N. Hanikel, P. Pena-Sánchez, Y. Liu, N. J. Diercks, R. O. Ritchie, D. M. Proserpio, O. Terasaki and O. M. Yaghi, *Nat. Synth.*, 2023, **2**, 286–295.

185 J. Ding, X. Guan, J. Lv, X. Chen, Y. Zhang, H. Li, D. Zhang, S. Qiu, H. L. Jiang and Q. Fang, *J. Am. Chem. Soc.*, 2023, **145**, 3248–3254.

186 Y. Liu, L. Liu, X. Chen, Y. Liu, Y. Han and Y. Cui, *J. Am. Chem. Soc.*, 2021, **143**, 3509–3518.

187 J. Wang, P. Yang, L. Liu, B. Zheng, J. Jiang, J.-P. Ma, Y. Yan, S. Yang, L. Yang, Q.-K. Liu, Y. Han and Y. Chen, *CCS Chem.*, 2022, **4**, 1879–1888.

188 H. Wu, M. Almalki, X. Xu, Y. Lei, F. Ming, A. Mallick, V. Roddatis, S. Lopatin, O. Shekhah, M. Eddaoudi and H. N. Alshareef, *J. Am. Chem. Soc.*, 2019, **141**, 20037–20042.

189 J. H. Dou, M. Q. Arguilla, Y. Luo, J. Li, W. Zhang, L. Sun, J. L. Mancuso, L. Yang, T. Chen, L. R. Parent, G. Skorupskii, N. J. Libretto, C. Sun, M. C. Yang, P. V. Dip, E. J. Brignole, J. T. Miller, J. Kong, C. H. Hendon, J. Sun and M. Dinca, *Nat. Mater.*, 2021, **20**, 222–228.

190 Z. Wang, L. S. Walter, M. Wang, P. S. Petkov, B. Liang, H. Qi, N. N. Nguyen, M. Hambsch, H. Zhong, M. Wang, S. Park, L. Renn, K. Watanabe, T. Taniguchi, S. C. B. Mannsfeld, T. Heine, U. Kaiser, S. Zhou, R. T. Weitz, X. Feng and R. Dong, *J. Am. Chem. Soc.*, 2021, **143**, 13624–13632.

191 Q. Liu, Y. Miao, L. F. Villalobos, S. Li, H. Y. Chi, C. Chen, M. T. Vahdat, S. Song, D. J. Babu, J. Hao, Y. Han, M. Tsapatsis and K. V. Agrawal, *Nat. Mater.*, 2023, **22**, 1387–1393.

192 X. Li, K. Zhang, G. Wang, Y. Yuan, G. Zhan, T. Ghosh, W. P. D. Wong, F. Chen, H.-S. Xu, U. Mirsaidov, K. Xie, J. Lin and K. P. Loh, *Nat. Synth.*, 2022, **1**, 382–392.

193 X. Li, H. S. Xu, K. Leng, S. W. Chee, X. Zhao, N. Jain, H. Xu, J. Qiao, Q. Gao, I. H. Park, S. Y. Quek, U. Mirsaidov and K. P. Loh, *Nat. Chem.*, 2020, **12**, 1115–1122.

194 K. Liu, H. Qi, R. Dong, R. Shivhare, M. Addicoat, T. Zhang, H. Sahabudeen, T. Heine, S. Mannsfeld, U. Kaiser, Z. Zheng and X. Feng, *Nat. Chem.*, 2019, **11**, 994–1000.

195 Z. Wang, Z. Zhang, H. Qi, A. Ortega-Guerrero, L. Wang, K. Xu, M. Wang, S. Park, F. Hennersdorf, A. Dianat, A. Croy, H. Komber, G. Cuniberti, J. J. Weigand, U. Kaiser, R. Dong and X. Feng, *Nat. Synth.*, 2021, **1**, 69–76.

196 H. Qi, H. Sahabudeen, B. Liang, M. Polozij, M. A. Addicoat, T. E. Gorelik, M. Hambsch, M. Mundszinger, S. Park, B. V. Lotsch, S. C. B. Mannsfeld, Z. Zheng, R. Dong, T. Heine, X. Feng and U. Kaiser, *Sci. Adv.*, 2020, **6**, eabb5976.

197 B. Liang, Y. Zhang, C. Leist, Z. Ou, M. Polozij, Z. Wang, D. Mucke, R. Dong, Z. Zheng, T. Heine, X. Feng, U. Kaiser and H. Qi, *Nat. Commun.*, 2022, **13**, 3948.

198 X. Li, J. Wang, X. Liu, L. Liu, D. Cha, X. Zheng, A. A. Yousef, K. Song, Y. Zhu, D. Zhang and Y. Han, *J. Am. Chem. Soc.*, 2019, **141**, 12021–12028.

199 X. Han, P. Liu, F. Lin, W. Chen, R. Luo, Q. Han, Z. Jiang, X. Wang, S. Song, K. M. Reddy, H. Deng and M. Chen, *Angew. Chem., Int. Ed.*, 2020, **59**, 21419–21424.

200 L. Cao, X. Liu, D. B. Shinde, C. Chen, I. C. Chen, Z. Li, Z. Zhou, Z. Yang, Y. Han and Z. Lai, *Angew. Chem., Int. Ed.*, 2022, **61**, e202113141.

201 C. Feriante, A. M. Evans, S. Jhulki, I. Castano, M. J. Strauss, S. Barlow, W. R. Dichtel and S. R. Marder, *J. Am. Chem. Soc.*, 2020, **142**, 18637–18644.

202 D. Aulakh, L. Liu, J. R. Varghese, H. Xie, T. Islamoglu, K. Duell, C. W. Kung, C. E. Hsiung, Y. Zhang, R. J. Drout, O. K. Farha, K. R. Dunbar, Y. Han and M. Wriedt, *J. Am. Chem. Soc.*, 2019, **141**, 2997–3005.

203 S. Ehrling, E. M. Reynolds, V. Bon, I. Senkovska, T. E. Gorelik, J. D. Evans, M. Rauche, M. Mendt,

Open Access Article. Published on 21 March 2024. Downloaded on 1/15/2026 6:48:41 PM. This article is licensed under a Creative Commons Attribution-NonCommercial 3.0 Unported Licence.

M. S. Weiss, A. Poppl, E. Brunner, U. Kaiser, A. L. Goodwin and S. Kaskel, *Nat. Chem.*, 2021, **13**, 568–574.
204 X. Han, W. Chen, R. Su, Y. Tian, P. Liu, P. Guan, M. Luo, J. Han, X. Cao, M. Pan and M. Chen, *Nanoscale*, 2021, **13**, 13215–13219.
205 C. Guan, H. Wu, W. Ren, C. Yang, X. Liu, X. Ouyang, Z. Song, Y. Zhang, S. J. Pennycook, C. Cheng and J. Wang, *J. Mater. Chem. A*, 2018, **6**, 9009–9018.
206 A. Mayoral, M. Sanchez-Sanchez, A. Alfayate, J. Perez-Pariente and I. Diaz, *ChemCatChem*, 2015, **7**, 3719–3724.
207 Z. Thiam, E. Abou-Hamad, B. Dereli, L. Liu, A. H. Emwas, R. Ahmad, H. Jiang, A. A. Isah, P. B. Ndiaye, M. Taoufik, Y. Han, L. Cavallo, J. M. Basset and M. Eddaoudi, *J. Am. Chem. Soc.*, 2020, **142**, 16690–16703.
208 X. Peng, P. M. Pelz, Q. Zhang, P. Chen, L. Cao, Y. Zhang, H. G. Liao, H. Zheng, C. Wang, S. G. Sun and M. C. Scott, *Nat. Commun.*, 2022, **13**, 5197.
209 M. Meledina, S. Turner, M. Filippousi, K. Leus, I. Lobato, R. K. Ramachandran, J. Dendooven, C. Detavernier, P. Van Der Voort and G. Van Tendeloo, *Part. Part. Syst. Char.*, 2016, **33**, 382–387.
210 S. J. Datta, A. Mayoral, N. Murthy Srivatsa Bettahalli, P. M. Bhatt, M. Karunakaran, I. D. Carja, D. Fan, M. M. P. Graziane, R. Semino, G. Maurin, O. Terasaki and M. Eddaoudi, *Science*, 2022, **376**, 1080–1087.
211 S. Cai, Y. Lun, D. Ji, P. Lv, L. Han, C. Guo, Y. Zang, S. Gao, Y. Wei, M. Gu, C. Zhang, Z. Gu, X. Wang, C. Addiego, D. Fang, Y. Nie, J. Hong, P. Wang and X. Pan, *Nat. Commun.*, 2022, **13**, 5116.
212 B. Shen, X. Chen, K. Shen, H. Xiong and F. Wei, *Nat. Commun.*, 2020, **11**, 2692.
213 X. Feng, H. S. Jena, C. Krishnaraj, D. Arenas-Esteban, K. Leus, G. Wang, J. Sun, M. Ruscher, J. Timoshenko, B. Roldan Cuenya, S. Bals and P. V. Voort, *J. Am. Chem. Soc.*, 2021, **143**, 21511–21518.
214 D. Sun, L. W. Wong, H. Y. Wong, K. H. Lai, L. Ye, X. Xv, T. H. Ly, Q. Deng and J. Zhao, *Angew. Chem., Int. Ed.*, 2023, **62**, e202216008.
215 B. Liu, X. Chen, N. Huang, S. Liu, Y. Wang, X. Lan, F. Wei and T. Wang, *Nat. Commun.*, 2023, **14**, 4835.
216 L. Zhang, Y. Zhou, M. Jia, Y. W. He, W. Hu, Q. Liu, J. Li, X. H. Xu, C. Wang, A. Carlsson, S. Lazar, A. Meingast, Y. H. Ma, J. Xu, W. Wen, Z. H. Liu, J. Cheng and H. X. Deng, *Matter*, 2020, **2**, 1049–1063.
217 Y. Liu, J. Li, J. Lv, Z. Wang, J. Suo, J. Ren, J. Liu, D. Liu, Y. Wang, V. Valtchev, S. Qiu, D. Zhang and Q. Fang, *J. Am. Chem. Soc.*, 2023, **145**, 9679–9685.
218 Z. Jiang, X. Xu, Y. Ma, H. S. Cho, D. Ding, C. Wang, J. Wu, P. Oleynikov, M. Jia, J. Cheng, Y. Zhou, O. Terasaki, T. Peng, L. Zan and H. Deng, *Nature*, 2020, **586**, 549–554.
219 B. Liu, X. Chen, N. Huang, S. Liu, B. Shen, F. Wei and T. Wang, *Nano Lett.*, 2023, **23**, 1787–1793.
220 M. Ma, L. Wang, H. Wang, H. Xiong, X. Chen, F. Wei and B. Shen, *Nano Lett.*, 2022, **22**, 9928–9934.
221 M. Botifoll, I. Pinto-Huguet and J. Arbiol, *Nanoscale Horiz.*, 2022, **7**, 1427–1477.
222 J. Song, C. S. Allen, S. Gao, C. Huang, H. Sawada, X. Pan, J. Warner, P. Wang and A. I. Kirkland, *Sci. Rep.*, 2019, **9**, 3919.
223 S. Cao, P. Kok, P. Li, A. M. Maiden and J. M. Rodenburg, *Phys. Rev. A*, 2016, **94**, 063621.
224 Z. Chen, M. Odstrcil, Y. Jiang, Y. Han, M. H. Chiu, L. J. Li and D. A. Muller, *Nat. Commun.*, 2020, **11**, 2994.
225 L. Zhou, J. Song, J. S. Kim, X. Pei, C. Huang, M. Boyce, L. Mendonca, D. Clare, A. Siebert, C. S. Allen, E. Liberti, D. Stuart, X. Pan, P. D. Nellist, P. Zhang, A. I. Kirkland and P. Wang, *Nat. Commun.*, 2020, **11**, 2773.
226 Z. Ding, S. Gao, W. Fang, C. Huang, L. Zhou, X. Pei, X. Liu, X. Pan, C. Fan, A. I. Kirkland and P. Wang, *Nat. Commun.*, 2022, **13**, 4787.
227 X. Pei, L. Zhou, C. Huang, M. Boyce, J. S. Kim, E. Liberti, Y. Hu, T. Sasaki, P. D. Nellist, P. Zhang, D. I. Stuart, A. I. Kirkland and P. Wang, *Nat. Commun.*, 2023, **14**, 3027.
228 C. M. O'Leary, C. S. Allen, C. Huang, J. S. Kim, E. Liberti, P. D. Nellist and A. I. Kirkland, *Appl. Phys. Lett.*, 2020, **116**, 124101.
229 Z. Dong, E. Zhang, Y. Jiang, Q. Zhang, A. Mayoral, H. Jiang and Y. Ma, *J. Am. Chem. Soc.*, 2023, **145**, 6628–6632.
230 H. Sha, J. Cui, J. Li, Y. Zhang, W. Yang, Y. Li and R. Yu, *Sci. Adv.*, 2023, **9**, eadf1151.
231 H. Zhang, G. Li, J. Zhang, D. Zhang, Z. Chen, X. Liu, P. Guo, Y. Zhu, C. Chen, L. Liu, X. Guo and Y. Han, *Science*, 2023, **380**, 633–638.
232 H. Sha, J. Cui and R. Yu, *Sci. Adv.*, 2022, **8**, eabn2275.
233 J. Lv, H. Zhang, D. Zhang, L. Liu and Y. Han, *Acc. Mater. Res.*, 2022, **3**, 552–564.
234 H. G. Liao, D. Zherebetskyy, H. Xin, C. Czarnik, P. Ercius, H. Elmlund, M. Pan, L. W. Wang and H. Zheng, *Science*, 2014, **345**, 916–919.
235 W. Yuan, B. Zhu, X. Y. Li, T. W. Hansen, Y. Ou, K. Fang, H. Yang, Z. Zhang, J. B. Wagner, Y. Gao and Y. Wang, *Science*, 2020, **367**, 428–430.
236 X. Sun, D. Wu, L. Zou, S. D. House, X. Chen, M. Li, D. N. Zakharov, J. C. Yang and G. Zhou, *Nature*, 2022, **607**, 708–713.
237 J. P. Patterson, P. Abellan, M. S. Denny, Jr., C. Park, N. D. Browning, S. M. Cohen, J. E. Evans and N. C. Gianneschi, *J. Am. Chem. Soc.*, 2015, **137**, 7322–7328.
238 K. M. Vailonis, K. Gnanasekaran, X. B. Powers, N. C. Gianneschi and D. M. Jenkins, *J. Am. Chem. Soc.*, 2019, **141**, 10177–10182.
239 B. J. Smith, L. R. Parent, A. C. Overholts, P. A. Beaucage, R. P. Bisbey, A. D. Chavez, N. Hwang, C. Park, A. M. Evans, N. C. Gianneschi and W. R. Dichtel, *ACS Cent. Sci.*, 2017, **3**, 58–65.
240 L. R. Parent, C. H. Pham, J. P. Patterson, M. S. Denny, Jr., S. M. Cohen, N. C. Gianneschi and F. Paesani, *J. Am. Chem. Soc.*, 2017, **139**, 13973–13976.
241 J. Lyu, X. Gong, S. J. Lee, K. Gnanasekaran, X. Zhang, M. C. Wasson, X. Wang, P. Bai, X. Guo, N. C. Gianneschi and O. K. Farha, *J. Am. Chem. Soc.*, 2020, **142**, 4609–4615.
242 J. P. Buban and S.-Y. Choi, *Microsc. Microanal.*, 2017, **23**, 130–131.

 This journal is © The Royal Society of Chemistry 2024

Open Access Article. Published on 21 March 2024. Downloaded on 1/15/2026 6:48:41 PM.
This article is licensed under a Creative Commons Attribution-NonCommercial 3.0 Unported Licence.

243 J. M. Ede and R. Beanland, *Ultramicroscopy*, 2019, **202**, 18–25.
244 J. L. Vincent, R. Manzorro, S. Mohan, B. Tang, D. Y. Sheth, E. P. Simoncelli, D. S. Matteson, C. Fernandez-Granda and P. A. Crozier, *Microsc. Microanal.*, 2021, **27**, 1431–1447.
245 S. Mohan, R. Manzorro, J. L. Vincent, B. Tang, D. Y. Sheth, E. P. Simoncelli, D. S. Matteson, P. A. Crozier and C. Fernandez-Granda, *IEEE Trans. Comput. Imaging*, 2022, **8**, 585–597.
246 J. Han, K. J. Go, J. Jang, S. Yang and S. Y. Choi, *npj Comput. Mater.*, 2022, **8**, 196.
247 G. Correa and D. Muller, *Microsc. Microanal.*, 2020, **26**, 1932–1934.
248 P. Cueva, E. Padget and D. A. Muller, *Microsc. Microanal.*, 2018, **24**, 490–491.
249 M. P. Oxley, M. Ziatdinov, O. Dyck, A. R. Lupini, R. Vasudevan and S. V. Kalinin, *npj Comput. Mater.*, 2021, **7**, 65.
250 X. Li, O. E. Dyck, M. P. Oxley, A. R. Lupini, L. McInnes, J. Healy, S. Jesse and S. V. Kalinin, *npj Comput. Mater.*, 2019, **5**, 5.
251 T. Friedrich, C. P. Yu, J. Verbeek, T. Pennycook and S. V. Aert, the 2021 IEEE International Conference on Image Processing (ICIP), 2021.
252 M. Ziatdinov, O. Dyck, A. Maksov, X. Li, X. Sang, K. Xiao, R. R. Unocic, R. Vasudevan, S. Jesse and S. V. Kalinin, *ACS Nano*, 2017, **11**, 12742–12752.
253 K. Lee, J. Park, S. Choi, Y. Lee, S. Lee, J. Jung, J. Y. Lee, F. Ullah, Z. Tahir, Y. S. Kim, G. H. Lee and K. Kim, *Nano Lett.*, 2022, **22**, 4677–4685.
254 L. Yao, Z. Ou, B. Luo, C. Xu and Q. Chen, *ACS Cent. Sci.*, 2020, **6**, 1421–1430.
255 X. L. Lu and K. He, *Microsc. Microanal.*, 2023, **29**, 1895–1896.
256 C. Wang, Q. Zou, Z. Cheng, J. Chen, C. Luo, F. Liang, C. Cai, H. Bi, X. Lian, X. Ji, Q. Zhang, L. Sun and X. Wu, *Nanotechnology*, 2021, **33**, 085302.